Extraction and transport of ion beams from an ECR ion source

Saminathan, Suresh

Document Version
Publisher's PDF, also known as Version of record

Publication date:
2011

Citation for published version (APA):
Saminathan, S. (2011). Extraction and transport of ion beams from an ECR ion source University of Groningen: s.n.

Extraction and Transport of Ion Beams from an ECR Ion Source

To My Parents

COVER: *Calculated spatial distributions for a fully space-charge compensated Ne*$^{6+}$ *beam behind the* 90° *bending magnet at location VT3.*

The present work has been performed with financial support from the University of Groningen and the GSI Helmholtzzentrum, Darmstadt.

It is part of the research programme of the 'Stichting voor Fundamenteel Onderzoek der Materie (FOM)', which is financially supported by the 'Nederlandse Organisatie voor Wetenschappelijk Onderzoek (NWO)', and was also supported by the European Commission within the Seventh Framework Programme through IA-ENSAR (contract no. RII3-CT-2010-262010).

PRINTED BY: Facilitair Bedrijf, University of Groningen, Groningen, October-2011

RIJKSUNIVERSITEIT GRONINGEN

Extraction and Transport of Ion Beams from an ECR Ion Source

Proefschrift

ter verkrijging van het doctoraat in de
Wiskunde en Natuurwetenschappen
aan de Rijksuniversiteit Groningen
op gezag van de
Rector Magnificus, dr. E. Sterken,
in het openbaar te verdedigen op
vrijdag 11 november 2011
om 12:45 uur

door

Suresh Saminathan

geboren op 4 mei 1979
te Vellore, Tamilnadu, India

Promotor:	Prof. dr. S. Brandenberg
Copromotor:	Dr. ir. J. P. M. Beijers
Beoordelingscommissie:	Prof. dr. K. J. Boller
	Prof. dr. ir. R. H. Hoekstra
	Dr. C. M. Lyneis

ISBN : 978-90-367-5189-6 (printed version)

ISBN : 978-90-367-5192-6 (electronic version)

Contents

Chapter 1

INTRODUCTION

1.1 General introduction

The invention of the ECR ion source [1] in the end of the 1970's and it's subsequent continuous development based on new RF and magnet technology has been an essential step for research programmes utilizing secondary radioactive ions in various accelerator laboratories around the world such as the TRIμP program at KVI [2], the FAIR program at GSI [3], the Radioactive Ion Beam Factory at RIKEN [4], the Facility for Rare Isotope Beams (FRIB) at NSCL [5] and the SPIRAL2 project at GANIL [6], which require primary beams of highly charged ions of all elements up to uranium. Also atomic physics research depends on ECR ion sources when studying the interaction of highly charged ions with atoms, ions and surfaces. In addition to physics research, ECR ion sources are also used in industrial applications such as ion beam etching, implantation and ion beam sputtering deposition, etc.

Generally an intense multiply-charged ion beam is extracted from an ECR ion source, transported in a low-energy beamline and injected into one or a series of accelerators for acceleration to high energies. Cyclotrons are often equipped with an ECR ion source. As in a circular accelerator, such as a cyclotron or synchrotron, the maximum energy is proportional to the square of the charge-state (q^2), the use of higher charge-state ions can reduce the accelerator size and thus the facility costs. This gives a strong motivation to use an ECR ion source, which is capable of producing intense beams of high charge state ions. Furthermore, there are no cathode or filaments in the ion source and stable beams can be produced for long periods (days - months).

Over the last three decades, the performance of ECR ion sources in terms of charge state and current has been greatly improved by using ever higher microwave frequencies for ECR heating of the plasma and corresponding higher magnetic fields. This allows better plasma confinement and higher plasma density, resulting in a higher beam intensity and shift of the charge state distribution towards higher charge states [7–10]. However at the same time the higher magnetic fields and higher beam intensities result in a larger emittance. This is mainly due to angular momentum conservation in the axial magnetic field at the extraction region [11–13] and influence of the space-charge forces when the extraction current exceeds several milliamperes [14]. In addition to this ion beams extracted from an ECR ion source are not rotationally symmetric because of the magnetic-field geometry of the ion source [1]. Therefore, detailed understanding of the ion beam formation, extraction and transport of the intense ion beams is one of the key elements to meet the ever-increasing demands on the quality and intensity of highly charged ion beams and is equally important as ECR ion source improvement itself. The objective of this thesis is to improve the understanding of the physics of ion beam formation, extraction and transport including higher-order effects and correlations. We have applied our simulation tools to study and improve the overall efficiency and quality of the low energy beam transport system of the AGOR cyclotron.

The superconducting cyclotron (AGOR) at KVI is used for the acceleration of light and heavy ions [15]. The Advanced Electron Cyclotron Resonance (AECR) ion source [16] coupled to AGOR produces a variety of ion beams required by the experimental program at the AGOR facility. Present development work is mainly focused on increasing the beam intensities of the ECR ion source injector and optimizing the beam transport and injection into AGOR driven by the requirements of the experiments. At present the transmission of the beam from the ECR source analyzing system up to the cyclotron is at most 50 % due to an insufficient understanding of and control over the properties of the injected beams.

In order to achieve a high transport and injection efficiency in the low-energy beamline it is important to know the initial properties of the ion beam extracted from the ECR ion source and to prevent effective emittance growth during transport due to ion-optical aberrations and space-charge effects. Because of the large emittance of the ion beams extracted from the ECR ion source, the low energy beam transport (LEBT) is more critical than the high energy beam transport of the extracted beam. In general an ECR ion source possess a large beam size and divergence. Therefore, strong higher order effects (aberrations) cannot be avoided and have to be compensated to avoid a large increase of the acceptance of the ion optical system required for high transmission. A computational study has been undertaken to understand the processes that lead to a blow up of the effective emittance and to improve the ion beam transmission efficiency in an economical way. This study concentrates on the full three dimensional (3D) simulation of ion beam extraction and transport from an ECR ion source. The results of this thesis have been validated by measurements of the beam properties including its full 4D phase-space distribution.

1.2 Thesis outline

This thesis is organized as follows: Some aspects of ion beam transport along with the simulation tools used in this thesis are discussed in chapter 2. Chapter 3 briefly describes the physics involved in the production of multiply charged ion beams in an ECR ion source. In addition to this the computer code used for modeling of the ECR ion source is described. Chapter 4 describes the KVI-AECR ion source together with the low energy beamline diagnostic tools used in this study.

In order to make a clean comparison with beam profile and emittance measurements, particularly in the beamline section before the bending magnets, we have first studied the essentially mono-component He^+ beam. He^+ formation and the simulation of ion extraction and transport including space-charge are discussed in chapter 5. The results of the calculations are compared with measurements of the beam profiles and emittances. The simulation of multiple charge state neon beam formation and its extraction including space-charge are discussed in chapter 6. In addition to this the transport of a Ne^{6+} beam through the LEBT system up to the matching section is discussed. In chapter 7 a study to decrease the beam losses and improve the ion-optical properties of the analyzing magnet is discussed. In chapter 8 we discuss the application of our simulation approach to the formation, extraction and transport of Ar^{7+} and He^+ beams from the CAPRICE ECR ion source and EIS test bench installed at GSI, Darmstadt, while in the last chapter some general conclusions on the design of ion optical systems for the transport of large emittance low energy ion beams are given and perspectives for further work are sketched.

Chapter 2

THEORY OF ION BEAM TRANSPORT

2.1 Introduction

An ion beam transport system consists of focusing, deflection and often additional energy or momentum selection elements. Most often these devices are magnetic elements, although at low beam velocity electrostatic elements are also used. To provide focussing in both transverse planes solenoids, Einzel lenses or multiplets of quadrupoles are used. Usually various beam transport configurations can be used to achieve the same beam properties. However, the system design always represents a compromise between flexibility, ease of operation, complexity and cost. In order to achieve a high quality beam transport a thorough understanding of the beam requirements at the end of the system and of the beam characteristics at the start of the line are crucial.

The physical principles of multiply-charged ion production in ECR ion sources and the extraction of intense multiply-charged ion beams will be discussed in chapter 3. In this chapter we describe the basic principles of ion beam transport in section 2.2. Causes of beam distortions are discussed in section 2.3. Simulation tools used in the transport calculations are briefly described in the last section 2.4.

2.2 Ion beam transport

In order to optimize the performance of a charged particle transport system it is very important to understand two aspects of charged particle dynamics, i.e. the single-particle dynamics in external electric and/or magnetic fields and the collective effects caused by the electric and magnetic fields generated by the beam itself. In this section the basics of single particle dynamics in external electric/magnetic fields are discussed.

In general optical elements are either magnetic or electrostatic devices depending upon the applications. In the case of high energy beams magnetic devices are used, because for relativistic particles ($v \approx c$) the force due to a magnetic field of 1 T, which is easily produced, is equivalent to that for an electric field of 300 MV/m, which is practically impossible to achieve [17]. For low energy beams ($v << c$) this is not an issue and other considerations come into play. Quadrupoles and bending magnets along with field free drift spaces are the main building blocks of a beam transport system. The function of a quadrupole is focusing, while the electrostatic and magnetic bends provide guiding and focusing.

2.2.1 Charged particle motion

A *beam* is an ensemble of charged particles that moves along a straight or curved path, usually defined as the longitudinal direction and that are confined in the transverse direction by external magnetic or electric fields [18]. The dynamical state of each individual particle is at any given instant of time defined by three space coordinates (x, y, z) and three momentum coordinates (p_x, p_y, p_z). The six dimensional (6D) space spanned by the three spatial and three momentum components, i.e. (x, y, z, p_x, p_y, p_z) is known as *phase-space*. The transport of a beam through a beamline can be visualized as a flow of the beam particles in phase-space. *Liouville's theorem* states that the density of particles or the volume occupied by a given number of particles in the 6D phase-space remains invariant as one moves along with the flow although the shape of the volume may change continuously. In other words, the phase-space flow of the beam particles is incompressible. This theorem is valid if the forces acting on the particles are conservative and differentiable. These conditions are mostly met in beam transport systems, provided collisions between particles can be neglected. In some cases Liouville's theorem is violated, e.g. electron cooling, stochastic cooling and synchrotron radiation.

The force acting on a point charge q in an electromagnetic field (Lorentz force) is given by $F = q(E + v \times B)$. The motion of a charged particle due to the Lorentz force is determined by Newton's equation

$$\frac{dp}{dt} = F = q(E + v \times B) \tag{2.1}$$

with p the momentum of the charged particle. The particle's trajectory can be determined by solving Newton's equation for a given configuration of electric E and magnetic fields B.

In general the trajectory of a charged particle through the optical elements can be calculated in two ways: either analytically using an expansion of the equation of motion in a power series of the coordinates up to a given order or by integrating the equation of motion numerically. Here, we briefly describe the analytical method and introduce various important beam parameters. This helps to understand the basic principles of beam dynamics through a beam transport system. Numerical tools used in this thesis will be discussed in Sec. 2.4.

Let us consider a local Cartesian coordinate system $(x,\ y,\ z)$ to describe the trajectory of a particle in the vicinity of the reference trajectory (i.e. the optical axis). The origin of this coordinate system moves along the reference trajectory of the beam. The horizontal, vertical and longitudinal (beam direction) axes are labeled x, y and z, respectively. Instead of the $(x,\ y,\ z,\ p_x,\ p_y,\ p_z)$ phase-space coordinates it is customary in beam physics to use the set $(x,\ x',\ y,\ y',\ l,\ \delta)$. In this notation x' and y' are defined as dx/ds and dy/ds, where s is the coordinate along the reference trajectory, while l is the path length difference and δ the fractional momentum deviation between an arbitrary particle and the reference particle. The dynamical state of a beam particle at any given time t is fully defined by the 6D state-vector $X = [\,x,\ x',\ y,\ y',\ l,\ \delta\,]^T$. The time evolution of the beam is obtained by integrating the Newton-Lorentz equation of motion (Eq. 2.1). Its solution can be viewed as a 6D mapping of the phase-space, i.e.

$$\overrightarrow{X}(1) = \overrightarrow{F}_{0\to 1}(\overrightarrow{X_0}) \tag{2.2}$$

This mapping is generally speaking nonlinear, but beam transport systems are designed in such a way that the nonlinearities are small so that a power expansion of equation 2.2 converges rapidly. The power expansion of equation 2.2, which obtained directly from the power expansion of the equation of motion, can be written as

$$X_i(1) = \sum_j R_{ij} X_j(0) + \sum_{j,k} T_{ijk} X_j(0) X_k(0) + \ldots \tag{2.3}$$

with X_i the i-th component of the particle's state vector X, R_{ij} the first-order and T_{ijk} the second-order coefficient of the transfer map F. In linear systems where all higher-order terms in equation 2.3 are neglected one can represent each beamline element with its characteristic transfer matrix R, so that the transfer matrix of the entire line is simply the product of the matrices of the successive beamline elements [19].

However, low energy ion beams as considered in this thesis generally have large cross-sections and divergences, so that the higher-order terms in the power expansion (Eq. 2.3) are important. Solution methods based on power expansions then become very cumbersome and it is much more practical to numerically integrate the equation of motion (Eq. 2.1).

2.2.2 Beam emittance

A real beam consists of many particles and each particle can be represented by a point with coordinates $(x,\ x',\ y,\ y',\ l,\ \delta)$ in the 6D phase space. The phase-space density

$f(x,\ x',\ y,\ y',\ l,\ \delta)$ is defined such that $f(x,\ x',\ y,\ y',\ l,\ \delta)dxdx'dydy'dld\delta$ is the number of particles in the 6D volume-element $dV = dxdx'dydy'dld\delta$. The total number of beam particles N is then given by

$$N = \int f(x,\ x',\ y,\ y',\ l,\ \delta)dxdx'dydy'dld\delta \tag{2.4}$$

By dividing the phase-space density f by the number of beam particles N we get the normalized phase-space density $\rho(x,\ x',\ y,\ y',\ l,\ \delta) = \frac{1}{N} f(x,\ x',\ y,\ y',\ l,\ \delta)$, which is convenient for calculating various phase-space averages.

In many cases there is no correlation between the four transverse coordinates (x, x', y, y') and the longitudinal coordinates $(l,\ \delta)$, so that the phase-space density can be factorized into a transverse and longitudinal one: $\rho(x,\ x',\ y,\ y',\ l,\ \delta) = \rho_t(x,\ x',\ y,\ y')\ \rho_l(l,\ \delta)$. For many beamline elements, e.g. drift sections, Einzel lenses, quadrupoles and bending magnets, the 4D transverse phase-space distribution $\rho_t(x,\ x',\ y,\ y')$ can be separated in horizontal and vertical 2D distributions: $\rho_t(x,\ x',\ y,\ y') = \rho_x(x,\ x')\ \rho_y(y,\ y')$. However, solenoids and skew quadrupoles couple the two transverse phase spaces and for these elements one has to consider the full transverse phase-space distribution $\rho_t(x,\ x',\ y,\ y')$. As we are in this thesis only considering DC beams with a very small momentum spread ($\Delta p/p \leq 2.5 \times 10^{-4}$) we do not consider the longitudinal phase space. In the remainder of this section we will assume that the horizontal and vertical phase spaces are decoupled.

In the first-order formalism the so-called σ-matrix is used, which transforms as

$$\sigma(1) = \mathbf{R}\sigma(0)\mathbf{R}^T \tag{2.5}$$

The elements of the σ-matrix are the second-order moments of the phase-space density distribution $\rho(x,x')$, i.e.

$$\sigma = \begin{pmatrix} \overline{x^2} & \overline{xx'} \\ \overline{xx'} & \overline{x'^2} \end{pmatrix} \tag{2.6}$$

Here the overbar denotes a phase-space average of a function $g(x,\ x')$ defined by

$$\overline{g(x,x')} = \iint g(x,x')\rho(x,x')dxdx' \tag{2.7}$$

The product $X^T\sigma^{-1}X = 1$ with row vector $X^T = (x,\ x')$ defines the phase-space ellipse, which has an area A_x given by

$$A_x = \pi\sqrt{det(\sigma)} = \pi\sqrt{\sigma_{11}\sigma_{22} - \sigma_{12}^2} \tag{2.8}$$

It contains a certain fraction of the beam particles which depends on the phase-space distribution function $\rho(x,\ x')$. An example of such a phase-space ellipse is shown in Fig. 2.1. The tilt of the ellipse indicates a correlation between x and x' which shows

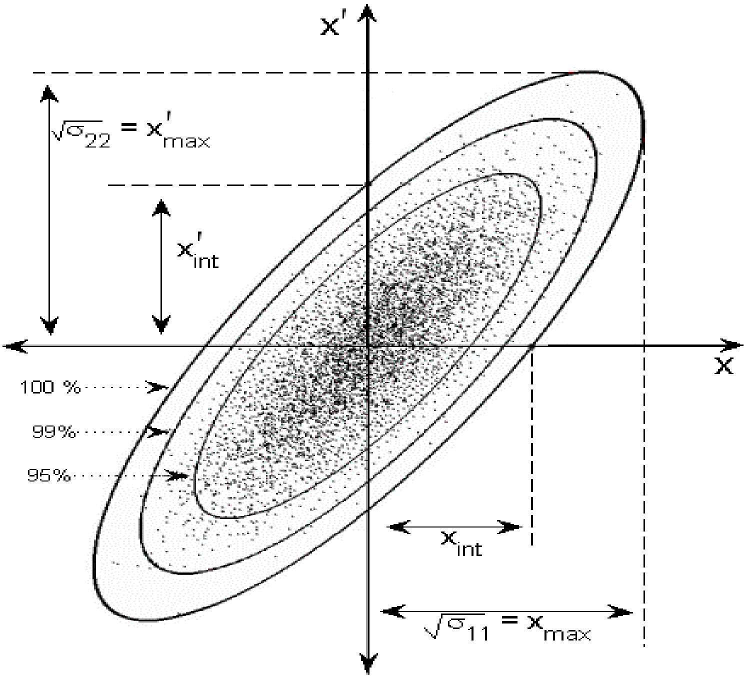

Figure 2.1: *A two dimensional phase-space ellipse (adopted from Ref. [20]).*

whether the beam is divergent (positive tilt angle, $\sigma_{12} > 0$), convergent (negative tilt angle, $\sigma_{12} < 0$) or at a so-called beam waist (tilt angle = $0°, 90°$, $\sigma_{12} = 0$). The area A_x of the phase-space ellipse is related to the so-called root-mean-square (rms) beam emittance $\varepsilon_{xx'-rms}$ defined as:

$$\varepsilon_{xx'-rms} = \frac{A_x}{\pi} = \sqrt{\sigma_{11}\sigma_{22} - \sigma_{12}^2} \tag{2.9}$$

The rms-emittance of a beam is an important quality parameter, i.e. the smaller its value the higher the beam quality for a given beam current. Following Lapostolle we define the effective rms-emittance as [21]

$$\varepsilon_{xx'} = 4\varepsilon_{xx'-rms} \tag{2.10}$$

It can be shown that for a beam with a uniform phase-space distribution the phase-space ellipse with area $A_x = \pi\varepsilon_{xx'}$ contains all the beam particles while for a Gaussian phase-space distribution it encompasses 90% of the beam particles [22]. From now on we will denote the effective rms-emittance simply as the effective emittance.

According to Liouville's theorem the area of the phase-space ellipse and thus also the

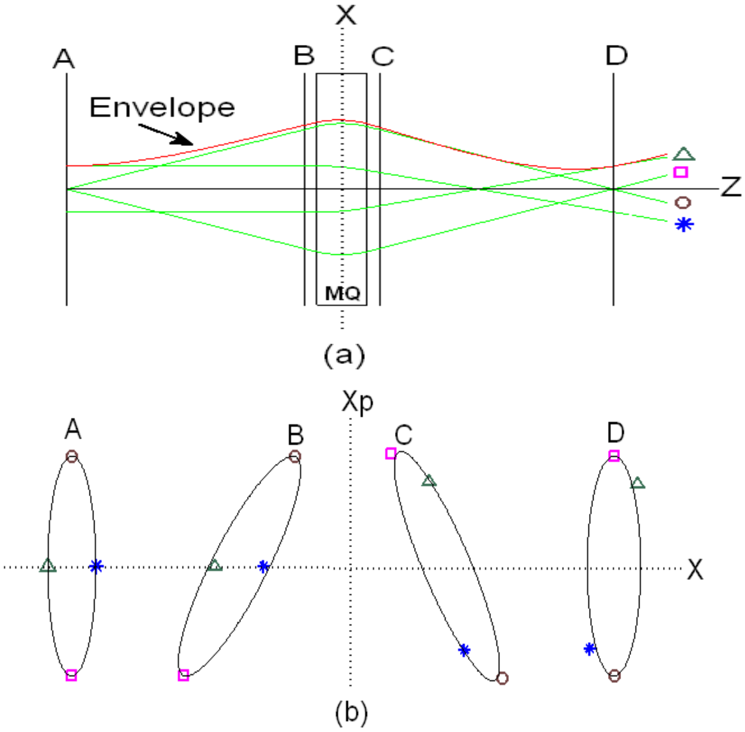

Figure 2.2: *Simulated ray trace and beam envelope through a magnetic quadrupole using the code COSY INFINITY [23]. Configuration-space view (a) and transverse phase-space views in (x,x') plane at different locations (b).*

effective emittance is conserved during beam transport as long as there are no collisions and the beam is not accelerated or decelerated, although the shape and orientation of the ellipse change continuously [22]. This is illustrated in Fig. 2.2 which shows the transport of a beam through a beamline consisting of two drift spaces and a magnetic quadrupole. Both individual ion trajectories, the beam envelope and a few phase-space ellipses at different positions along the beamline are plotted.

As we already mentioned the transport of low-energy beams often suffers from nonlinearities and tends to be non-paraxial. Because of these effects the simple linear matrix transformations no longer hold, i.e. ellipses do not transform into ellipses. Nonlinear forces cause a distortion of the phase-space distribution as is illustrated in Fig. 2.3. Although according to Liouville's theorem the phase-space area occupied by the beam particles does not change during the beam transport, the effective emittance $\varepsilon_{xx'}$ does increase because of ion-optical aberrations and/or nonlinear space-charge forces.

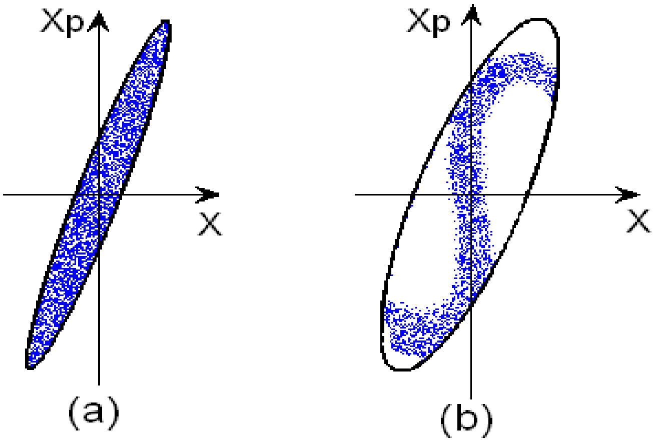

Figure 2.3: *Transverse phase-space area of the beam due to linear forces (a) and due to non-linear force (b).*

When the beam is accelerated the effective emittance $\varepsilon_{xx'}$ will decrease because of a decreasing beam divergence. In order to compare beam emittances at different beam energies it is better to take this trivial dependence into account by defining the so-called normalized effective emittance $\varepsilon_{xx',n}$ as

$$\varepsilon_{xx',n} = \beta\gamma\varepsilon_{xx'} \tag{2.11}$$

with $\beta = v/c$ and $\gamma = 1/\sqrt{1-\beta^2}$ the relativistic factor. According to Liouville's theorem the normalized effective emittance $\varepsilon_{xx',n}$ is invariant for all energies as long as collisions are not important and the beam transport is linear.

2.3 Beam distortion

During beam transport the emittance of the beam should be matched to the acceptance of the optical elements in order to avoid losses. In general the effective emittance of the ion beam increases due to optical aberrations and nonlinear space-charge forces, which leads to mismatch between the emittance of the transported beam and the acceptance of the optical elements and/or accelerator and consequently to beam losses. The increase of the effective emittance is in particular an issue for low energy ion beams. They have a small (magnetic) rigidity so one has the tendency to use short optical elements resulting in important contributions from the fringe fields, which are responsible for nonlinear effects. Image aberrations in the low energy beamline are often large because of the large filling factors. The most important causes of effective emittance growth in LEBT

Index	Multipoles	Term	Effect
n = 0	Dipole	$\frac{q}{p_z}B_{y0}$	Deflection
n = 1	Quadrupole	$\frac{q}{p_z}\frac{dB_y}{dx}x$	Focusing
n = 2	Hexapole	$\frac{q}{p_z}\frac{1}{2!}\frac{d^2B_y}{dx^2}x^2$	2^{nd} order correction /Chromaticity compensation
n = 3	Octupole	$\frac{q}{p_z}\frac{1}{3!}\frac{d^3B_y}{dx^3}x^3$	3^{rd} order correction

Table 2.1: *The most important multipoles and their principle effects on the beam transport [24,25]*

.

are nonlinearities in the applied forces and self-fields (space-charge forces of the beam). These will be discussed in the following subsections.

2.3.1 Optical aberrations

Each multipole has a different effect on the path of the charged particle. The most important multipoles and their purpose are listed in table 2.1. In addition to their main purpose higher-order multipoles with $n \geqslant 2$ introduce aberrations during beam transport [24].

Different higher order terms in the expansions of the transfer function cause various types of image aberrations, which result in distorted phase-space distributions of the beam transported through the optical elements. Quadrupoles and rotationally symmetric lenses have a straight optical axis. In these systems the imperfectly formed electrodes and pole face cause higher order aberrations and this could be an odd order aberration $(n = 3,5,...)$, because all electromagnetic forces are anti-symmetric with respect to the horizontal (x) and vertical plane (y).

Mid-plane symmetric systems such as magnetic or electric bending systems have a curved optical axis. As in the case of quadrupoles, here also higher multi-pole fields are added by imperfectly formed electrodes or pole faces. In the case of mid-plane symmetric systems aberrations of even order can exist $(n = 2,\ 4,...)$, since all electromagnetic forces are symmetric with respect to the midplane $(y = 0)$ in the bending plane (x) and antisymmetric in the non-bending plane (y). The magnetic flux density distribution $B_y(x,\ 0)$ proportional to x^n influences only image aberrations of nth and higher order but not aberrations of smaller than nth order. For example a hexapole magnet can be used to correct the second order image aberration produced by a dipole. In order to do this the hexapole strength $(n = 2)$ is adjusted in such a way that the overall second-order coefficient vanishes. Aberrations of $n = 4,\ 6,...$ are modified slightly but aberrations of zeroth and first order, i.e. the deflection of the beam and position of the image, are unchanged [24]. In addition to the image aberrations dipoles and quadrupoles also introduce chromatic aberrations.

In order to achieve a high quality beam transport it is important to minimize and/or correct optical aberrations as much as possible. Aberration correction or compensation can be achieved by using higher-order multipole fields at suitable locations in the system [24].

2.3.2 Space-charge effects on ion beam transport

In addition to the guiding fields (focusing/bending) the beam generates internal fields which, depending on the beam intensity, can influence the beam properties significantly. These are the electric fields caused by the space-charge and magnetic field of the ion beam current. The radial or transverse electromagnetic field that is generated by the beam as a whole can have a major influence on the trajectories of individual particles in the beam. For a cylindrically symmetric beam with uniform charge density ρ_0 and velocity v the radial electric field E_r at a distance r is given by (Coulomb's law)

$$E_r = \frac{1}{2\varepsilon_0}\rho_0 r \tag{2.12}$$

Similarly, for the azimuthal magnetic field (Ampere's law)

$$B_\varphi = \frac{1}{2}\mu_0\rho_0 v r \tag{2.13}$$

The total force acting on a beam particle is then [17]

$$F_r = e(E_r - vB_\varphi) = \frac{e\rho_0 r}{2\varepsilon_0\gamma^2} \tag{2.14}$$

In the case of a high energy beam $(v \approx c)$ the repulsive force due to the electric field is almost completely compensated by the attractive force due to the magnetic field. In a low energy ion beam the magnetic component can be neglected with respect to the electric component [26].

It is important to note that as long as the space-charge forces are linear (e.g. in a beam with uniform particle density) the effective emittance does not increase. However, in practice beam density is often non-uniform which can lead to an increase of the effective beam emittance because of nonlinear space-charge forces.

In practice collisions of beam particles with residual gas atoms and interactions with the walls generate secondary electrons in the beamline. These electrons become trapped in the electrostatic field of the beam, thereby reducing the effective charge density in the beam. This process is called space-charge compensation. Depending on the degree of space-charge compensation the radial electric field and the defocusing it causes are reduced [27]. The degree of space-charge compensation depends on the particular low energy ion beam transport design and the residual gas pressure [28]. Space-charge compensation is not efficient in ultra high vacuum pressures and in systems with electrostatic focusing and/or bending elements. In order to minimize the influence of the space-charge effect in the transport of intense ion beams it is essential to provide a high degree of space-charge compensation within the beam transport system by means of carefully optimizing the gas pressure along the beamline [28–30]. However, increasing the gas pressure also reduces the ion current via charge exchange processes. In Ref. [31] it has been shown that the emittance values decrease with increasing gas pressure. Comparison of measurements and simulations conducted at LBNL for helium beams give an estimate of 80 % compensation for beamline pressures in the 10^{-8} *mbar* range [32].

2.4 Computational tools

Computer codes play an important role in the understanding of ion beam transport and beamline design and optimization. In this thesis four different codes have been used according to the specific issues addressed, which are briefly described in this section.

The initial 6D phase-space distribution of the ions at the extraction aperture of the ECR ion source is calculated with a PIC-MCC code developed at KVI [33]. This code is described in Sec. 3.4 of this thesis. The General Particle Tracer (GPT) code and the LORENTZ3D code have been used to simulate the extraction of an ion beam from the ECR ion source and its subsequent transport through the low-energy beamline. The code COSY INFINITY has been used for the beam envelope calculation from the analyzing magnet to the matching section of the cyclotron injection system. GPT and LORENTZ3D are commercially available codes, while COSY INFINITY is in the public domain. A survey of computer codes available for simulating the behavior of charged particle beams including space-charge effect is given in Ref. [34].

2.4.1 LORENTZ3D-EM

LORENTZ3D-EM [35] is a combined 3D electrical and magnetic field solver package that incorporates ray tracing. To solve both electrostatic and magnetic problems LORENTZ3D uses the so-called Boundary Element Method (BEM) [36] and Finite Element Method (FEM) hybrid solvers. The advantage of this code is that problems with complex geometry and nonlinear material properties can be modeled. Space-charge effects can be taken into account in an iterative way.

In our simulations we used this code to calculate the full 3D magnetic fields of the AECR ion source's solenoid and hexapole magnets, the magnetic field of the analyzing magnet and the electrostatic fields of the accel-decel extraction system. In addition to this, the optimization of the design of the 110° analyzing magnet has been performed using the ray tracing functionality of the code.

2.4.2 GPT

The General Particle Tracer (GPT) code [37] is a full 3D code tracking particles through the electromagnetic fields of optical elements and the self-fields. This code has been used to study non-linear effects of charged-particle dynamics in the extraction region and beam transport through the analyzing magnet. The techniques used in the GPT code are described in detail in Ref. [38]. The initial particle distribution, 3D electromagnetic field configuration (optical element), the required accuracy of the calculations and the output method are specified in an input file.

The initial particle distribution consists of a number of macro-particles, each typically representing a large number of real particles and can be produced by using a built-in particle generator. In our case the 6D phase-space distributions from the ECR ion source calculated with the PIC-MCC code were used as input for GPT.

The fields of physical structures are represented by so called elements. Most standard beamline components are represented in GPT. Built-in models have been used for the quadrupoles and bending magnets. GPT allows bending magnets with rotated pole faces and fringe fields. The fringe fields are modeled with a second order Enge function [38]. Also 2D field maps of ion-optical elements calculated by external programs like POISSON/SUPERFISH and 3D field maps computed with LORENTZ3D can be used in GPT. We used this option for the ECR ion source solenoid, hexapole, electrostatic extraction system and the magnetic focussing solenoid of the GSI-EIS Beamline (see chapter 8). The equation of motion for the macro-particles is solved using a 5th order embedded Runge-Kutta integrator with adaptive step-size control.

In order to calculate particle trajectories including space-charge forces we used a 2D point-to-line model for continuous beams. In this model every particle represents a complete line and the force on each particle depends on the position of all other particles. A mean field approximation is used for the interaction between the particles and collisions between individual particles are neglected.

GPT is computationally fast compared to LORENTZ3D, but lacks the electric and/or magnetic modeling of a real geometry. We have used GPT for trajectory calculations including space-charge forces and calculated the 3D electric/magnetic fields with the LORENTZ3D code.

2.4.3 COSY INFINITY

COSY INFINITY is well suited for studying aberrations of ion-optical systems, because one can include arbitrary orders in the beam dynamics simulation [23] using the so-called the Differential Algebraic (DA) approach [39]. It allows the study of accelerator lattices, spectrographs, beamlines, electron microscopes and it is quite useful to calculate the ion beam envelope quickly. We used this code to study the aberrations of the KVI-AECR

110° analyzing magnet and for beam envelope calculations of the entire beamline up to the matching section.

Chapter 3

ELECTRON CYCLOTRON RESONANCE ION SOURCE

3.1 Introduction

Electron Cyclotron Resonance (ECR) Ion Sources are used to produce intense, high charge state ion beams of intermediate and heavy mass elements [1]. They are widely used to produce ion beams for accelerators, atomic physics research and industrial applications. In order to achieve ever higher intensities of ever higher charge states ion beams it is essential to obtain an in-depth understanding of not only the processes in the plasma of the ECR ion source but also of the beam formation, extraction and transport of the multiple-charge state and multi-component ion beams they produce.

In this chapter we discuss aspects of the physics and technology of ECR ion sources that are relevant for the work described in this thesis. First the historical development of ECR ion sources is briefly outlined in section 3.2. In order to understand the beam formation and extraction processes ECR ion source fundamentals are presented in section 3.3. Finally, a brief review of ECR ion source modeling including the Particle-In-Cell Monte-Carlo Collision (PIC-MCC) and KOBRA3-INP codes used in this study is given in section 3.4.

3.2 Brief history of the ECR ion source

The history of the ECR ion source starts in the late 1960s, when Electron Cyclotron Resonance Heating (ECRH) was developed as a technique to heat the plasma in magnetic confinement devices used in fusion research [1]. In 1969 it was proposed to produce high charge state ions in plasma devices using ECRH [40]. The first sources using ECRH to produce multiply charged ions were developed in 1972 in France by Geller et al. [41] and in Germany by Wiesemann et al. [42]. In 1974 Geller and his co-workers made a major step towards the ECR ion source by transforming a large mirror device (CIRCE) [43] into an ion source, SUPERMAFIOS [44]. SUPERMAFIOS was equipped with solenoids to generate an axial magnetic field and a hexapole magnet to produce a radial field. The superposition of the hexapole and solenoid fields produces a minimum-B magnetic field configuration that stabilizes the plasma against MHD instabilities [45]. It does this by creating closed ellipsoidal iso-B surfaces inside the plasma chamber with a magnetic field increasing in all directions from the center to the walls of the plasma chamber. At one of these surfaces the electron Larmor rotation is resonant with the injected microwaves and a very efficient heating of the plasma electrons is achieved. However, the electrical power consumption of this source was still very high $(3\ MW)$. The next step involved the development of lower power consumption sources by using high strength permanent magnets (NdFeB) for in particular the hexapole field. For example the MICROMAFIOS 10 GHz (1979) and CAPRICE 10 GHz (1983) ion sources with a power consumption of about 50 kW were realized by using solenoids for the axial field and NdFeB magnets, while the NEOMAFIOS 8 GHz source built in 1986 used NdFeB permanent magnets for both the axial and radial magnetic field.

An advanced ECR ion source (AECR) for the production of high charge state ions was built in 1990 by the LBNL ECR ion source group and upgraded (AECR-U) [46,47] in 1996. Slightly modified versions of this source are in operation at JYFL [48], KVI [49], Texas A&M University [50], NSCL [51], and ANL [52]. Meanwhile other laboratories around the world have also developed and successfully put ECR ion sources into operation (e.g. DECRIS in Dubna [53], ECR4 in GANIL [54], GTS in CEA/Grenoble [55], SERSE in Catania [56] and 18 GHz source at RIKEN [57], etc.). Nowadays ECR ion sources have matured to the level that they are commercially available.

As a result of three decades ECR ion source development a remarkable source performance has been obtained, e.g. the beam intensity of Ar^{8+} has increased from a few tens of μA to 2 mA [58]. This has mainly been achieved by using higher frequency microwave power and an accordingly increased magnetic field. In 1987 Geller and co-workers published semi-empirical scaling laws for optimizing ECR ion source design [59]. The most important scaling law is that the extracted beam intensity scales with the square of the microwave frequency. However, the use of normally conducting solenoids and permanent magnet multipoles limits to the frequency of the microwave power of about 18 GHz [60]. Advances in superconducting magnet technology have made it possible to use the ever higher frequency microwave sources developed for radar and satellite communication also in ECR ion sources. This has resulted in the emergence of the third generation ECR ion sources (e.g. VENUS, SECRAL, RIKEN-SC, SERSE, SUSI, etc.). A detailed account of the historical development of ECR ion sources can be found in references [1,61–63].

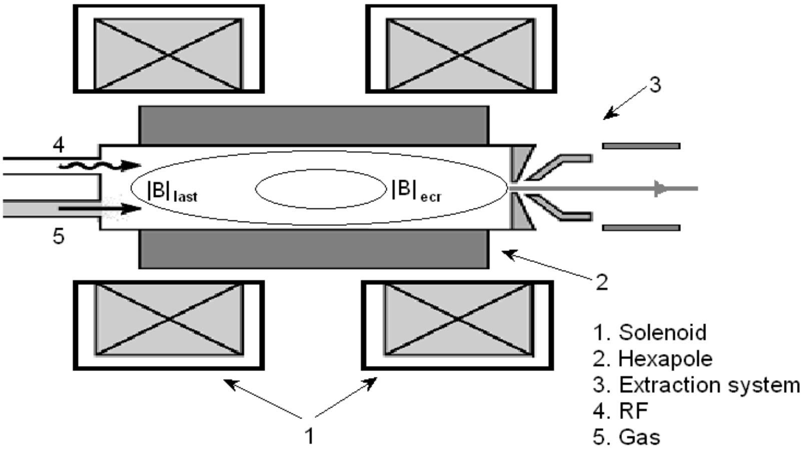

Figure 3.1: *Schematic view of an ECR Ion Source.*

3.3 ECR ion source fundamentals

Figure. 3.1 shows a schematic drawing of an ECR ion source. Its main components are: *a)* Plasma chamber and vacuum system. *b)* Solenoid and hexapole magnets for axial and radial confinement of the plasma, respectively. *c)* Injection of neutral atoms or molecules (by oven, gas inlet, etc.) to be ionized. *d)* RF power input with appropriate frequency which is the source of energy for the electrons, so that high charge state ions can be created via successive ionization. *e)* Ion extraction system for the ion beam formation.

3.3.1 Magnetic confinement

The main draw back of a simple mirror structure (without hexapole) is that macroscopic plasma instabilities (e.g. MHD instabilities) are excited because the plasma pressure radially decreases with the magnetic field [1]. The plasma will therefore quickly escape in the radial direction from the trap. Therefore, in most ECR ion sources a multipole field, usually a hexapole, producing a radially increasing field is superimposed on to the mirror field to stabilize and thus better confine the plasma. This results in a so-called *minimum-B (min-B)* structure because the magnetic field strength has a minimum in the center of the structure and increases from there in all directions (Fig. 3.2a). Fig. 3.2b shows a 3D view of the resultant magnetic field of an ECR ion source. The $iso-|B|$ surfaces (magnetic isobars) in a min-B magnetic configuration are closed nested shells.

In a magnetic mirror charged particles that move exactly parallel to the magnetic field lines ($v_\perp = 0$) have no magnetic moment and are immediately lost from the trap.

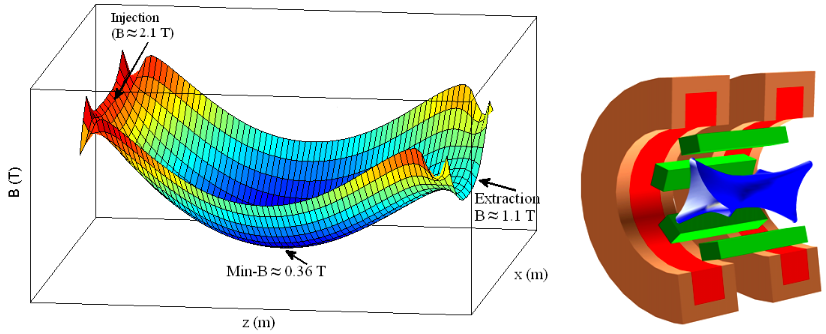

(a) **(b)**

Figure 3.2: *Typical (Min-B) magnetic structure of a 14.1 GHz ECR ion source (a) and 3D view of ECR ion source magnetic field configuration (figure taken from Ref. [64]) (b).*

Particles that have no parallel velocity $(v_{\parallel} = 0)$ are trapped forever. Whether or not a charged particle remains trapped depends on the ratio of the perpendicular and parallel velocity components, which defines the pitch angle α:

$$\tan(\alpha) = \frac{v_{\perp}}{v_{\parallel}} \tag{3.1}$$

When a particle moves in the direction of increasing magnetic field **B**, its perpendicular velocity increases because of the adiabatic invariance of the magnetic moment $\mu = \frac{mv_{\perp}^2}{2B}$ and consequently the parallel velocity has to decrease because of the conservation of total kinetic energy. Therefore, charged particles will bounce back and forth between the two high-field regions of the magnetic mirror, provided the perpendicular velocity component is large enough.

Since the magnetic moment (μ) of a particle is a conserved quantity, the pitch-angle at different axial positions z and z' only depends on the magnetic field:

$$\frac{\sin^2(\alpha)}{\sin^2(\alpha')} = \frac{B(z)}{B(z')} \tag{3.2}$$

The minimum pitch angle $\alpha_\circ$ at the midplane z = 0 (where the magnetic field has a minimum value B_{min}) for which a particle will be reflected at the position z = z' where the field has its maximum with value B_{max} is then

$$\alpha_\circ = \sin^{-1}\left(\sqrt{\frac{B_{min}}{B_{max}}}\right) = \sin^{-1}\left(\sqrt{\frac{1}{R_m}}\right) \tag{3.3}$$

with $R_m = B_{max}/B_{min}$ is the magnetic mirror ratio. The angle $\alpha_\circ$ defines the so-called *loss cone* [65, 66] in velocity space (Fig. 3.3). Particles inside the loss cone, i.e. $\alpha < \alpha_\circ$

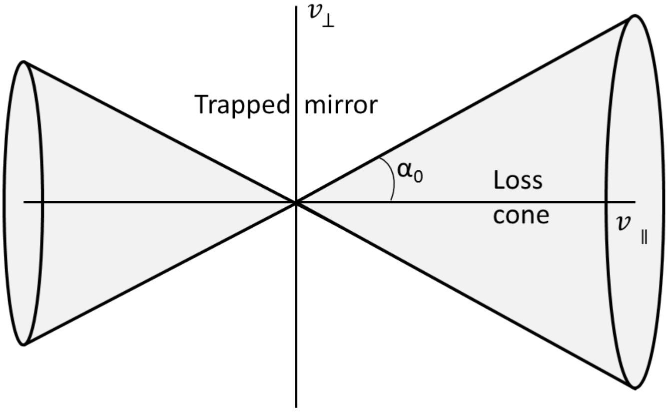

Figure 3.3: *Schematic view of the loss cone in the ECR ion source (Left cone: Injection side and Right cone: Extraction side).*

are not trapped and escape from the magnetic mirror system. Particles diffuse into the loss cone (and thus escape from the trap) through collisional scattering, microscopic instabilities, e.g. due to the interaction with the RF field, and non-adiabatic processes. Collisional scattering is often the dominant mechanism for diffusion into the loss cone. Collisional losses generally increase with plasma density and decrease with electron energy. A detailed analysis of the confinement of electrons and ions in an ECR ion source is complicated, since the magnetic confinement depends upon the ratio of the Larmor frequency and the collision frequency, which in turn depends on the energy and position of the particles. A global description of the dynamics of electrons and ions is given in the subsections 3.3.2 and 3.3.3.

For $R_m >> 1$ and assuming an isotropic velocity distribution the escape fraction ξ can be approximated as [1]

$$\xi \sim \frac{1}{2R_m} \tag{3.4}$$

For higher mirror ratios the confinement is better and consequently the production of high charge state ions is increased. On the other hand, the mirror ratio should not be too high since ions have to escape from the plasma trap in order to be extracted. Optimization of the mirror ratio is therefore one of the important elements in the design of ECR ion sources [56, 67–70]. For the KVI-AECR ion source, $R_m \sim 3.6$ and approximately 14 % of the particles escape immediately. The particle confinement time is determined by the probability to scatter into the loss cone.

3.3.2 ECR Heating

Plasma electrons trapped in the magnetic field of an ECR ion source follow helical paths along the field lines. The local frequency of the rotation around the magnetic field lines is the cyclotron frequency $\omega_{cyc} = eB/m$. By injecting microwave power with frequency ω_{RF} the electrons are accelerated or decelerated, depending on the phase of their gyration motion with respect to that of the local RF electric field, if the electron cyclotron resonance condition is fulfilled:

$$\omega_{RF} = \omega_{cyc} - k_{\parallel} v_{\parallel} \tag{3.5}$$

with ω_{RF} the wave frequency, $\omega_{cyc}(\overrightarrow{r})$ the cyclotron frequency of the particle at point r, $k_{\parallel}$ the RF wave vector and $v_{\parallel}$ the component of the electron velocity parallel to the magnetic field line. For $v_{\parallel} = 0$ equation 3.5 defines a surface in the min-B magnetic configuration of an ECR ion source, which is called the *resonance surface*.

The magnetic field at the resonance surface is given by $B \cong \frac{f_{RF}}{28}$, with B expressed in tesla and $f_{RF} = \omega_{RF}/2\pi$ the injected microwave frequency in gigahertz [1].

The study of electromagnetic wave propagation and ECR heating in a plasma is complicated due to collective phenomena. In a min-B configuration, electrons cross the resonance region many times and may, depending on the phases between their motion and the RF field, gain or loose energy. However, the energy gain of an electron at the accelerating phases is higher than the energy loss in the decelerating phases. Therefore, the electrons undergo a global heating called *stochastic ECR heating* [71] and rapidly reach keV energies, sufficient to ionize the atoms via successive single ionizations [1]. The typical range of the electron density of ECR plasmas is between 10^{11} and 10^{12} cm^{-3} depending on ion source parameters [72].

ECR plasmas are far from thermodynamical equilibrium and the electron energy distribution function (EEDF) is strongly non-Maxwellian [73]. Because of the confinement and the ionization, collision and diffusion processes the electron energy varies from several tens of eV to several hundreds of keV. Although there is a continuum of electron energies, the EEDF can conveniently be represented by three populations the energies of which are connected to the diffusion, ionization and confinement processes [74]: a cold one ($E_{kin} \sim 1$–100 eV), a warm one ($E_{kin} \sim 100$ eV–100 keV), responsible for the ionization processes [1] and a hot one (energy above 100 keV up to a few hundred keV).

During their oscillation in the magnetic mirror, the electrons and ions can be scattered into the loss cone. Thus the confinement time for electrons is related to the scattering rate for electron-electron and electron-ion collisions. Due to their low collision rates high energy electrons are well confined. On the other hand the cold electrons suffer more frequent scattering collisions and are not magnetically confined. However, they remain confined by the space-charge field of the plasma ions. The cross-sections for ionization exhibit broad maxima centered at $E_e \geqslant 3W_{ion}$ [75], with W_{ion} the binding energy of the electron to be removed, which lies in the range 5 eV to 1.5 keV. Consequently the cold electrons hardly contribute to the ionization process and only serve as a source to replenish the population of higher energy electrons. Also the high energy electrons $(E_e > 100\ keV)$ do not significantly contribute to the ionization because of their low ionization cross-sections and low densities.

The production of multiply charged ions increases with microwave power up to a maximum after which it decreases because of RF induced plasma losses [76]. Stabilizing the plasma against RF induced instabilities is an important aspect of optimizing the source performance for the highest charge states. Injecting additional RF power at a lower frequency has been found to have such a stabilizing action: both the total RF power and the power at the upper frequency can be increased before instabilities occur resulting in a better performance of the source in terms of total intensity and charge state distribution.

3.3.3 Ion dynamics

The ECR plasma is a mixture of ions, electrons and neutrals that undergo collisions with each other. The charge-state distributions (CSD) of the beams extracted from an ECR ion source is strongly dependent on plasma parameters such as electron (n_e) and ion densities (n_q), temperatures, ion mass (m_i) and neutral density (n_0), etc. The steady-state rate equations for a specific species of multiply charged ion contain terms describing the ionization and loss processes. The loss processes include transport, radiative recombination and charge exchange. It has been shown that charge exchange and radiative recombination losses are relatively small compared to typical transport losses [77].

The colder electrons leave the ECR plasma faster than the ions due to their higher mobility. In order to maintain charge neutrality, the plasma therefore attains a positive potential with respect to the plasma chamber (the so-called *plasma potential*), which reduces the loss of low energy electrons by confining them electrostatically. The plasma potential in ECR ion sources has been extensively studied and reported in references [46, 76, 78]; depending on the conditions of operation of the source it lies in the range 10–50 V. In order to optimize the ECR ion source for multiply-charged ion production the ion temperature and the plasma potential should be as low as possible for better ion confinement [79].

Ions in the ECR plasma are confined by magnetic as well as electrostatic fields depending on the location of the ions and the plasma density. According to the model presented in Ref. [1, 80, 81] the ions in the core of the plasma ions are highly collisional and not confined by the magnetic mirror, but electrically confined by a negative potential dip created by the hot electrons. However, near the wall the ions are magnetically confined due to the low collisional rate caused by the reduced plasma density. The ions find their way to the ion extraction aperture, which is located on the axis of symmetry, through diffusion and scattering. The ions arriving at aperture in the plasma electrode are then accelerated by the applied extraction field, which is typically a few tens of *kV* potential difference with respect to ground.

We can summarize the general requirements for production of multiply charged ions in an ECR ion source as follows [1,82]:

1. **Sufficient electron energy**: The electron energy should be high enough to produce the required charge state. This can be satisfied by ECR heating with sufficient microwave power.

2. **Long ion confinement**: The ions must be confined long enough in order to achieve the required charge state via successive single ionizations. This is achieved by the min-B configuration

3. **High plasma density**: In order to maximize the ion current it is important to produce a high density plasma. This can be realized by heating with high frequency RF power and correspondingly high magnetic fields.

4. **Low background pressure**: For high charge state ion production a low background pressure is important to minimize recombination and charge exchange processes. This sets constraints to the gas pressure.

In addition to the general scaling laws the performance of ECR ion sources has also been continuously improved experimentally by the introduction of new design concepts and techniques, such as biased disk [83], wall coating [67], gas mixing [84,85], multiple frequency heating and tuning [86–89].

3.3.4 Extraction fundamentals

The performance of a source for highly charged ions is expressed in terms of beam brightness and charge state distribution. The plasma volume provides the ions, while the extraction system together with electric and/or magnetic fields of the source in the extraction region determine the properties of the ion beam extracted from the plasma volume. The particles passing through the extraction system acquire energy and a directed velocity in the electric and/or magnetic fields of the extraction system. Therefore, understanding the physics of an ion source extraction system is very important for the production of high intensity, high quality ion beams.

Depending on the application the extraction system can take many different forms, consisting of as many as five electrodes and widely different geometries [90]. In the simplest case two separate electrodes are used (see Fig. 3.4a). In ECR ion sources usually a three-electrode extractor design is used, with an additional electrode (V_{supp}), which is biased to a relatively low negative voltage, inserted between the plasma (V_{ext}) and ground

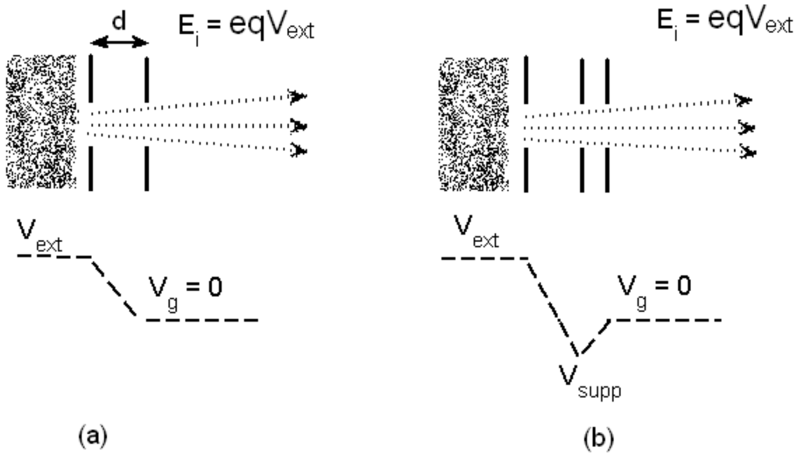

Figure 3.4: *Schematic view of two electrode extraction system (a) and three electrode extraction system (b). Figure adopted from Ref. [63].*

electrode (V_g) (Fig. 3.4b). This three electrode configuration is called an *accel-decel* extraction system, because ions are accelerated in the first gap and decelerated in the second gap. The middle electrode acts as a shielding electrode for the low energy electrons produced in the downstream region in order to improve the space-charge compensation for the extracted ion beam.

The ions available for beam formation at the plasma electrode have been transported from the inner region of the plasma by diffusion or plasma flow to the extraction region. When the plasma comes into contact with the plasma electrode a sheath with a thickness of the order of a Debye length (λ_D) is formed. The Debye length is given by

$$\lambda_D = \sqrt{\frac{\varepsilon_0 k T_e}{n_e e^2}} \tag{3.6}$$

where ε_0 is the permittivity of free space, k is the Boltzmann constant, e is the charge of the electron, T_e is the electron temperature and n_e is the electron density. In the ECR ion source the Debye length is typically a fraction of a millimeter. Ions in the plasma acquire a finite velocity directed towards the sheath boundary. Bohm showed that in order to satisfy the Poisson equation in the plasma sheath this velocity compound should exceed $\sqrt{kT_e/m_i}$ [91], with m_i the ion mass.

The quality of the extracted beam is determined by the trajectories of the ions in the extraction region. These are influenced by several factors, such as the applied electric field strength, the magnetic field in the beam formation region, the shape of the emitting plasma surface and the space-charge density in the resulting beam itself. The emitting 'surface' is the boundary between the plasma sheath and the ion beam, the so-called *plasma meniscus* [63]. Depending on the plasma density, extraction geometry and extraction voltage the plasma meniscus can vary between strongly convex and strongly concave. For a given geometry and voltage it will be convex at high plasma density, resulting in beam losses in the extraction system and concave at low density, leading to strong focussing and subsequent blow up due to space-charge forces if these are not properly compensated. Simulations indicate that the ideal shape of the plasma meniscus is a flat surface [63].

The current density of charged particles that can be extracted from the plasma by the electric field is limited by the plasma density and space-charge of the ion beam and can not exceed the Child-Langmuir law (assuming a planar plasma sheath and an ion beam without space-charge compensation [63, 66])

$$j_{sc} \simeq \frac{4}{9}\varepsilon_0\sqrt{2eq/m_i}\,\frac{V_{ext}^{3/2}}{d^2} \tag{3.7}$$

with ε_0 the vacuum permittivity, m_i is the ion mass, V_{ext} is the extraction voltage, and d is the length of the extraction gap (Fig. 3.4). This equation holds under space-charge limited conditions i.e. when the ion source is capable of producing more ions than can be removed at any time (space-charge limited mode) by the extraction system.

For positively charged ions with charge state q the energy E_i of the extracted ion beam is given by $E_i = eqV_{plasma}$, where $V_{plasma} = V_{ext} + V_p$. The plasma potential V_p is typically of order 10 V, and can usually be neglected ($V_p << V_{ext}$) in comparison with the extraction voltage of many kilo-volts.

In the above description it was assumed that there is no magnetic field in the beam formation region. In an ECR ion source, however, the ion beam formation and extraction is more complex due to the presence of a combination of electric and magnetic fields in the extraction region. This has a strong influence on the beam formation process.

(a) Position of the plasma electrode and ion confinement:

The position of the plasma electrode in an ECR ion source with respect to the magnetic configuration is an important parameter for the optimization of the production and extraction of the highly charged ion beam. In order to preserve the plasma confinement the extraction system should not influence the mirror reflection of the particles in the plasma. Therefore, it is generally located at the last closed $iso-|B|$ surface of the source (see Fig. 3.1). In this way only ions in the loss cone of the mirror are extracted.

There is a loss cone at both ends of the source, which are in general not identical in size because of the different magnetic field maxima at either end (see Fig. 3.2a). By using a larger axial magnetic field at the so-called injection side of the source (see Fig. 3.3) the loss cone at this side is smaller, resulting in a higher output of ions on the extraction side. The extracted ion current I_q of charge state q is approximately half the ion loss rate [1]

$$I_q \approx \frac{1}{2} \frac{n_q eqVol}{\tau_q} \tag{3.8}$$

where n_q is the density of the ions of charge state q, τ_q the ion confinement time; Vol is the part of the plasma volume that maps along the magnetic field lines into the extraction area, i.e. the plasma volume may not be the same for different ion species.

(b) Extraction geometry, potential, current and plasma meniscus:

The accel-decel system used in ECR ion sources generally has a Pierce-type plasma electrode (first electrode) and various shapes for the puller electrode (second electrode), while the grounded electrode (third electrode) is in most cases a simple cylindrical pipe. The Pierce theory was originally developed for electron guns assuming zero magnetic field, zero thermal energy and electrons uniformly emitted from a planar cathode. The Pierce theory is also applicable to positive ion beams by reversing the electric field direction and changing the charge to mass ratio of the electron to that of the ion. According to the Pierce theory, the plasma electrode should make an angle of 67.5° with respect to the optical axis to produce a transverse electrostatic field that exactly balances the space-charge field of the electron beam [92], assuming space-charge limited extraction conditions.

The plasma provides an ion current to the extraction aperture given by Eq. 3.8. Dividing this by the area of the extraction aperture gives the extracted current density j_{sc}, which should be equal to the space-charge limited current density, Eq. 3.7. This equality defines the shape of plasma meniscus and thereby the effective distance (d) in Eq. 3.7.

In an ECR ion source the shape of plasma meniscus is difficult to predict. It depends upon the plasma parameters, the shape of the plasma electrode, the extraction potential and the local magnetic field. The inhomogeneity in the plasma density across the extraction aperture leads to further complications of the plasma sheath model (see Eq. 3.6). A fully three-dimensional plasma sheath model for the ion extraction from an ECR ion source has not yet been developed.

(c) Magnetic field and ion temperature:

The loss of axial symmetry of the simple mirror field by the addition of the radial multipole field to create a min-B configuration has important consequences for the electron and ion trajectories in the trap. It causes according to calculations [93, 94] a triangular pattern in the plasma distribution at the injection and extraction sides, which is indeed observed in practice [95] (Fig. 3.5b and 3.5a). Fig. 3.5 shows the plasma sputter marks on the injection and extraction sides of the KVI-AECR ion source due to the ECR ion source magnetic field configuration (see Fig. 3.2b). The plasma density drops axially and radially outside the resonance zone [96, 97]. Therefore, the ion motion outside the resonance zone is dominated by the magnetic field rather than by collisions resulting in the triangular beam pattern.

Furthermore, Fig. 3.5b shows that the shape of the plasma facing side of the plasma

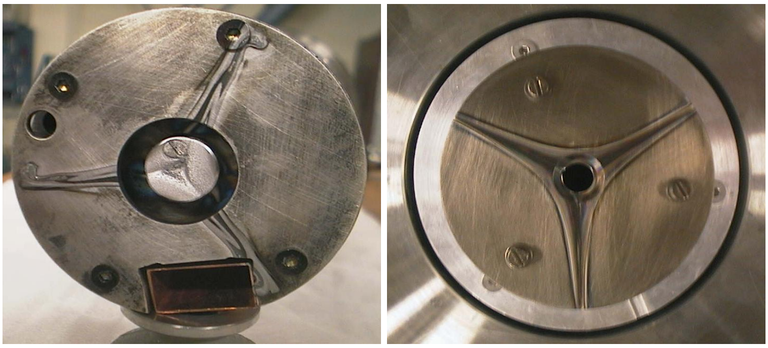

(a) (b)

Figure 3.5: *Injection plug with biased disk (a) and Plasma electrode (b).*

electrode is not very important in ECR ion sources, because the ions that are extracted have diffused from the plasma core that is concentrated around the plasma chamber axis [1]. The properties of the extracted beam are mainly determined by the local electric and magnetic fields between the plasma and puller electrodes [98, 99].

During the ion beam extraction from the ECR ion source the triangular beam pattern rotates due to the magnetic field in the extraction region. The angle of rotation is in first-order given by the following formula for magnetic lenses [100]:

$$\Theta = \sqrt{\frac{Q}{8 m_i V_{ext}}} \int B_z dz \tag{3.9}$$

with Q the charge of the extracted ion, V_{ext} the extraction voltage, m_i the mass of the extracted ion and B_z the axial magnetic field strength. This is illustrated in Fig. 3.6, where the angle of rotation as a function of the mass number to charge state ratio (m/q) for an extraction potential $V_{ext} = 24\ kV$ and $\int B_z dz \approx 0.077\ Tm$ has been plotted. The calculation has been done for the KVI-AECR ion source.

The emittance of the ion beam extracted from an ECR ion source is determined by two factors: (1) the ion temperature [12] and (2) the magnetic field in the extraction region of the ECR ion source [12, 13] (see Fig. 4.2b). To estimate both contributions to the emittance it is assumed that the electric field has no azimuthal variation, that the plasma density distribution is uniform across the aperture of the plasma electrode and that the ion temperature is given by a Maxwellian temperature distribution inside the plasma. The emittance of the ion beam extracted from the ECR ion source under these assumptions is given by [12]:

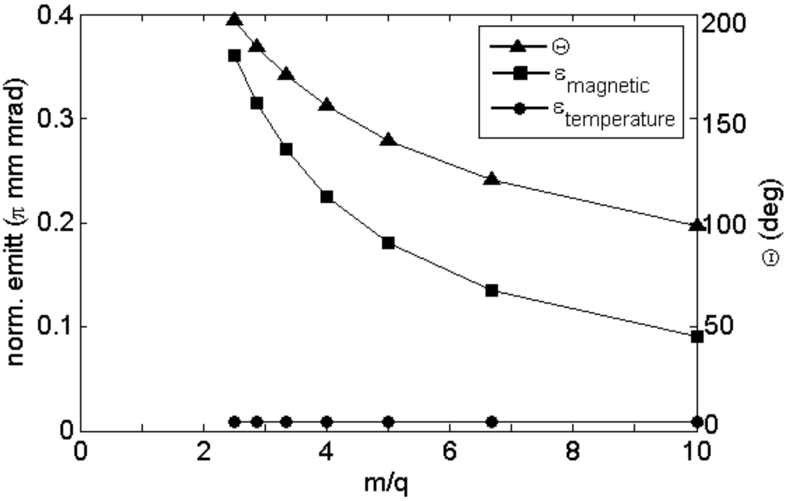

Figure 3.6: *Calculated normalized emittance values (left scale) and angle of rotation (right scale) for KVI-AECR ion source extraction conditions.*

$$\varepsilon = r_0\sqrt{\frac{kT_i}{2QV_{ext}}} + r_0^2 B_0\sqrt{\frac{Q}{8m_iV_{ext}}} \tag{3.10}$$

where r_0 is the aperture of the plasma electrode, k the Boltzmann constant, T_i the ion temperature, m_i the ion mass, Q the charge of the ion, V_{ext} extraction potential and B_0 the magnetic field at the aperture of the plasma electrode.

Fig. 3.6 shows the two contributions to the emittance as a function of m/q for the KVI-AECR ion source with typical extraction parameters ($r_0 = 4\ mm$, $B_0 = 1.1\ T$, $V_{ext} = 24\ kV$ and $kT_i = 1\ eV$ Ref. [101]). Eq. (3.10) shows that for a given atomic mass the emittance of the extracted ion beam is expected to be larger for higher-charge state ions. However, this is in contradiction with the general observation that higher charge state beams have a smaller emittance, as quantified by e.g. measurements of the emittance after the analyzing magnet of the AECR-U at LBNL [102]. Possible explanations based on plasma physics and ion production processes, such as a dependence of the radial transport on the charge-to-mass ratio of the particles, are proposed in Ref. [103]. Since highly charged ions appear to be concentrated more on the axis of the ECR ion source as compared to low charge state ions [93], the effective extraction radius is smaller for highly charged ions and thus their emittance as well.

3.4 ECR ion source modeling

The large increase in ECR ion source performance in the last two decades has been realized on the basis of more or less empirically established macroscopic design rules. Further improvements will depend more and more on a better understanding of the underlying plasma physics and ion extraction in ECR ion sources. However, this is a very complicated and challenging problem because of the collective character of plasma behavior and the huge ranges in time and length scales involved.

To illustrate the complexity of ECR ion source behavior we show in Fig. 3.7 measured beam profiles behind the extraction system for two different operating conditions of the ECR ion source differing only in gas pressure and extraction solenoid current. The operating conditions corresponding to Fig. 3.7a are the standard conditions giving a high beam current, good stability and optimum beam transport efficiency. The operating condition for the hollow beam profile (see Fig. 3.7b) results in significantly reduced performance in terms of intensity, stability and transport efficiency.

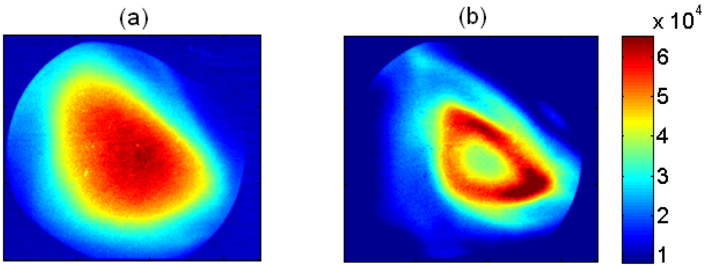

Figure 3.7: *Measured* He^+ *beam profile behind the extraction system for stable operation (a) and an unstable operation (b) in the KVI-AECR ion source.*

Many groups have developed numerical modeling and simulation tools for ECR ion sources, but detailed three-dimensional, self-consistent simulation codes treating both the electron and ion dynamics in ECR plasmas are still lacking. Also at KVI an ECR ion source simulation code has been developed which has been used in this thesis to determine the phase-space distributions of ions in the plane of the plasma electrode. These distributions are used as initial conditions for ion extraction and transport calculations described in chapters five, six and eight. Before describing the KVI plasma simulation code a brief overview will be given of the simulation efforts done by other groups.

An initial effort of ECR ion source plasma simulation was done by the Grenoble group [104–107]. They have developed a zero-dimensional code that simulates the electron and ion dynamics in a self-consistent manner by solving the Fokker-Planck equation in velocity space. With this code they could qualitatively reproduce several phenomena observed in real ECR ion sources, including the biased-disk, gas mixing and afterglow effects. A detailed quantitative description is of course not possible because no spatial degrees of freedom have been taken into account.

The GEM2D code (General ECR ion source Model) [108–110] under development at FARTECH, Inc, aims at predicting the steady state ECR ion source plasma self-consistently. The advantage of the code is that the electron density, temperature and ion density in the ECR ion source and the CSD of the ion beam extracted from the ECR ion source are calculated by using operational parameters, such as RF power, RF frequency, gas pressure and device configurations as input. However, the code assumes rotational symmetry so that the real 3D magnetic geometry is not taken into account.

The ECR ion source group at LNS, Catania is working on the development of a numerical code to model the electron and ion dynamics in an ECR ion ion source using a Monte Carlo approach [75, 111, 112]. The objective of the simulation is to understand the effect of frequency tuning and two frequency heating on ion dynamics, beam formation and beam brightness, etc. However, the code is not yet predicting the electron/ion dynamics in the ECR source in a self-consistent way [113].

The KOBRA3D-INP [114] code has been developed at INP, Germany by P. Spädtke to model ion sources and space-charge effects during beam extraction and transport. In this code collisions are neglected so that the production and diffusion of multiply charged ions are not calculated. The main assumption is that the ions are magnetized in the whole plasma chamber and that the motion of the charged particles is determined by the magnetic field only [115–117]. The code does not calculate the charge state distribution of the extracted ions, instead the experimentally observed distribution has to be used as input to the code. The code calculates the spatial distribution of the extracted ions by tracing them from their starting positions at the plasma chamber wall along the magnetic field lines that pass through the extraction aperture. The simulation of ion beam extraction from the ECR ion source can be performed with the same code by using the calculated 3D spatial distribution. The major limitation of the code is that it does not simulate the production of multiply charged ions in the ECR ion source, because collisions and diffusion are not taken into account.

Mironov et al. have written a code based on the Particle-In-Cell Monte-Carlo Collision (PIC-MCC) method to model the ion dynamics in an ECR ion source plasma [33, 118]. This code simulates the full 3D ion dynamics in an ECR ion source and has been used to study charge state distributions, ion confinement times, ion temperatures, gas mixing effect and the isotope anomaly, as well as the wall coating effect. The main approximation made in the code is that the electron energy distribution is given by a single Maxwellian with the electron density determined by local charge neutrality and the electron temperature (T_e) is used as a fitting parameter. This implies that the simulations assume a steady-state plasma with a single isotropic electron momentum distribution throughout the plasma and without any internal electric fields. Both ion-ion and electron-ion collisions are taken into account, i.e. electron-ion heating, ion-ion temperature equilibration, ion diffusion and the ionization dynamics are all included in the plasma model. Charge-exchange and recombination processes are neglected because of their low probability in the simulated plasma conditions.

The movement of ions with different masses and charge states is tracked in the three-dimensional min-B field magnetic trap of the ECR ion source using a leapfrog particle mover [119]. The motion of neutral particles is modeled by taking into account scattering and energy losses when they hit the chamber walls. Collisions between charged particles are computed using the model of Nanbu [120]. The collision partners are chosen randomly inside a computational cell using the method of Takizuka-Abe [121].

Simulations are started with equal numbers of neutrals and singly-charged particles uniformly distributed over the source volume. This ensemble of particles is then allowed to evolve until a stationary condition is reached. The total number of particles in the simulation is kept constant by injecting a neutral particle (with room temperature energy distribution) into the plasma chamber for each heavy particle lost through the extraction aperture. Approximately 50 % of the heavy particles remain neutral in the stationary state and the local plasma density is determined dynamically by the balance between the ionization rate and the in-and out-flow of the ions in each mesh cell. In the stationary state, the extracted ion currents can be calculated from the flux of ions through the extraction aperture. More details are given in Ref. [33]. Results of simulated charge state and phase-space distributions are reported in chapter 5 and 6.

Despite the fact that the electron dynamics is not taken into account and that the electron distribution is a simple Maxwellian, it has been demonstrated that this code yields very relevant results for the ion dynamics and the production of highly-charged ions [33]. We have used the code to calculate the charge state distributions and 6D phase-space distributions to perform the three-dimensional simulations of multiply charged ion beam extraction and transport to the injection system of the AGOR cyclotron installed at KVI.

Chapter 4

ECR ION SOURCE AND LOW ENERGY BEAM TRANSPORT

4.1 Introduction

This chapter presents a detailed description of the KVI-AECR ion source, low energy beam transport (LEBT) system and beam diagnostic devices. These are used in the simulations and measurements described in chapters 5–7. In this chapter the KVI-AECR ion source is described in Sec. 4.2, while the low energy beam transport (LEBT) system is described in Sec. 4.3. Section 4.4 gives a description of the various diagnostic devices used in this study.

4.2 KVI-AECR ion source

The ECR ion source of the AGOR facility at KVI is essentially a copy of the AECR ion sources installed in Berkeley (LBNL) [46], Jyväskylä (JYFL) [48] and Argonne (ANL) [52]. A schematic cross section of the KVI-AECR is shown in figure 4.1.

The ion source has an aluminum plasma chamber with inner diameter of 76.2 *mm* and a length of 320 *mm*. The plasma chamber holds the six NdFeB permanent magnet bars (see Fig. 4.2b) with lengths of 295 *mm* generating the hexapole field, which together with the axial mirror field produced by two solenoids generate the minimum-B configuration. The solenoids have an inner bore diameter of 208 *mm*. The magnetic field configuration is characterized by maximum values of 2.1 T and 1.1 T of the axial field at the injection and extraction planes, respectively, a minimum field of 0.36 T in the center of the plasma chamber and a maximum hexapole field at the radial wall of 0.9 T. The calculated magnetic field along the axis of the source is shown in Fig. 4.3. The field maxima are

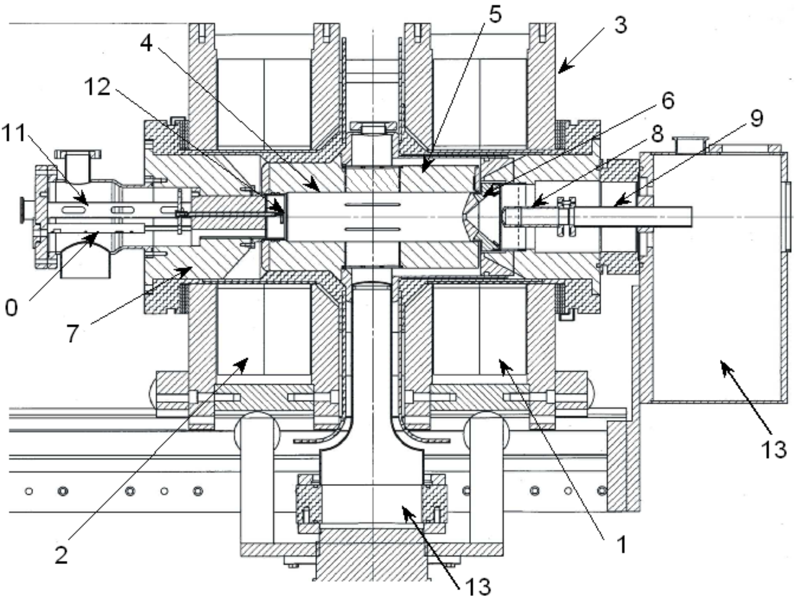

1. Extraction coil
2. Injection coil
3. Iron yoke
4. Aluminum plasma chamber
5. NdFeB Sextupole magnet
6. Aluminum/Iron Extraction electrode
7. Iron plug
8. Puller
9. Grounded electrode
10. Gas feed
11. Microwave feed
12. Biased disk
13. Pumping port

Figure 4.1: *Advanced Electron Cyclotron Resonance Ion source (AECR) at KVI.*

shaped and enhanced by iron yokes around the coils and by iron plugs at the injection and extraction sides of the source. In order to optimize the intensity of the extracted ion beam the field maximum at the extraction side is lower than the field maximum at the injection side.

The plasma chamber is radially accessible through six slits located between the magnet bars of the hexapole magnet. These slits are used to improve the pumping of the plasma chamber by a 410 ls^{-1} turbo pump and also allow insertion of e.g. sputter probes and plasma diagnostics. Fig. 4.4 shows a photo of the injection plug with biased disk, RF wave guide, gas feed and an oven used for metal ion production.

The plasma is heated with 14.1 GHz microwaves generated by a 2 kW klystron amplifier. The microwave power is launched into the plasma chamber from the injection side via a rectangular waveguide connected off-axis to the plasma chamber. In addition to the main 14.1 GHz heating system, the source is also equipped with a 11–12.5 GHz,

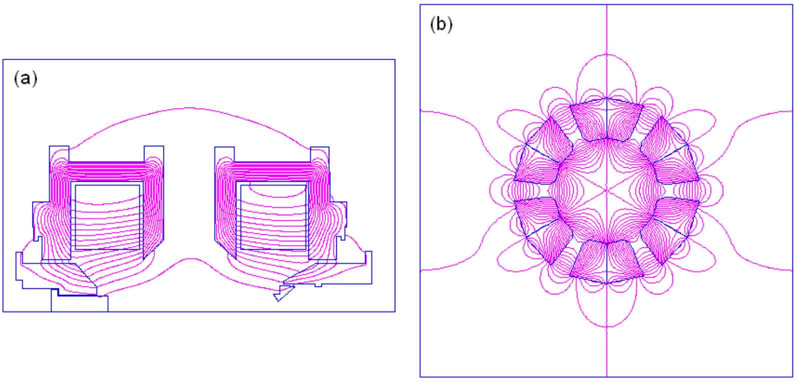

Figure 4.2: *Solenoids (a) and hexapole (b) used in the KVI-AECR ion source.*

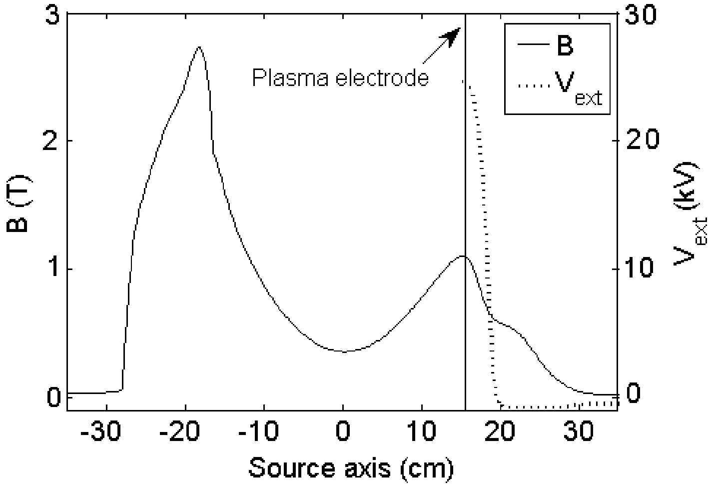

Figure 4.3: *Calculated magnetic field along the axis of the KVI-AECR ion source (left scale) and calculated potential along the axis of the extraction system (right scale).*

400 *W* Travelling Wave Tube Amplifier (TWTA), enabling two-frequency heating. The same wave guide is used for both RF power sources using a special coupler system. The plasma chamber is electrically isolated from ground and biased at the extraction voltage which can have a maximum value of 35 *kV*.

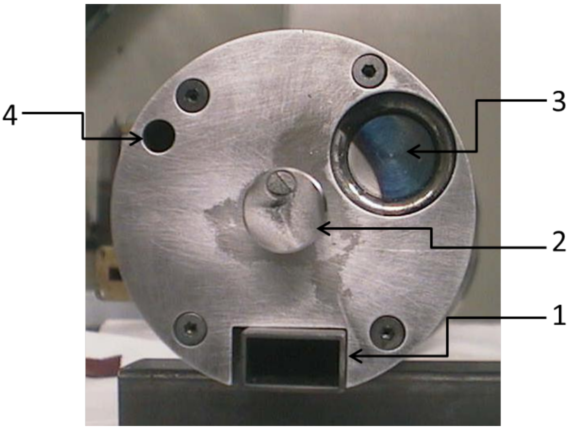

Figure 4.4: *Injection plug: 1. RF wave guide, 2. Biased disk, 3. Oven and 4. Gas feed.*

4.2.1 Extraction system

The ion beam is extracted from the KVI-AECR ion source with an accel-decel extraction system (Fig. 4.5) consisting of three electrodes, i.e. a plasma, puller and ground electrode. The plasma electrode has been designed according to the so-called Pierce geometry [92], with a cone half-angle of 67.5° with respect to the optical axis and is made of aluminum in order to enhance secondary electron emission from its wall. The puller and ground electrodes are made of stainless steel. The diameter of the plasma electrode aperture is 8 *mm*. The beam is extracted by a single puller system with an entrance aperture of 13 *mm* diameter and a length of 95 *mm*. A ground electrode is located behind the puller with an inner diameter of 53 *mm* and a length of 100 *mm*. The puller and ground electrodes have a fixed gap of 5 *mm* and are attached to a translation stage with a range of 20 *mm*. In this way the gap between the plasma and puller electrodes can be varied from 20 to 40 *mm*.

The plasma electrode is electrically connected to the plasma chamber and is therefore biased at the source potential (V_{ext}). The puller electrode has a negative potential (V_{supp}) of a few hundred volts. A typical potential distribution along the axis of the KVI-extraction system ($V_{ext} = 24.7\ kV, V_{supp} = -300\ V$) is shown in Fig. 4.3. The positive potential accelerates ions from the ECR ion source while the negative dip in the potential curve prevents the low-energy secondary electrons produced in the beam transport section downstream to be accelerated into the source thus enhancing the space-charge compensation of the extracted ion beam. The fringe field of the extraction solenoid extends up to the ground electrode as shown in Fig. 4.3.

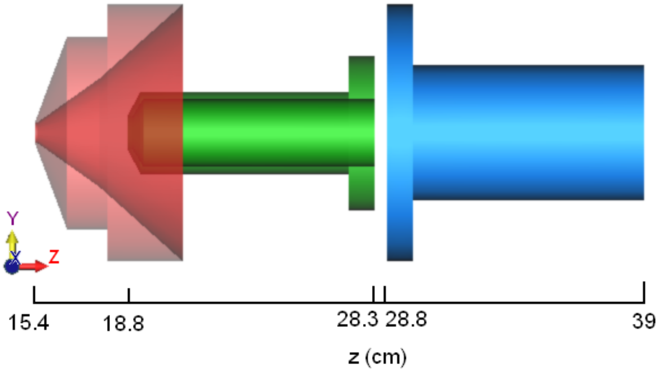

Figure 4.5: *Accel-deccel extraction system used in AECR ion source. The origin of the coordinate system is at the center of the plasma chamber (see Fig. 4.3).*

4.3 KVI-LEBT system

The ion beam extracted from the KVI-AECR is transported to the AGOR cyclotron via the low energy beam transport (LEBT) system shown in Fig. 4.6. It consists of four bending magnets, one magnetic quadrupole triplet, fifteen electric quadrupoles (EQ), several electrostatic deflection plates and diagnostic elements. The properties of the four bending magnets installed in the LEBT system are listed in table 4.1. All electrostatic quadrupoles are identical and have a length of 120 *mm* and aperture of 70 *mm*. Electric quadrupoles are used instead of magnetic ones because the LEBT system was designed to be used for polarized proton and deuteron beams which suffer from depolarization when using magnetic quadrupoles [122, 123].

In order to separate the required charge state the extracted ion beam is transported through a double focusing 110° bending magnet (M110) [124]. The distance from the aperture of the plasma electrode to the effective field boundary (EFB) of this magnet is 682 *mm*. The distance between the image and the EFB is 374 *mm*. This gives a first order magnification of 0.6. In the KVI-LEBT system there is, in contrast to most other systems, no optical element between the ECR ion source and the analyzing magnet. In order to minimize beam losses and aberrations one or more optical elements (solenoid, einzel lens, quadrupole, etc.) are often used to match the emittance of the beam from the ion source to the acceptance of the analyzing magnet. In many laboratories a magnetic solenoid is used directly after the extraction system of the ECR ion source. In particular for high intensity beams containing many different charge states the charge state dependence of the focusing strength of the solenoid can be problematic as it may cause hollow beams due to space-charge effects [125]. An einzel lens (or other electrostatic systems) provides focussing that is independent of the charge state but hinders space-charge compensation, which is most important in this region because of the high intensity of the beam before charge state selection.

The analyzed beam is then transported by a magnetic quadrupole triplet and an electrostatic quadrupole singlet (EQ1) to the 90° bending magnet (M90). The outer two quadrupoles in the quadrupole triplet are identical with a length of 110 *mm* and diameter of 50 *mm*. The length and diameter of the inner quadrupole are 180 *mm* and 50 *mm* respectively. After the M90 magnet the next three electrostatic quadrupoles (EQ2–EQ4) guide the beam to the M50 bending magnet. This magnet bends the beam over 50° after which the beam is transported by the next three electrostatic quadrupoles (EQ5–EQ7) to the M72 bending magnet. This magnet bends the beam over 72° to a 2.1 *m* long drift section after which the beam enters the matching section. After the matching section the beam is bent achromatically over 90° by an electrostatic deflector into the cyclotron injection line, which consists of three solenoids and an electrostatic inflector in the cyclotron center.

The five electrostatic quadrupoles in the matching section are used to match the beam emittance to the acceptance of the AGOR cyclotron. The three solenoids in the axial beamline provide the required orientation of the ion beam at the inflector entrance. Also the strongly increasing field along the cyclotron axis (stray field of the cyclotron) is an essential ingredient of the optics. The matching section and the solenoids are tuned to obtain maximum possible injection efficiency. The KVI-LEBT system also includes various electrric/magnetic beam-steering elements to provide adjustments of both offset and tilt angle of the ion beam. More details can be found in Ref. [123].

Table 4.1: *The properties of the bending magnets installed at the KVI-LEBT*

	M110	M90	M50	M72
Bending radius ρ_0 (mm)	400	240	290	240
Bending angle α (degree)	110	90	50	72
Vertical gap (mm)	67	60	60	60
Entrance pole face angle ε_1 (degree)	37	0	15.63	30
Exit pole face angle ε_2 (degree)	37	0	15.63	30

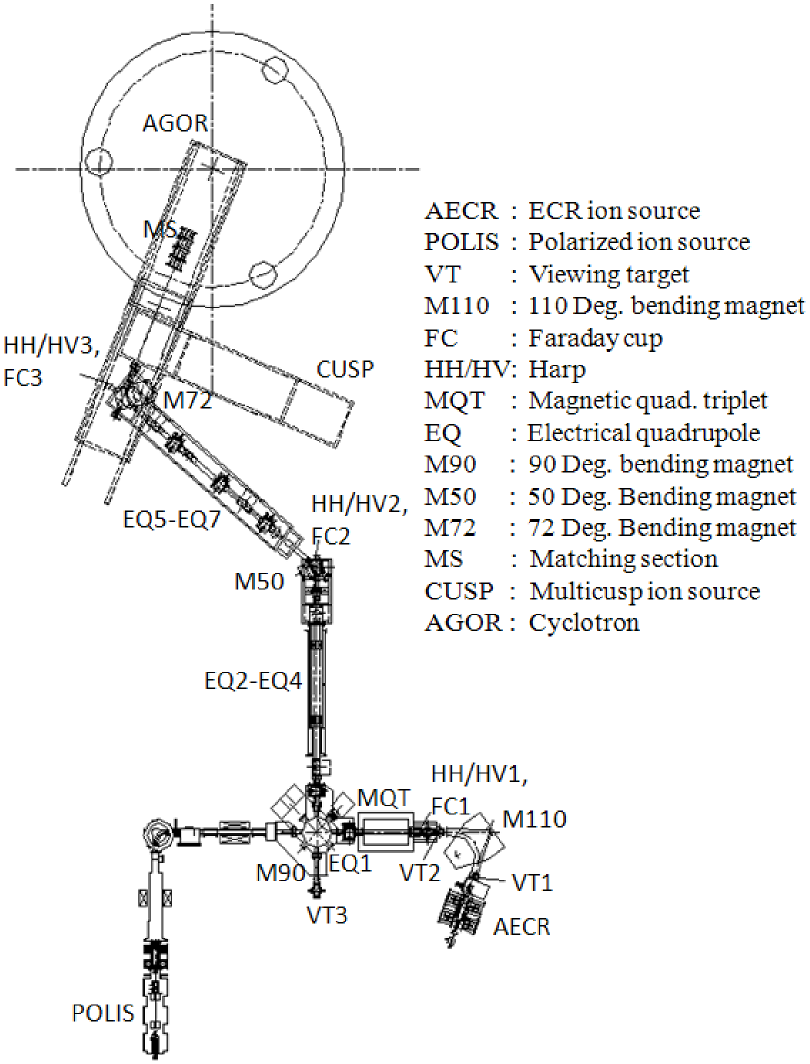

Figure 4.6: *KVI-Low energy beam transport section.*

4.4 Beam diagnostic tools

The efficiency of the ion beam transport through the LEBT system depends on many parameters. In order to measure these parameters and optimize the ion beam transport various beam diagnostic devices are installed in the KVI-LEBT system: Faraday cups, beam profile monitors and a pepper-pot emittance meter. We have also used these devices to benchmark our beam transport simulations. In this section the various beam diagnostic devices will be briefly discussed and their use explained.

4.4.1 Faraday cup

Beam current is an important optimization parameter for the ion source and beam transport system. Faraday cups (FCs) are the most commonly used devices for beam current measurements [126]. There are several FCs installed in the KVI-LEBT system, their locations are marked in Fig. 4.6. All FC's are equipped with electron suppressor rings which are negatively biased to prevent electrons from escaping [127, 128].

4.4.2 Beam profile monitor

1D and/or 2D transverse intensity distributions are measured with harps ($2 \times 1D$ distribution) and viewing targets (2D distribution). A general review of these kind of beam diagnostics can be found in Ref. [129]. Here we briefly describe the wire harps and viewing targets installed in the KVI-LEBT system.

The wire harp consists of a set of 24 tungsten wires with a diameter of 20 μ m fixed on an insulating ceramic frame in two planes (horizontal (x) and vertical (y)) [128]. The harps are equipped with an electron suppressor ring to minimize the effects of secondary electrons. The current on the individual wires is digitally averaged over 400 ms and used to reconstruct the beam profile. The locations of the harps are marked in figure 4.6.

A viewing target is a simple method to determine the full 2D beam profile. We have used a BaF_3 coated metal disk as a viewing target. The metal disk is a 4 mm thick aluminum plate with a diameter of 70 mm. Three viewing targets have been used to measure the beam profiles, one (VT1) is located behind the extraction system, the second one (VT2) close to the image plane of the analyzing magnet and the third one (VT3) behind the M90 bending magnet (see Fig. 4.6).

The scintillator light from the screen is observed with a monochrome CCD camera. The recorded images are then analyzed off-line using image processing tools. The advantage of a viewing target is that it gives immediate qualitative information about the intensity, size and shape of the incident beam (see Figs. 5.10). The main disadvantage of this method is that it is very difficult to correlate the recorded images to the beam intensity because of the rapid deterioration of the scintillating material by low energy heavy ion beams [14]. Therefore, it is very important to minimize the exposure time and to

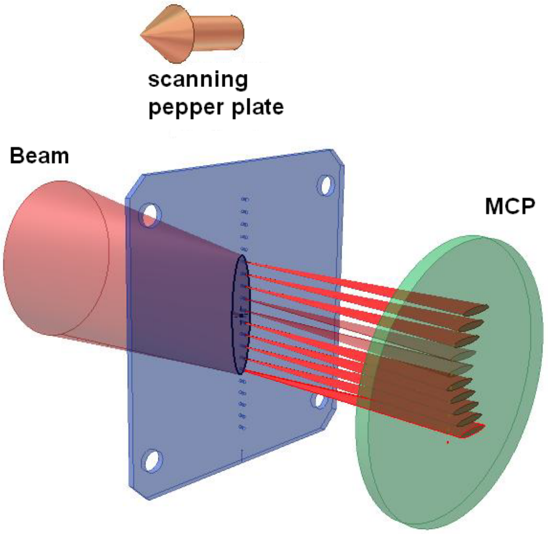

Figure 4.7: *Schematic view of pepperpot emittance meter.*

replace the viewing target frequently. Furthermore, due to the fabrication technique the surface of the viewing target is not perfectly homogeneous, possibly leading to variations in light yield over the surface. Because of these issues we have used the viewing screens only for qualitative measurements.

4.4.3 Peppeprot Emittance meter

The concept of beam emittance has been discussed in sections 2.2.2 and 3.3.4. Measurement of the transverse emittance is important for the evaluation of the performance of the ion source and associated beam transport system. Here we describe an instrument [130] that has been developed at KVI to measure the full four-dimensional (4D) transverse phase-space density distribution.

In order to measure the emittance we have to determine the trajectories of the beam particles. Several methods of measuring the transverse emittance such as the Allison scanner, slit scanner, quadrupole method and pepper-pot method, etc. have been described in the literature [131–138]. The widely used Allison type emittance scanner measures the 2D phase-space distribution in either the horizontal or vertical plane. This device is thus not able to measure correlations between the transverse emittance planes, i.e. it measures a 2D projection of the full 4D phase-space distribution. It is therefore not suitable to measure the emittance of beams from ECR sources, which exhibit correlations between the two transverse emittance planes. A good understanding of the beam prop-

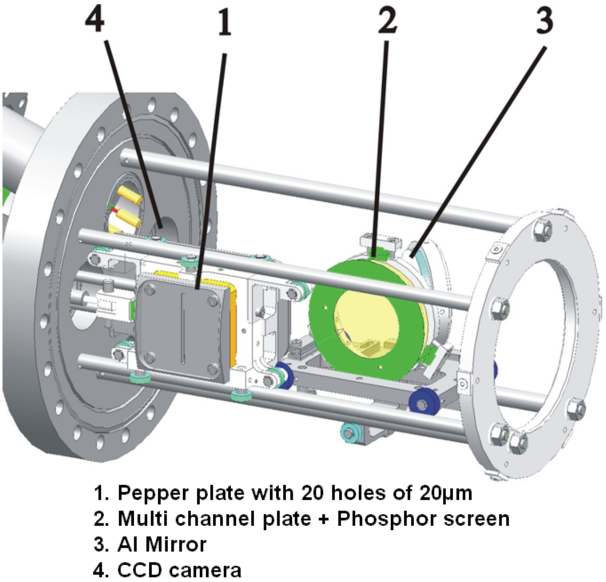

Figure 4.8: *The KVI-4D pepperpot emittance meter.*

erties requires the measurement of the full 4D phase-space distribution. The pepperpot technique that we have adopted does measure the full 4D phase-space distribution and thereby allows a complete analysis of the properties and transport of the beam.

The operation of a pepperpot emittance meter is schematically indicated in Fig. 4.7, which also shows the main components. A 3D view of the KVI device is displayed in Fig. 4.8

The pepperpot plate is a 25 μm tantalum foil with a vertical row of 20 holes with a diameter of 20 μm and a pitch of 2 mm. This pepperpot plate is mounted on a water-cooled copper block that can absorb 150 W of beam power. The assembly can be moved through the beam by a stepper motor driven translation mechanism with a positioning accuracy better than 10 μm. The instrument can be easily adapted to a different phase-space distribution by replacing the pepper plate with one having a suitable hole pattern.

The ions that are transmitted through the holes in the pepperpot plate are detected with a position-sensitive detector positioned 51.3 mm downstream of the pepperpot plate. The detector consists of two micro-channel plates in chevron configuration and a phosphor screen, both with an effective diameter of 41.5 mm. The light emitted by the phosphor screen is imaged by a mirror and a lens system onto a CCD camera mounted outside the vacuum. The MCP, phosphor screen and mirror assembly are mounted on a carriage which can be moved in and out of the beam pneumatically. The measurement is performed by scanning a 1D vertical row of holes in the horizontal direction. This method

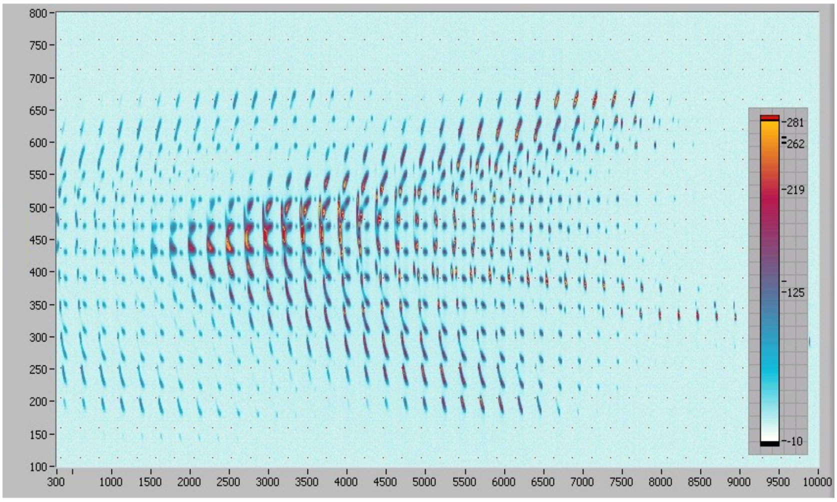

Figure 4.9: *A typical hyper emittance measured by pepperpot emittance at the image plane of the analyzing magnet.*

was chosen because the large horizontal divergence of the beam at the measurement location would compromise the resolution in the x-direction if a 2D array would have been used. The full four-dimensional phase-space distribution $\rho(x,\ x',\ y,\ y')$ of the ion beam can be reconstructed by stepping the pepper plate through the beam in the x-direction and taking a CCD image at each step. An entire series of these images measured with the pepperpot emittance meter at the image plane of the analyzing magnet in the KVI-LEBT is shown in Fig. 4.9. More detailed information about the KVI-4D pepper-pot emittance meter is presented in Ref. [130, 139].

Two dimensional projections can be constructed from the measured full 4D phase-space density distribution $\rho(x,\ x',\ y,\ y')$ by integrating over the other two variables, e.g. the standard (x,x') distribution is calculated as

$$\rho(x,x') = \int_y \int_{y'} \rho(x,x',y,y')dydy' \tag{4.1}$$

Once the second-order moments are calculated from the 2D phase-space distributions as defined in equation 4.1 the *effective emittance* can be calculated using equation 2.10:

$$\varepsilon_{xx} = 4\sqrt{\overline{x^2}\cdot\overline{x'^2} - \overline{xx'}^2} \tag{4.2}$$

More detailed information about the pepper pot emittance meter data analysis is presented in Ref. [133, 136–138, 140, 141].

Chapter 5

EXTRACTION AND TRANSPORT OF He$^+$

5.1 Introduction

In order to achieve high quality beam transport from the ECR ion source into the cyclotron it is important to have detailed information on the initial phase-space distribution of the ion beam extracted from the source and to prevent growth of the effective emittance by space-charge forces and aberrations of the optical elements in the beamline. As a first step a detailed 3D simulation of the extraction and transport of an essentially monocomponent Helium ion (He^+) beam has been done and compared with measurements to assess its validity. The simulation consists of two parts. First an initial phase-space distribution is calculated at the plasma electrode aperture of the ECR ion source using our plasma simulation code (PIC-MCC) [33]. In the next step the He^+ ions are tracked through the extraction system (an accel-decel lens), drift spaces and the 110° analyzing magnet (a double-focusing magnet). These elements form the first part of the beam transport system and are shown in Fig. 4.6. Both the space-charges of the ion beam and the magnetic fringe fields of the ECR ion source and analyzing magnet are fully taken into account. The effect of the space-charge forces is studied by varying the beam intensity in the simulations. Beam profiles and transverse emittances have been calculated and compared with measurements at various positions along the beamline.

This chapter is organized as follows: In Sec. 5.2 the He^+ formation is described, while the simulation of ion extraction and transport is discussed in Sec 5.3 and Sec. 5.4, respectively. In Sec. 5.5 the results of the calculations are compared with measurements of the beam profiles and emittances at two different locations, i.e. directly after the extraction system and close to the imaging plane behind the analyzing magnet (Fig. 4.6).

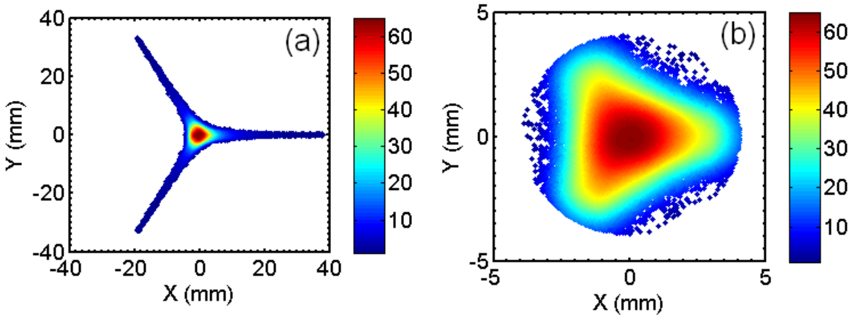

Figure 5.1: *Calculated spatial distribution of* He^+ *at the plasma electrode (a) and through the aperture of the plasma electrode (b).*

5.2 Beam formation of He$^+$

The PIC-MCC Code simulates the ion dynamics in the ECR ion source plasma using the particle-in-cell method. The full 3D min-B magnetic field is used. Ionization, recombination and all other scattering processes are taken into account in the code. Here only a brief summary of this simulation is given, more details can be found in Ref. [33].

The simulation is started with an equal number of He atoms (10^5) and singly charged He^+ ions which are homogeneously distributed in the ECR ion source volume. The electron energy distribution is given by a single Maxwellian with the electron density determined by local charge neutrality. No electron dynamics is considered, the electron temperature is treated as a free parameter. The gas pressure in the chamber is defined by the particle statistical weight and by the total number of neutral particles in the chamber in the stationary situation. The electron temperature is tuned to fit the experimental charge state distribution (CSD) of the extracted He^{q+} beam, and is around 250 eV.

The beam formation is determined by the ion motion in the plasma sheath that separates the plasma from the plasma electrode. Ions drifting towards the extraction hole are accelerated in the electric field of the plasma sheath to an energy equal to the plasma potential (typically a few tens of eV). The PIC-MCC code does not model the plasma sheath. In our extraction simulations using the GPT code a planar sheath with a thickness of 15 Debye lengths (≈ 1 mm) is assumed between the plasma electrode and the ECR plasma [142]. Based on measurements [78] we assume a potential difference of 20 V across the plasma sheath.

The calculated spatial distribution of the He^+ ions at the location of the plasma electrode is shown in Fig. 5.1a. A more detailed spatial distribution of the He^+ ions over the aperture in the plasma electrode is shown in Fig. 5.1b. It clearly exhibits the triangular symmetry of the min-B field configuration of the ECR ion source. The calculated dis-

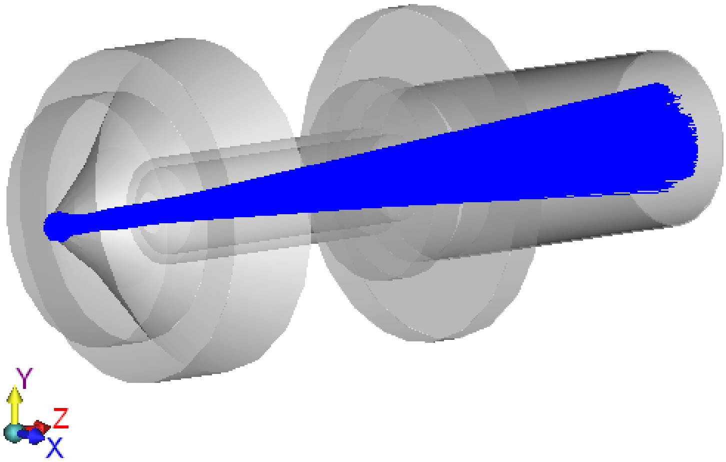

Figure 5.2: *He^{+} beam trajectory through the extraction system.*

tribution nicely coincides with the sputter marks observed on the plasma electrode (see Fig. 3.5b). The calculated phase-space distribution of He^{+} ions at the plasma electrode is the input for the simulation of ion beam extraction from the KVI-AECR ion source, which is described in the next section.

5.3 Ion beam extraction (He^{+})

We have already discussed in Sec. 2.3 that space-charge forces can have an important effect on the transport of a low-energy ion beam. However, the repulsive space-charge in a real ion beam is always to certain degree compensated by (secondary) electrons that are produced in collisions between beam ions and the residual background gas and/or by ion-wall interactions and are then trapped in the positive potential well of the beam. As discussed in Sec. 3.3.4 we will investigate the effect of space-charge compensation of the He^{+} beam without explicitly taking into account the secondary electrons by calculating the ion trajectories for various beam intensities. We start by looking at a zero current beam, in which the particles move independently. This case corresponds to a complete space-charge compensation. We then look into a partly-compensated ion beam to study beam extraction including space-charge forces for various beam intensities, which implies that the space-charge compensation does not depend on the phase-space coordinates.

The ion beam extraction and transport simulations discussed in this chapter have been performed with the GPT code [37], which allows for 3D particle tracking in arbitrary

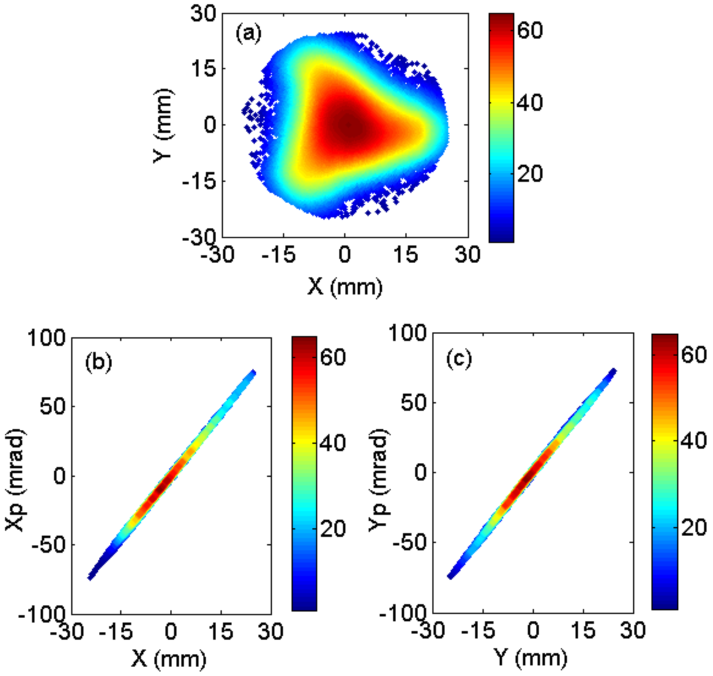

Figure 5.3: *Calculated spatial distribution for a fully space-charge compensated He^+ beam at location VT1 (a). Calculated horizontal (b) and vertical (c) emittance plot of a fully compensated He^+ beam at the same location VT1.*

electric and magnetic fields including space-charge effects. The space-charge models used in the GPT code have been shortly described in Sec. 2.4. The full 3D magnetic fields of the KVI-AECR ion source (solenoid and hexapole fields) and the electrostatic fields of the accel-decel extraction system have been calculated with the LORENTZ3D code [35] and imported in GPT. In this section we study the extraction of the He^+ ions by calculating their trajectories from plasma electrode to the first viewing target VT1 behind the ground electrode of the extraction system, see Fig. 4.6.

5.3.1 Extraction of a fully-compensated He^+ beam

Fig. 5.2 shows the He^+ ion trajectories through the accel-decel extraction system of the KVI-AECR ion source. The plasma electrode is always biased at $+24$ kV, the puller electrode at -300 V and the ground electrode connected to ground potential. From the simulated ion trajectories we have calculated various two dimensional (2D) cross sections of the four-dimensional (4D) transverse phase-space, e.g. 2D beam profiles and emittance plots, which can be compared to measurements. Fig. 5.3 shows the calculated 2D beam profile and emittances at the location of viewing target VT1 for a space-charge compensated beam. The phase-space distributions of the beam in the horizontal and vertical planes are nicely elliptical and nearly identical; the corresponding effective emittance $\varepsilon = 65\ \pi\ mm\ mrad$. During the ion beam extraction in the fringe field of the extraction solenoid, the ion beam triangle rotates due to the Lorentz force and simultaneously grows in size. The size is determined by the divergence of the extracted beam. To verify that the beam emittance is dominated by the fringe field of the extraction solenoid (see sec. 3.3.4) and hexapole we have performed a simulation of ion beam extraction without the magnetic field in the extraction region. In this case we find that the emittance of the extracted ion beam is negligible ($\approx 2\ \pi\ mm\ mrad$).

In order to study the effect of the hexapole fringe field on the ion beam extraction we have also performed a simulation with only the fringe field of the extraction solenoid, i.e. the fringe field of the hexapole is turned off. The result of this simulation are nearly identical to that of the full simulation. We therefore conclude that the fringe field of the hexapole is not important for the ion beam extraction from our source. In addition to the ECR magnetic field also the extraction potential influences the ion beam extraction, in particular the ion beam rotation and divergence. This has been tested in the simulations by changing the extraction potential and agrees with experimental observations.

5.3.2 Extraction of a partly-compensated He^+ beam

To study space-charge effects we have performed trajectory simulations including space-charge forces for different ion beam intensities of the He^+ beam. These simulations mimic beams with varying degrees of space-charge compensation.

Fig. 5.4 shows calculated 2D beam profiles and the horizontal emittances at the location of viewing target VT1 for an uncompensated beam with various beam currents. The PIC-MCC code predicts the total extractable He^+ current to be 450 μA, which is close to the measured beam current. The He^{2+} contribution is around 10 % of the total beam current and has not been taken into account. In the simulations we have assumed various degree of space-charge compensation $(95\ \%,\ 90\ \%,\ 80\ \%,\ 40\ \%\ and\ 0\ \%)$ by varying the beam current from 5 % to 100 % of the maximum value 450 μA. The 2D beam profiles of the space-charge compensated and uncompensated beams at the location of VT1 differ significantly (see Fig. 5.4). The uncompensated beam develops a hollow core and also the effect of the initial plasma distribution on the beam formation is amplified by the space-charge forces (see hot spots in Fig. 5.4). Figs. 5.4 (a) and (c) and 5.3 show a less pronounced change in the spatial profile between 90 % and 100 % space-charge compensation. Fig. 5.5 shows a nearly linear increase of effective emittance with decreasing space-charge compensation. These simulations clearly show the importance of effective space-charge compensation.

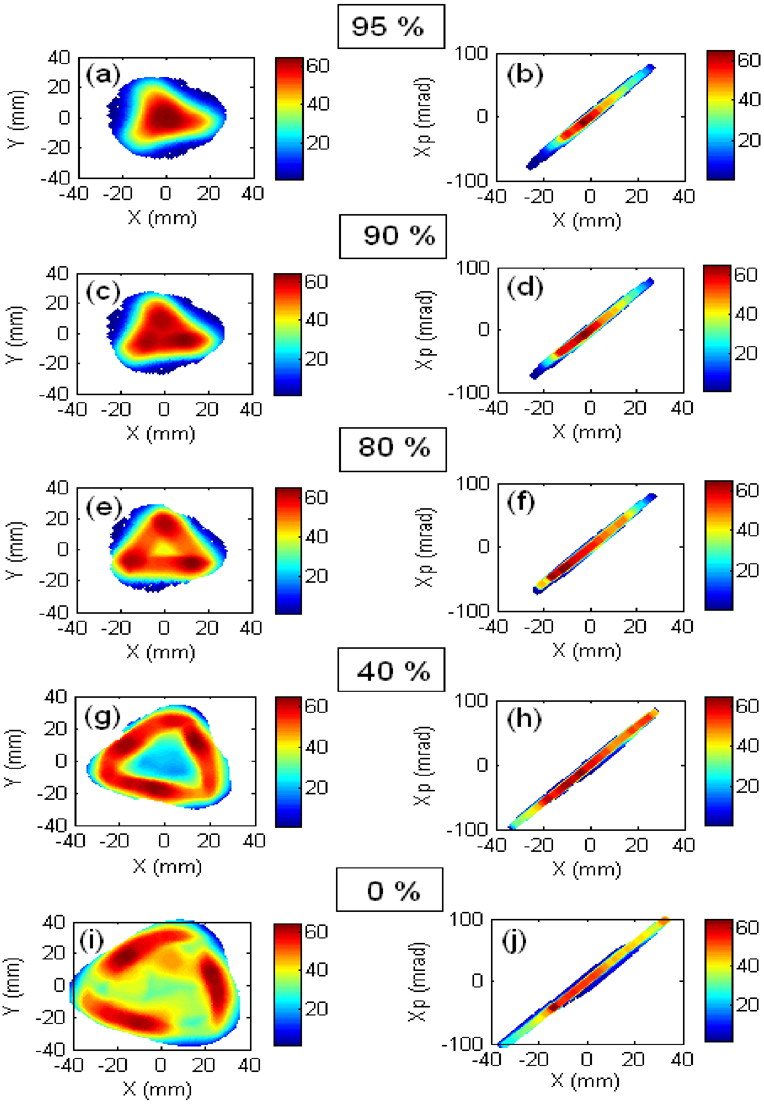

Figure 5.4: *Calculated spatial distributions (left column) and horizontal emittance (right column) of 450 μA He^+ beam with various degrees of space-charge compensation behind the ground electrode at location VT1. The percentage indicates the degree of space-charge compensation assumed in the calculation.*

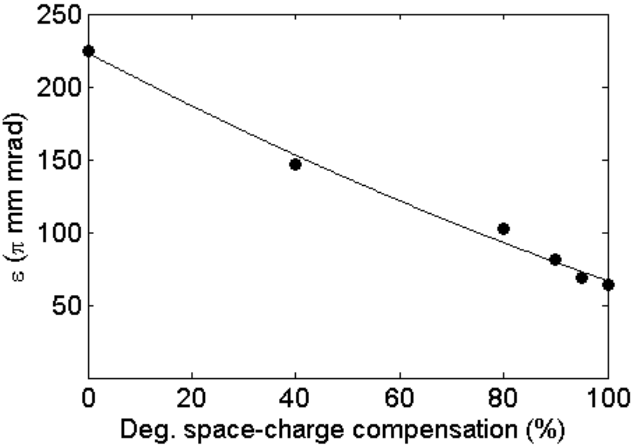

Figure 5.5: *Effective emittance of the He^+ beam for different degree of space-charge compensation for a total extracted of* 450 μA *directly after the extraction system (VT1).*

5.4 Ion beam transport (He^+)

At the beginning of the LEBT system a double-focusing dipole magnet analyses the extracted beam and selects the ions with the required charge-to-mass ratio. The selected component is then transported through a series of bending and focusing elements to the injection system of the AGOR cyclotron. The imperfections in the optical elements as well as the large emittance of the ion beam extracted from the ECR ion source provide a difficult challenge for the design of the LEBT system. In order to study the properties of the system we have simulated the ion beam transport through the LEBT system. In this section we study the beam transport up to the image plane of the analyzing magnet (at the location of VT2) both with and without space-charge compensation. The ion beam transport through the LEBT system up to the matching section is discussed in chapter 6.

5.4.1 Transport of a fully-compensated He^+ beam

In this simulation the full 3D magnetic field of the analyzing magnet calculated with LORENTZ3D is taken into account. The phase-space distribution at the location of VT1 (see Fig. 5.3) is used as the input for the transport simulation.

We have calculated the ion beam trajectories through the analyzing magnet up to the image plane (VT2). From the ion trajectories we extract various two dimensional (2D) cross sections of the four-dimensional (4D) transverse phase-space, i.e. 2D beam profiles and emittance plots, which are compared with measurements. Fig. 5.6 shows the beam profile and emittance at the location of VT2. The triangular spatial distribution

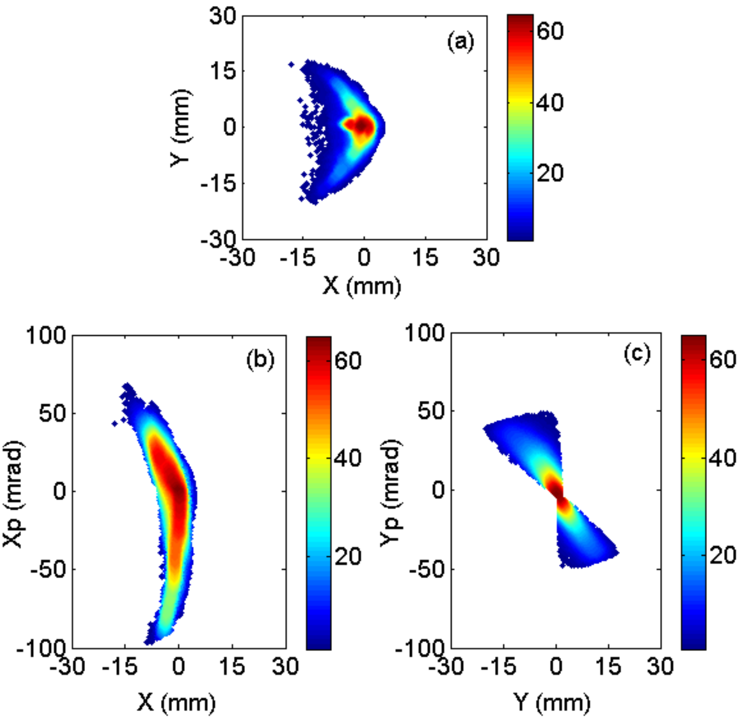

Figure 5.6: *Calculated spatial distributions for a fully space-charge compensated* He^+ *beam in the image plane of the analyzing magnet at location VT2 (a). Calculated horizontal (b) and vertical (c) emittance plot of a fully compensated* He^+ *beam at the same location VT2.*

of the extracted beam at the location of VT1 (see Fig. 5.3) is distorted into a crescent-shaped distribution (see Fig. 5.6a). This is an indication of strong aberrations, in particular second-order, in the analyzing magnet. Because of this the horizontal and vertical emittances are also distorted. Quantitative details are discussed in chapter 7.

The calculated effective emittances of the transported beam in the horizontal and vertical plane are 360 π *mm mrad* and 240 π *mm mrad* respectively. The beam loss during the transport from the location of VT1 to VT2 is around 25 %. It is mainly due to the rather small vertical aperture of the magnet, which explains the smaller effective emittance in the vertical plane.

In order to visualize the correlations at the location of VT2 the phase-space distributions for various combinations of coordinates have been plotted in Fig. 5.7. These distributions clearly show a correlation between the horizontal and vertical phase-space coordinates. The colours indicate particle positions in the horizontal (x) direction at the

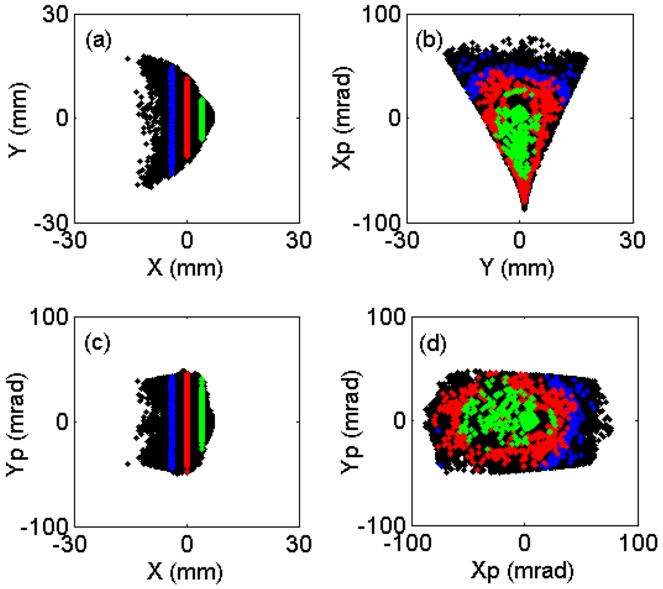

Figure 5.7: *Calculated profiles behind the analyzing magnet (VT2) plotted as a function of* X *with various colours. Spatial profile (a). Mixed phase-space* $(Y\ vs\ Xp)$ *(b) and* $(X\ vs\ Yp)$ *(c). Phase profile* $(Xp\ vs\ Yp)$ *at the same location plotted as a function of* X *with same colours (d).*

location of VT2 as shown in Fig. 5.7a. Comparison of the effective emittances before and after the analyzing magnet clearly shows the deleterious effects of the aberrations of the magnet.

The angle R_p is calculated as,

$$R_p(x) = \left[\frac{1}{N} \sum_{Y=1}^{Y=N} \sqrt{X_p^2 + Y_p^2} \right]_x \tag{5.1}$$

Figs. 5.7 (a) and (d) indicate that a correlation exist between the x-coordinate in the focal plane of the analyzing magnet and the transverse angle R_p, which is proportional to the transverse momentum of the particles. In Fig. 5.8 the average value of the angle R_p is plotted as a function of the x-coordinate of the particles. Since the measured phase-space coordinates are relative values they have been shifted by the right amount to overlap with the simulated points. Both simulated and measured values (with the pepperpot emittance meter) are shown and agree well clearly exhibiting an almost linear correlation.

The simulation results show that the aberrations of the analyzing magnet and the large beam emittance cause a five-fold increase in the effective emittance. Therefore it

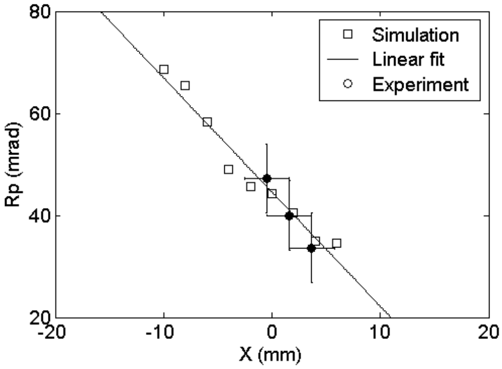

Figure 5.8: *Calculated angle R_p as a function of X in the image plane of the analyzing magnet at location VT2. Simulated (square) and measured (circle) data points.*

is very important to take into account higher-order effects in the design of ion optical systems of large emittance beams. A detailed study of a possible correction scheme for the second-order terms is discussed in chapter 7.

5.4.2 Transport of a partly-compensated He^+ beam

In analogy with the extraction simulation we have also performed a transport simulation of the ion beam from the location of VT1 to VT2 taking into account space-charge forces. We have used the calculated phase-space distribution at the location of VT1 shown in Fig. 5.4 (i) and (j), i.e. the totally uncompensated beam as initial conditions. Fig. 5.9 shows the calculated spatial and phase-space distributions at the location of VT2. The effective emittance of the transported beam increases significantly due to the space-charge force and aberrations of the analyzing magnet. In this simulation the calculated beam loss, mainly due to the small vertical aperture of the magnet, during the transport from the location of VT1 to VT2 amounts to about 60 %. The horizontal and vertical emittances of the transported beam are 1300 π mm $mrad$ and 550 π mm $mrad$, respectively. Such a large increase in emittance is easy to measure, so that comparison with emittance measurements will show us how effective space-charge compensation really is.

5.5 Measurements

To validate the simulations discussed in the previous sections we have performed beam profile and emittance measurements. The beam profiles have been measured with viewing screens behind the extraction system at position VT1 and close to the image plane of

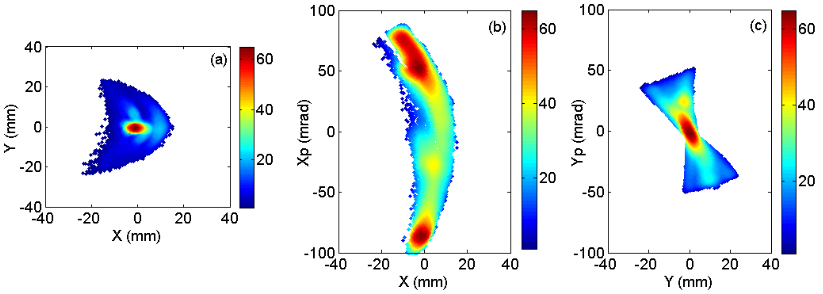

Figure 5.9: *Calculated spatial distributions of an uncompensated* He^{+} *beam with a beam current of* 450 μA *in the image plane of the analyzing magnet at location VT2 (a). Calculated horizontal (b) and vertical (c) emittance plot of an uncompensated* He^{+} *beam with a beam current of* 450 μA *at the same location VT2.*

the analyzing magnet at position VT2. Furthermore the full 4D emittance has been measured with a pepper-pot emittance meter at location VT2 behind the analyzing magnet. The ECR ion source was tuned in such a way that the extracted ion beam was mainly He^{+} ($\approx$ 500 μA) with a minor He^{2+} component ($\approx$ 65 μA). The beam profile measurement system and the pepperpot emittance meter have been discussed in Sec. 4.4.

5.5.1 Beam profile

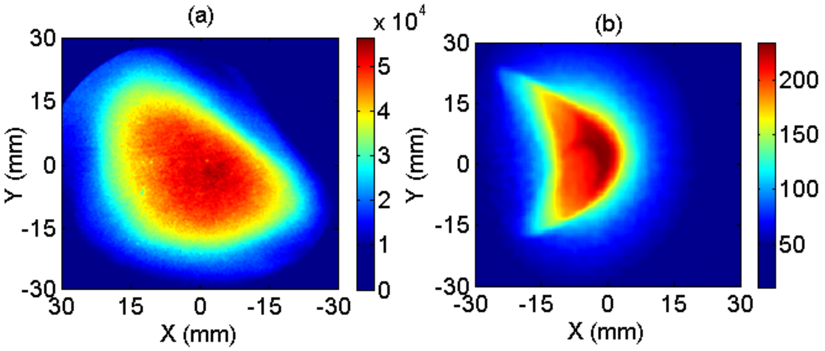

Figure 5.10: *Measured beam profiles of a* 24 *kV* He^{+} *beam behind the ground electrode at location VT1 (a) and in the image plane of the analyzing magnet at location VT2 (b).*

The measured beam profiles at viewing targets VT1 and VT2 are shown in Fig. 5.10 (a) and (b), respectively. During the measurement the background pressure in the beamline was in the order of 10^{-7} *mbar*. It should be noted that the beam profile measurement

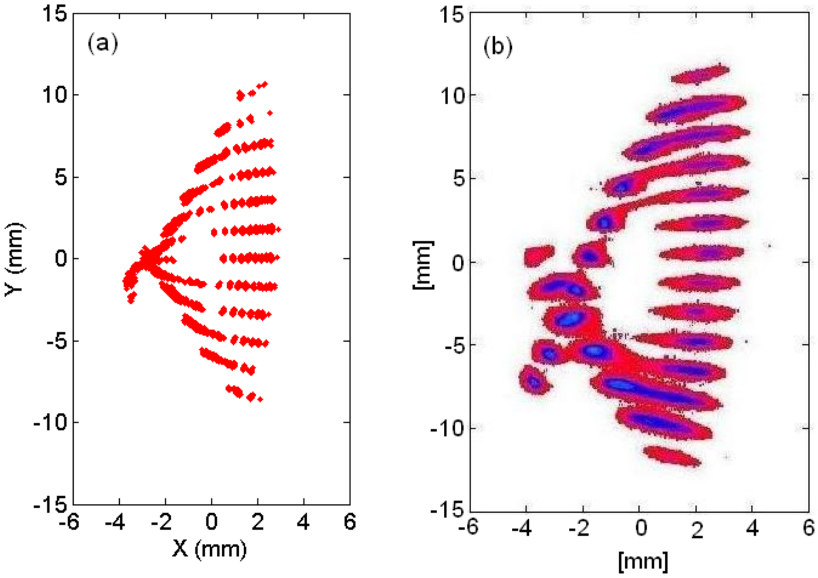

Figure 5.11: *Calculated spatial distributions at the location of MCP in the pepperpot emittance meter behind the analyzing magnet at location VT2 (a). Beam profiles of a 24 kV He$^+$ beam measured by MCP through pepperpot at the location of $x = 0$ m in the image plane of the analyzing magnet at VT2 (b).*

using a BaF_3 viewing target only gives qualitative information about the beam intensity of the incident beam because of saturation of the light yield with increasing current density.

A specific feature of the pattern shown in Fig. 5.1 is that the ion flux into the extraction aperture has a pronounced triangular symmetry. This results in a triangular shape of the extracted ion beams, which is confirmed in Fig. 5.10a. The same beam shape is also measured at other ECR ion sources, e.g., VENUS LEBT at LBNL [143]. Comparing the simulated beam profiles (see Figs. 5.3 and 5.4) with the measured beam profile at the location of VT1 (see Fig. 5.10a) favors the simulation of ion beam extraction with a degree of space-charge compensation $\geqslant$ 95 % (see Figs. 5.3a and 5.4a). The size and shape of the simulated beam profile for the fully space-charge compensated beam is comparable with the measured beam profile at the location of VT1. However, there is a slight difference in the amount of beam rotation between the simulated and measured beams. This may be due to a slight difference between the actual and calculated fringe fields and/or the degree of space-charge compensation.

Similarly, the calculated beam profile at the location of VT2 (see Fig. 5.6a) is comparable with the measured beam profile at the same location (see Fig. 5.10b). The calculated crescent-shaped beam profile also appears in the measurement at the location of VT2.

5.5.2 Emittance

A much more stringent test of the simulations is obtained by comparing them with measurements of the 4D transverse phase-space distribution of the beam. In order to do so we have replaced viewing target VT2 with a pepper-pot emittance meter [139, 144].

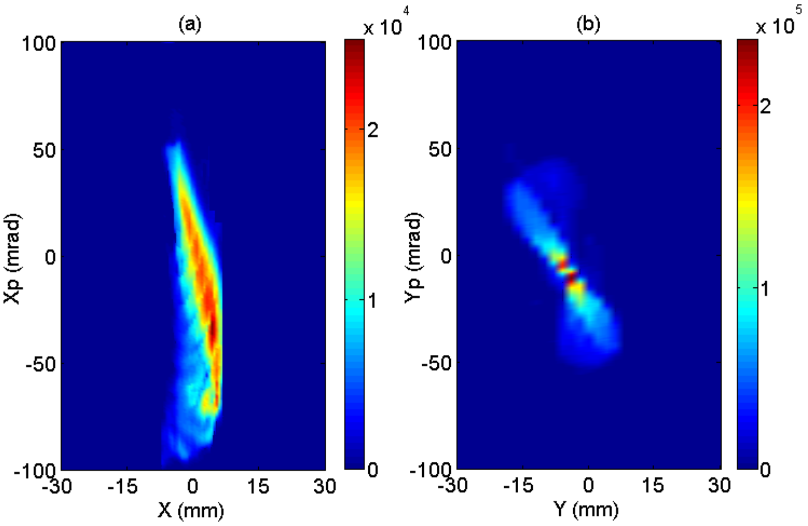

Figure 5.12: *Measured beam emittance of a 24 kV He^+ beam in the image plane of the analyzing magnet at location VT2, horizontal emittance (a) and vertical emittance (b).*

The measurement with the emittance meter was simulated with the calculated phase-space distributions of the transported ion beam at the location of the emittance meter, as displayed in Fig. 5.6. The calculated spatial distribution at the location of the MCP is shown in Fig. 5.11 (a). Fig. 5.11 (b) shows the measured spatial profile for He^+ ions using the pepperpot device with the holes in the pepperpot mask positioned at $x = 0$. The good agreement between the measurements and simulations demonstrates the validity of our full 3D simulations.

Fig. 5.12(a) and (b) show the horizontal and vertical 2D phase-space profiles extracted from the measured 4D phase-space data of the transported ion beam. The measured effective beam emittance in the horizontal plane is 390 π *mm mrad* and in the vertical plane 320 π *mm mrad*. Comparison of the plots in Figs. 5.6 and 5.12, shows similar aberrations in both simulation and experiment. The size and shape of the simulated phase-space distributions are similar to those found experimentally. The good agreement between simulation (see Fig. 5.6) and measurement clearly indicates that our simulations reproduce the basic mechanisms of beam formation, extraction and transport. Also the fringe fields and aberrations of the analyzing magnet seen to be well represented in the simulations.

5.6 Conclusions

We have simulated the extraction of a He$^+$ beam from the KVI-AECR ion source and its transport through the analyzing magnet using the GPT and LORENTZ3D codes. The initial ion distribution was obtained using the PIC-MCC code. The good agreement between calculated beam profiles and emittance plots and measured ones shows that all relevant processes are properly incorporated in the simulations. It implies that this type of detailed simulations are a valuable tool to design optimized beam transport systems for large emittance low energy ion beams. We find that the He$^+$ beam is essentially fully space-charge compensated up to a beam current of at least 0.5 *mA* and that the initial beam emittance is dominated by the conservation of canonical angular momentum.

Chapter 6

EXTRACTION AND TRANSPORT OF A MULTIPLE CHARGE STATE NEON BEAM

6.1 Introduction

In the previous chapter we have described simulations and measurements on an essentially mono-component He^+ beam. The comparison of simulations and measurements for this beam showed the validity of our simulation approach. In this chapter we broaden our simulations to a multi-component neon beam.

In Sec. 6.2 the simulation of multiple charge state neon beam formation at the plasma electrode using the PIC-MCC code [33] is discussed. The simulation of the extraction of this beam including space-charge effects with the GPT code [37] is then described in Sec. 6.3. Finally, in Sec. 6.4 the transport of a Ne^{6+} beam up to the matching section of the AGOR injection system is studied using the GPT and COSY INFINITY [23] codes.

6.2 Beam formation of Ne^{q+}

Just as for the He^+ simulation discussed in chapter 5 we use the PIC-MCC code to determine the phase-space distribution of the Ne^{q+} ions at the aperture of the plasma electrode which is then used as input for the subsequent extraction and transport simulations. In order to simulate a realistic case that can be compared with experiments we have chosen the relevant parameters in the PIC-MCC code such that the ion source is optimized for Ne^{6+} production, i.e. an electron temperature of 1 *keV* and gas pressure

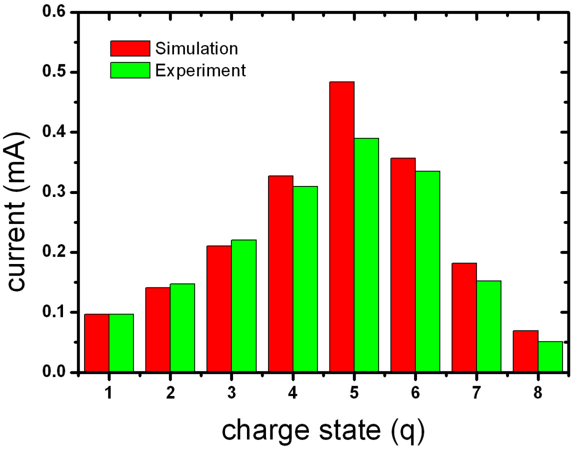

Figure 6.1: *Calculated (red) and measured (green) charge state distributions of neon ions at the location of VT2. In the calculated charge state distribution the simulated beam loss from the plasma electrode to the location of VT2 is taken into account.*

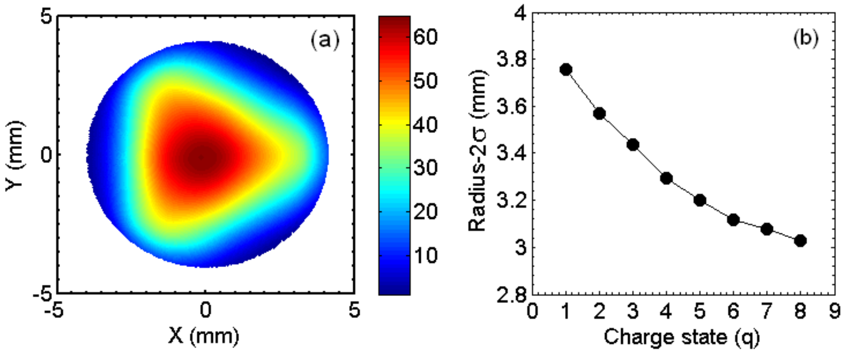

Figure 6.2: *Calculated spatial distribution of* Ne^{+} *ions at the aperture of the plasma (a) and effective beam radius* $(2\ \sigma)$ *for each charge state of the neon ions at the aperture of the plasma electrode (b).*

of 6.8×10^{-7} *mbar*. With these parameters we obtain a charge state distribution at the plasma electrode. In order to compare this charge state distribution with a measured one at the location of VT2 behind the analyzing magnet we have calculated the charge state dependent loss factors for the transport from the plasma electrode to VT2, see Sec. 6.4. Calculated and measured charge state distributions at VT2 are shown in Fig. 6.1 as can be seen, the overall agreement is good. The calculated beam current through the aperture of the plasma electrode is around 2.25 mA.

The spatial distribution of the neon ions integrated over all charge states at the aperture of the plasma electrode is shown in Fig. 6.2a. The triangular shape is caused by the magnetic field configuration of the ECR ion source. Looking into more detail shows that the spatial extent of the distribution depends on the charge state: for higher charge states the spatial distribution becomes progressively smaller. The 2σ radius of the ion distribution as a function of the charge state is shown in Fig. 6.2b. The PIC-MCC code also calculates the ion temperature as a function of the charge state. The mean ion temperature inside the plasma is 0.25 eV, but Ne^{1+} ions have a temperature of only 0.15 eV, while the ion temperature slowly increases with increasing charge state. More details about the influences of the electron density, temperature, ion confinement time and gas pressure are discussed in Ref. [33].

6.3 Ion beam extraction

The simulations of the multiple charge state beam extraction discussed in this chapter have been performed with the GPT code [37] including space-charge effects. The full 3D magnetic fields of the KVI-AECR ion source (solenoid and hexapole fields) and the electrostatic fields of the accel-decel extraction system have been calculated with the LORENTZ3D code [35] and imported in GPT. In this section we study the extraction of the Ne^{q+} ions by calculating their trajectories from the plasma electrode to the first viewing target VT1 behind the ground electrode of the extraction system, see Fig. 4.6. In this simulation a planar sheath with a thickness of 15 Debye lengths (≈ 1 mm) is assumed between the plasma electrode and the ECR plasma [142] and the plasma potential is assumed to be 20 V [78]. The phase-space distributions of the Ne^{q+} ions at the plasma-electrode aperture obtained in Sec. 6.2 provide the initial conditions for the trajectory calculations.

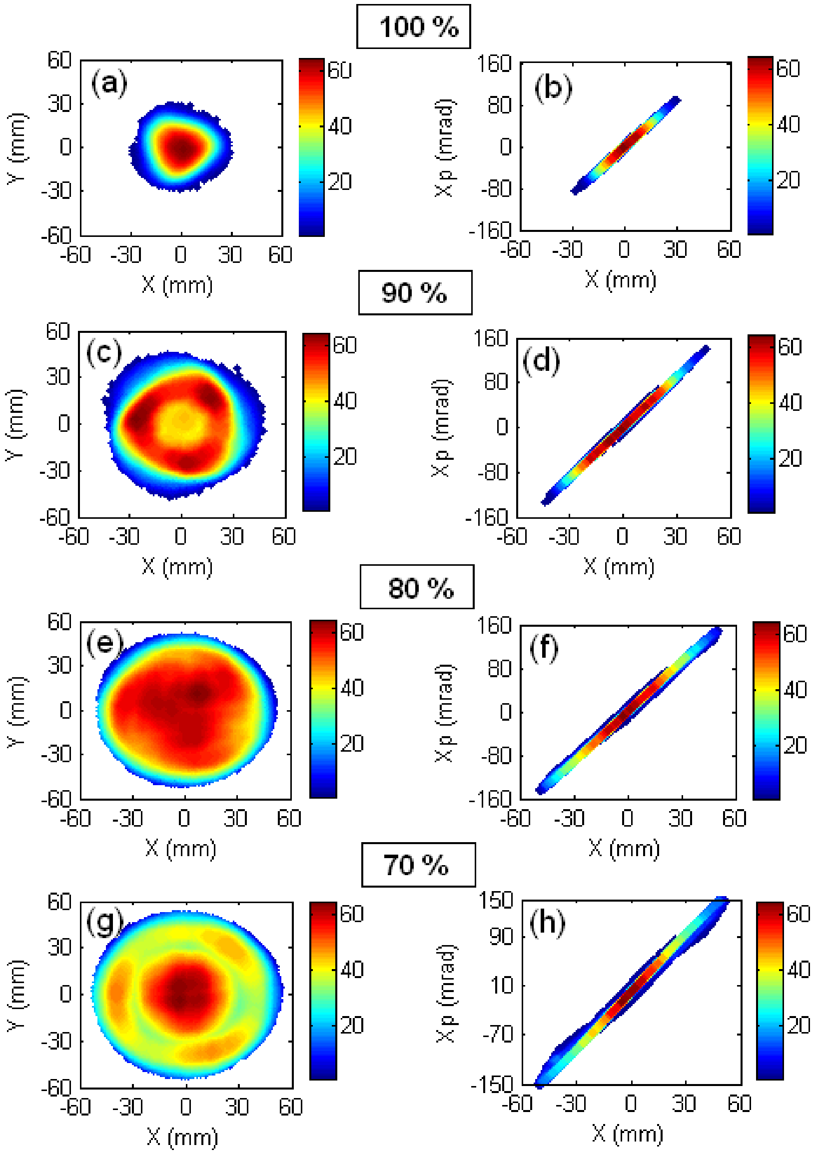

Figure 6.3: *Calculated spatial distributions (left column) and horizontal emittance (right column) of* 2.25 *mA* Ne^{q+} *beam* ($V_{ext} = 24$ *kV*) *with various degrees of space-charge compensation behind the ground electrode at location VT1. The percentage indicates the degree of space-charge compensation assumed in the calculation.*

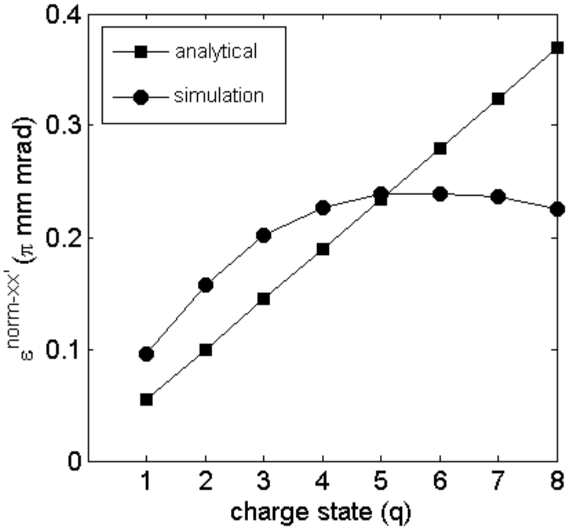

Figure 6.4: *Calculated effective normalized emittance of the neon ions behind the extraction system. Values are calculated with equation 3.10 (square) and using simulation (circle).*

First we study in subsection 6.3.1 the extraction of a fully-compensated Ne^{q+} beam, i.e. the ions are assumed to move independently without interacting with each other. In subsection 6.3.2 we study beam extraction including space-charge forces for various degrees of compensation. In all cases the plasma electrode is biased at $+24\ kV$ and the puller electrode at $-300\ V$.

6.3.1 Extraction of a fully-compensated Ne^{q+} beam

The ion trajectories have been calculated using the calculated 3D magnetic and electric fields of the ECR magnetic system and the extraction electrode system. From the trajectories the 4D phase-space distributions and various 2D projections at any location can be derived.

Fig. 6.3 (a) and (b) show the spatial profile and horizontal emittance of the multiple charge state neon beam at the location of viewing target VT1. The effective emittances of the beam in the horizontal and vertical planes are nearly identical. Values of the effective normalized horizontal emittance as a function of the charge state obtained from the simulation are given in Fig. 6.4. Comparison of the simulation results with those according to eq. (3.10) shows a clear discrepancy. According to Busch's theorem the emittance of a beam formed in a magnetic field is proportional to the square of the initial radius (see Eq. 3.10). Fig. 6.2b shows that the effective radius of the spatial distribution

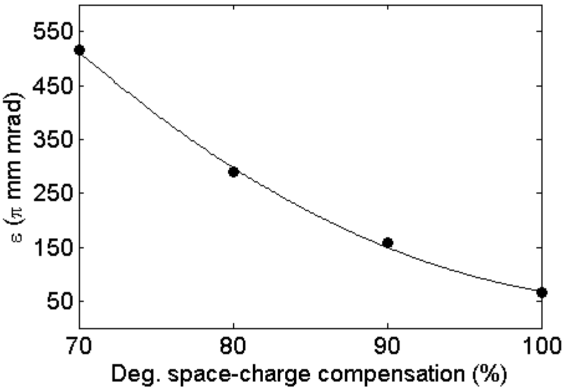

Figure 6.5: *Effective emittance of the neon beam for different degree of space-charge compensation for a total extracted of* 2.25 *mA direct after the extraction system (VT1).*

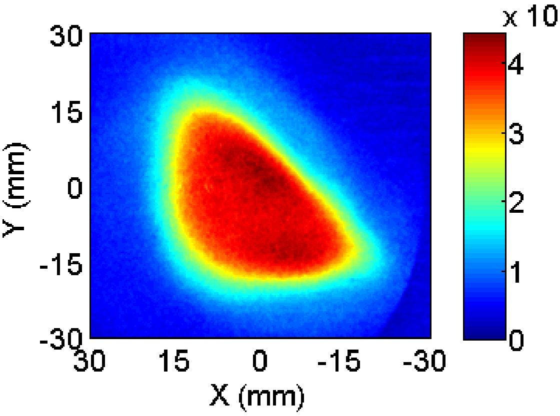

Figure 6.6: *Measured beam profiles of a* 24 *kV multiple charge state neon beam behind the ground electrode at location VT1.*

of ions extracted from an ECR ion source depends on the charge state, with higher charge state ions concentrated more along the axis than lower charge state ions. Therefore, the effective extraction radius is smaller for highly charged ions. This reduces the dominance of the magnetic field emittance $(\propto r^2)$ over the ion temperature emittance $(\propto r)$ for highly charged ions. The simulated emittances agree reasonably well with measurements performed at other ECR ion sources, e.g., VENUS LEBT at LBNL [103, 145].

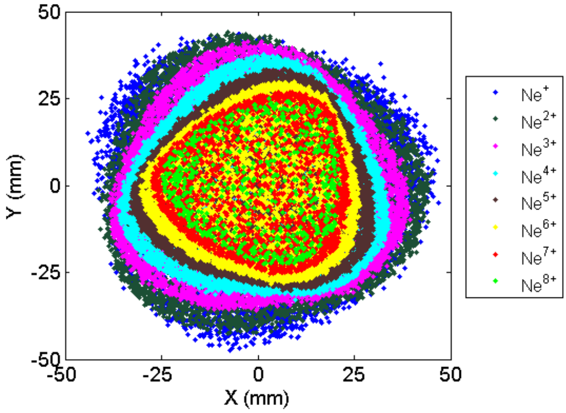

Figure 6.7: *Calculated spatial distribution for a* 90 % *space-charge compensated* Ne^{q+} *beam at location VT1. The various colour indicates the different charge state of the neon beam.*

6.3.2 Extraction of a partly-compensated Ne^{q+} beam

For a fully space-charge compensated beam the nominal current is zero, while for a totally uncompensated beam the nominal current in the simulation would be 2.25 mA. This agrees very well with experimental values. The currents for the individual charge states correspond to their fraction in the beam according to the simulated charge state distribution in Fig. 6.1. The effects of space-charge on the extraction process have been calculated by increasing the nominal beam current in the simulation.

Fig. 6.3 also shows calculated 2D beam profiles and emittances at the location of the viewing target VT1 (behind the extraction system) for varying degrees of space-charge compensation. In this simulation we assume different levels of neutralization (100 %, 90 %, 80 % and 70 %), i.e. the simulation has been performed for beam currents of 0 % to 30 % of total beam current (2.25 mA). The sizes of the 2D beam profiles and consequently the emittances at the location of VT1 depend significantly on the degrees of space-charge compensation. Fig. 6.5 shows a strong increase of effective emittance with decreasing space-charge compensation. These simulations clearly show the importance of effective space-charge compensation in the extraction system.

As a first test of these simulations we have performed a beam profile measurement. The beam profile has been measured with a viewing screen behind the extraction system at position VT1. During the measurement the background pressure in the beamline was of the order of 10^{-7} $mbar$. Fig. 6.6 shows the measured spatial profile of the extracted neon beam. The total extracted current was restricted to 700 μ A in order to prevent damage to the viewing target (sputtering and saturation of the light yield, etc.).

In addition to the emittance increase, effects of the ECR magnetic field on the spatial distribution at the plasma electrode appear to be magnified due to the space-charge forces (see hot spots in Figs. 6.3 (c). e and (g)). During the beam extraction each ion acquires a kinetic-energy determined by the applied extraction potential and the charge state. The fringe field of the extraction solenoid causes a net beam rotation according to the Lorentz force as discussed in Sec. 3.3.4. In order to show the influence of the extraction solenoid of the ECR ion source on the extraction a multiple charge state neon beam the spatial profiles of the different charge states is shown in Fig. 6.7 for a 90 % space-charge compensated beam. The figure shows a noticeable difference in rotation and size of the different charge state extracted from the ECR ion source.

Comparing the simulated beam profiles (see Fig. 6.3) with the measured beam profile at the location of VT1 (see Fig. 6.6) clearly favors the model with space-charge compensation higher than 90 %. The size and shape of the simulated beam profile for the fully space-charge compensated beam (see Fig. 6.3a) is comparable with the measured beam profile.

6.4 Transport of Ne^{6+} beam

To study the properties of the LEBT system we have extended our simulations to a full beam transport through the entire LEBT system. However, because of the large amount of computational time we have only calculated the transport of the multiple charge state beam in 3D up to the location of VT3 behind the 90° bending magnet (see Fig. 4.6). For the transport up to the matching section of the LEBT system a beam envelope calculation with COSY INFINITY was performed.

The phase-space distribution of the fully space-charge compensated beam calculated at the location of VT1 (see Fig. 6.3a) is used as the starting condition for the transport simulation.

6.4.1 Full 3D simulation

The extracted multiple charge state ion beam (Ne^{q+}) from the ECR ion source is transported through the double-focusing analyzing magnet. The magnetic field strength of the analyzing magnet is tuned for transmission of Ne^{6+} ions. The transmitted Ne^{6+} ions are then further transported through the quadrupole triplet, electrostatic quadrupole and 90° bending magnet. From the calculated ion trajectories we then extract various two dimensional (2D) cross sections of the four-dimensional (4D) transverse phase-space, e.g., 2D beam profiles and emittance plots, which will be compared with measurements. In Fig. 6.8 the calculated beam profile and emittances of the Ne^{6+} beam at the location of VT2 are displayed. The plot shows the distorted phase-space distributions of the Ne^{6+} beam. Similar experimental and simulation results have been reported in chapter 5 for the He^{+} beam. As discussed in chapter 5 the ion-optical aberrations and the large emittance

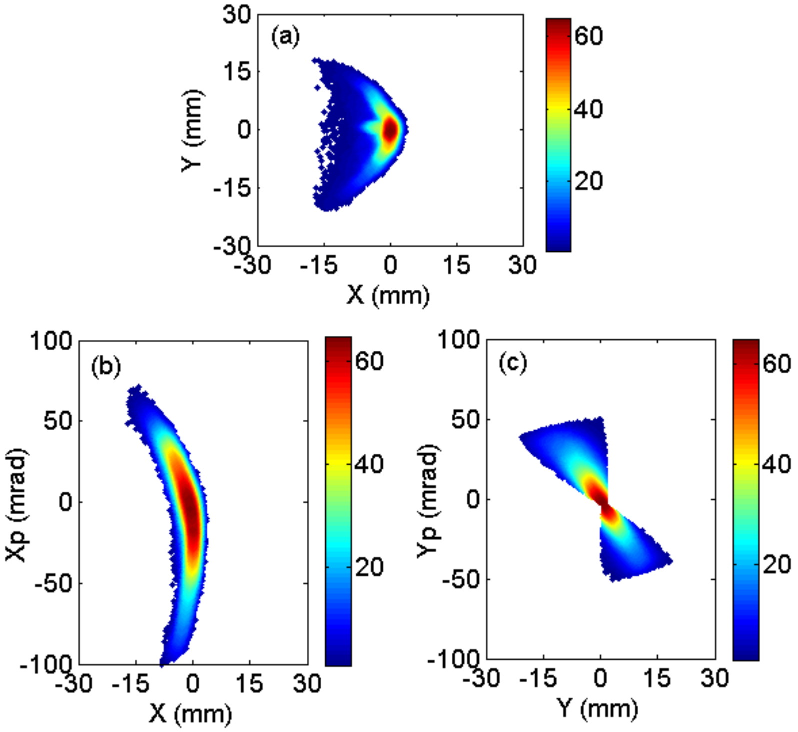

Figure 6.8: *Calculated spatial distributions for a fully space-charge compensated Ne^{6+} beam in the image plane of the analyzing magnet at location VT2 (a). Calculated horizontal (b) and vertical (c) emittance plot of a fully compensated Ne^{6+} beam at the same location VT2.*

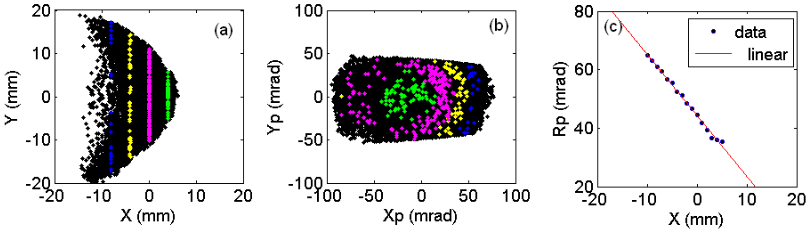

Figure 6.9: *Calculated spatial profile (a) and phase profile $(Xp,\ Yp)$ (b) behind the analyzing magnet at location (VT2). Colours indicate the particle position in the horizontal direction (x) at the location of VT2. Calculated radius R_p as a function of X in the image plane of the analyzing magnet at location VT2 (c).*

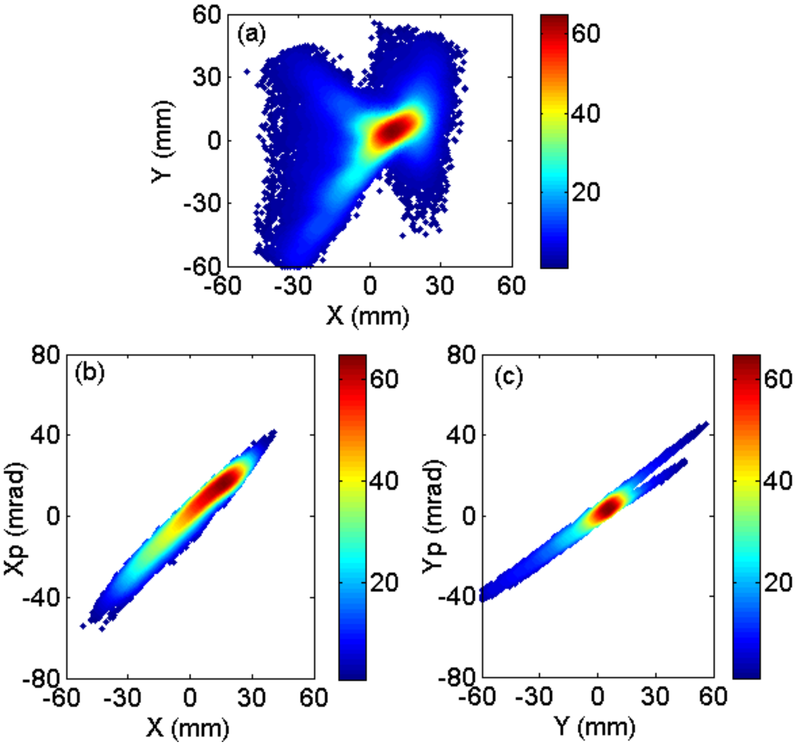

Figure 6.10: *Calculated spatial distributions for a fully space-charge compensated Ne*$^{6+}$ *beam behind the* 90° *bending magnet at location VT3 (a). Calculated horizontal (b) and vertical (c) emittance plot of a fully compensated Ne*$^{6+}$ *beam at the same location VT3.*

of the ion beam extracted from the ECR ion source determine the efficiency of the beam transport. They lead to an increase of the effective emittance both in the horizontal and vertical planes. The calculated effective emittances of the transported beam in the horizontal and vertical plane are 345 π *mm mrad* and 240 π *mm mrad*, respectively, whereas the effective emittance at the location of VT1 is 66 π *mm mrad*. The beam loss during the transport from VT1 to VT2 according to the calculation is approximately 25 %.

Fig. 6.9b shows the phase-phase profile $(Xp\ ,\ Yp)$ at the location of VT2 behind the analyzing magnet. In the plot particles with a specific X-coordinate (see Fig. 6.9a) are indicated with different colours. The calculated angle R_p (see Eq. 5.1) at various x positions is shown in Fig. 6.9c. Fig. 6.9c clearly indicates that particles with larger transverse components are deflected more in the horizontal direction due to their smaller longitudinal momentum.

For the transport of the beam from VT2 to VT3 the settings of the quadrupole triplet and electric quadrupole are taken from typical experimental settings for Ne^{6+} beam trans-

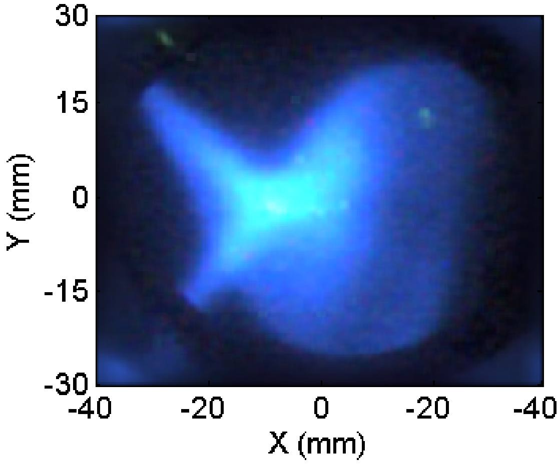

Figure 6.11: *Measured beam profiles of a 24 kV Ne^{6+} beam behind the* 90° *bending magnet at location VT3.*

port. The matching is not perfect with the acceptance of the 90° bending magnet because of the large initial emittance from the ECR ion source and the distorted phase-space distribution after the analyzing magnet. Fig. 6.10 shows the simulated beam profile and emittances of a Ne^{6+} beam at the location of VT3 behind the 90° bending magnet. The calculated effective emittances of the transported beam in the horizontal and vertical planes are 265 π *mm mrad* and 210 π *mm mrad* respectively. During the beam transport the particles that are far from the beam axis are lost explaining the decrease in effective emittance between VT2 and VT3. The calculated beam loss during the transport from the location of VT2 to VT3 is around 20 %. A measured beam profile at the location VT3 is shown in Fig. 6.11. The size and shape of the simulated beam profile of the Ne^{6+} beam is similar to the measured one.

6.4.2 Beam envelope simulation

In addition to the 3D simulations we have also calculated the beam envelope using the code COSY INFINITY [23] up to third-order. The fringe fields of the optical elements are taken into account using built-in models [39]. In order to calculate the beam envelope through the LEBT system we defined an initial emittance of 65 *mm mrad* for the Ne^{6+} beam at the location of the plasma electrode with an energy of 144 *keV*.

The calculated beam envelope plot for the Ne^{6+} beam is shown in Fig. 6.12. In order to estimate the increase in effective emittance through the LEBT system we have calculated the transfer map of the beamline from the location of VT2 to the location of

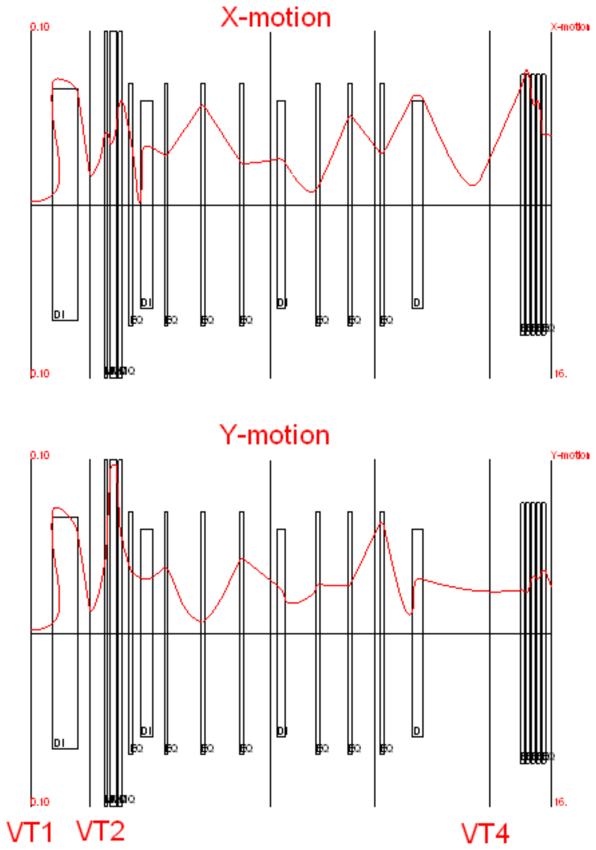

Figure 6.12: *Calculated horizontal (top) and vertical (bottom) beam envelopes for the Ne^{6+} beam using the code COSY INFINITY.*

VT4 behind the M72 magnet (see Fig. 6.12) using the COSY INFINITY code. As discussed in the previous section the full 4D phase-space distribution of the Ne^{6+} beam at the location of VT2 behind the analyzing magnet is known from the 3D simulations. By applying the transfer map calculated with COSY INFINITY to this phase-space distribution we can estimate the effective emittance at the location of VT4. Fig.6.13 shows the effective emittance at the locations of VT1, VT2 and VT4 as a function of the fraction of the beam intensities included in the calculation. Comparison with the acceptance of the AGOR cyclotron, i.e. 140 π *mm mrad*, shows that approximately 40 % of the extracted particles from the AECR ion source falls within this acceptance. Because the two transverse planes are decoupled the overall transmission into the cyclotron will then be in the range $15 - -20$ %. Comparison of COSY INFINITY calculations up to second

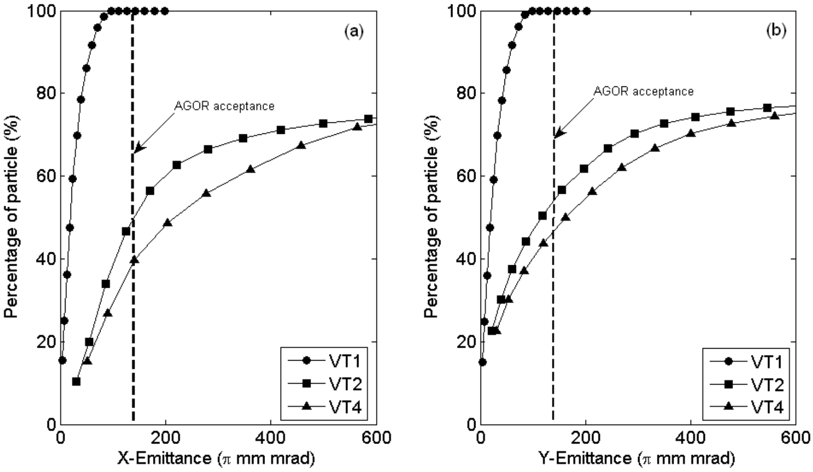

Figure 6.13: *Calculated effective emittance in the horizontal plane (a) and in the vertical plane (b) of the* Ne^{6+} *beam at various locations of the LEBT system. Calculation at location VT1 and VT2 has been performed with GPT. Calculation at location VT4 has been performed with COSY INFINITY. In this plot losses along the beamline has been taken into account from VT1 to VT2 only. At location VT1 the emittance* 140 *pi mm mrad encloses nearly one* 100 % *of extracted particles from the source.*

and third-orders shows little difference, which indicates the dominance of second-order effects as has also been deduced from the full 3D simulations.

6.5 Conclusions

We have simulated the extraction of a multiple charge state neon beam from the KVI-AECR ion source and its transport through the LEBT system using the GPT, LORENTZ3D and COSY INFINITY codes. The initial ion distribution was obtained with the PIC-MCC code. The properties of multiple charge state neon beam formation and extraction has been studied. The good agreement between simulations and measurements clearly indicates that our simulations reproduce the basic mechanisms of multiple charge state ion beam formation, extraction and transport. We find that the Ne^{q+} beam is fully space-charge compensated up to a beam current of at least 0.7 mA and that the initial beam emittance is dominated by the conservation of canonical angular momentum. Our calculation show that the large beam losses observed can be explained by a combination of a large initial emittance of the beam and strong aberrations, particularly in the dipole magnets. There is no need to involve space-charge effects to explain the observed beam losses for the Ne^{6+} beam, which typically has an intensity of 350 μA at the location

VT2, despite the fact that electrostatic quadrupoles are used, which are expected to destroy space-charge compensation. The observed transmission of the Ne^{6+} and similar beams from the ECR source to accelerated beam in the cyclotron, taking into account the cyclotron longitudinal acceptance and the beam losses in the analyzing magnet, is in good agreement with the prediction of the complete simulation.

Chapter 7

OPTIMIZATION OF THE KVI-AECR CHARGE STATE ANALYZER

7.1 Introduction

Measurements show that the low energy beam transport from the ECR ion source to the AGOR cyclotron suffers from significant beam losses, which limit the attainable intensities of the beam extracted from the cyclotron. The simulations described in chapter 5 and 6 show that the 110° analyzing magnet is not only one of the locations of beam losses but also causes a significant increase of the effective emittance due to its aberrations and the large beam dimensions. As the beam essentially fills the full aperture of the magnet the non-linear terms in the equation of motion caused by the higher-order field components have a strong influence on the beam properties [146]. Furthermore, the radius of curvature of the magnet is not very large compared to the beam dimensions, resulting in higher-order kinematics terms and a large contribution of the fringe field to the overall large action of the magnet on the beam [147].

In this chapter we present a study to improve the ion-optical properties of the analyzing magnet and to decrease the beam losses. We have found that this can be achieved by modifying the shape of the pole faces and increasing the magnet gap. First we describe in Sec. 7.2 a detailed study of the ion-optical aberrations of the analyzing magnet based on trajectory simulations and a second-order analysis of the beam transport through the analyzing magnet. Then in Sec. 7.3 a method is described to compensate the ion-optical aberrations of the analyzing magnet by adding hexapole components to its main dipole field. The chapter closes with a summary and outlook in Sec. 7.4.

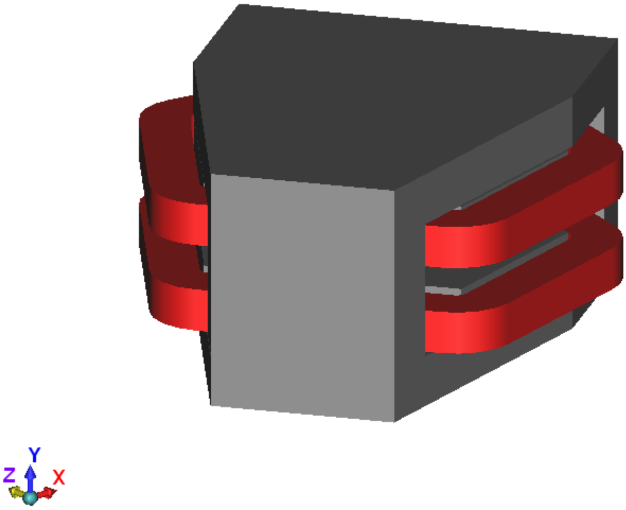

Figure 7.1: *3D view of the KVI-AECR charge state analyzing magnet.*

7.2 Transport properties of the magnet

In order to understand the transport properties of the analyzing magnet (hereafter denoted as M110) a detailed 3D transport simulation has been performed with different starting conditions of the ion beam. In addition to this the second-order transfer coefficients of the magnet have been calculated from the location VT1 in front of the magnet to the location VT2 behind the magnet (see Fig. 4.6).

Fig. 7.1 shows the double focusing bending magnet used as a charged particle analyzer in the KVI-LEBT system. The magnet has a geometrical acceptance of 120 *mm* wide and 60 *mm* high, which is determined by the vacuum chamber. Its radius of curvature is 400 *mm*. The pole faces have a tilt angle of 37° to obtain simultaneous imaging in both transverse planes. The distance from the aperture of the plasma electrode to the effective field boundary (EFB) is 682 *mm*. The distance between the EFB and the image is 374 *mm*. This gives a first order magnification of 0.6.

An illustration of the complex non-linear behaviour of the particle trajectories is shown in Fig. 7.2. In the image plane of the analyzing magnet a 10 *mm* diameter diaphragm is used to select the charge state of interest. The trajectories of 24 $keV\ He^{+}$ ions passing through this diaphragm have been backtracked to the plasma electrode of the ECR ion source. The position of these particles are indicated in blue. The positions of the particles lost at the image plane have been indicated in red. Fig. 7.2 shows the positions of these two groups of particles at various locations in the first part of the LEBT system, i.e. behind the analyzing magnet at the location VT2 (a), behind the extraction

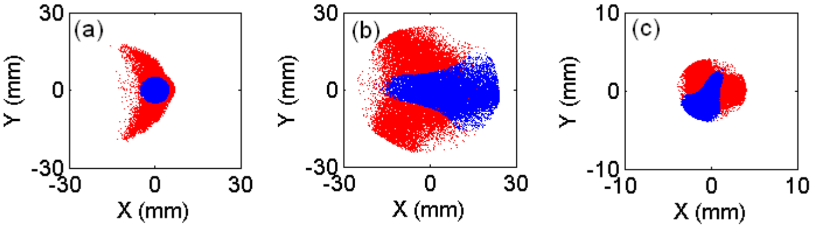

Figure 7.2: *Calculated spatial distributions for a fully space-charge compensated* He^+ *beam in the image plane of the analyzing magnet at the location VT2 (a) and behind the ground electrode at location VT1 (b) and at the aperture of the plasma electrode (c). The blue coloured particles are transported through the* 10 *mm collimator at the location VT2 while the red coloured particles are lost on the collimator.*

system at location VT1 (b) and at the aperture of the plasma electrode (c). The rotation of the beam caused by the magnetic fringe field is clearly visible in Fig. 7.2. Apart from the rotation the decreasing magnetic fringe field of the ECR source also has a strong influence on the beam focusing in the extraction system: without magnetic field a narrow waist would be present at the location of the puller electrode.

In order to separate the effects of the analyzing magnet from those of the properties of the beam extracted from the ECR ion source transport simulations have been performed with different initial conditions, assuming an initially rotationally symmetric uniform ion beam with an emittance of 60 π *mm mrad* at the location of VT1, i.e. the same emittance value as obtained in Sec. 5.3.1. The results of this simulation are shown in Fig. 7.3, which should be compared to the simulation with a realistic beam in Fig. 5.3.

We find that the values of the transported beam emittance in the horizontal (x-plane) and vertical (y-plane) planes differ only slightly for both cases. The beam emittance of the initially round beam at the location of VT2 is around 360 π *mm mrad* (x-plane) and 240 π *mm mrad* (y-plane). This is significantly larger than the design specification (140 π *mm mrad*) of the acceptance of the AGOR injection system [123]. Comparison of the two calculations shows that the observed beam losses and emittance growth (see Fig. 7.2) are essentially due to the transfer properties of the analyzing magnet. The calculated transmission through the diaphragm is 50 % of the total transported beam. Fig. 7.4 shows various phase-space projection of the initially round beam. The colours indicate particles with various x-positions at the location of VT2. For this beam the phase-space distributions at the location of VT2 are distorted in a similar way as observed for a realistic beam in chapter 5 (see Figs. 7.4 and 5.7). This clearly indicates the dominant influence of the magnet properties on the ion beam transport.

The origins of the observed aberrations can be studied by calculating the higher-order transfer matrix of the M110 magnet. In order to correct the aberrations the relevant

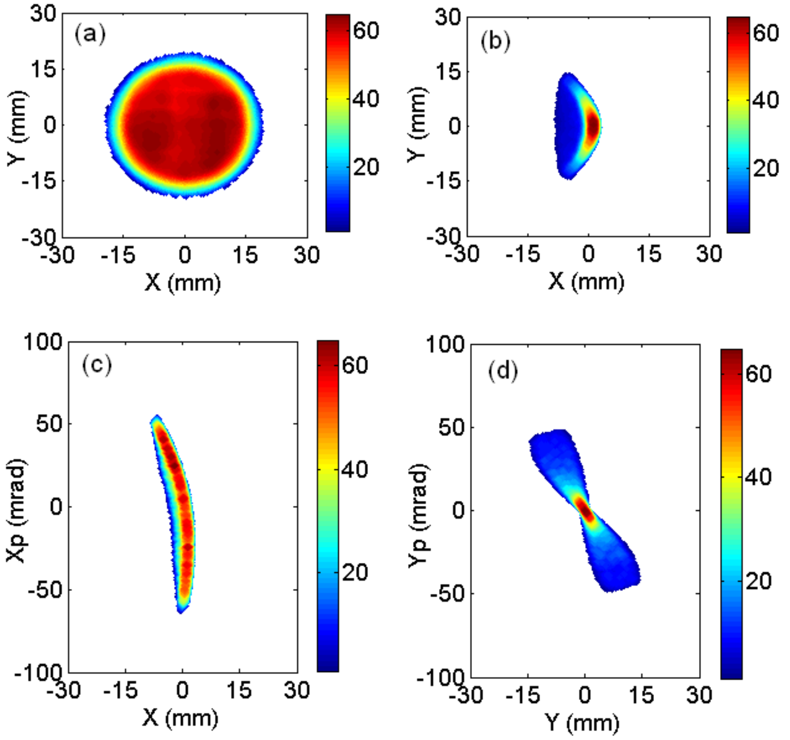

Figure 7.3: *Calculated spatial distributions at location VT1 (a) and at location VT2 (b). Calculated Phase-space distributions at location VT2 in x-plane (c) and y-plane (d) for the phase-space distributions of uncorrelated beam at the location of plasma electrode.*

nonlinear terms in the expansion of its transfer function have to be identified and subsequently reduced by optimization of the magnet geometry. For example, the second-order expansion for the coordinate x can be written as

$$\begin{aligned} x_1 = {} & (x|x)x_0 + (x|x')x'_0 + (x|xx)x_0^2 + (x|xx')x_0x'_0 + (x|x'x')x_0'^2 \\ & + (x|yy)y_0^2 + (x|yy')y_0y'_0 + (x|y'y')y_0'^2 + (x|\delta)\delta_0 \\ & + (x|\delta\delta)\delta_0^2 + (x|x\delta)x_0\delta_0 + (x|x'\delta)x'_0\delta_0 \end{aligned} \tag{7.1}$$

with similar expressions for the coordinates x', y and y' [148]. The second-order coefficients are a mix of both magnetic and kinematic effects. Both effects can be compensated by suitably modifying the pole faces of the magnet.

Tab. 7.1 shows the transfer map of the M110 magnet calculated with COSY INFIN-

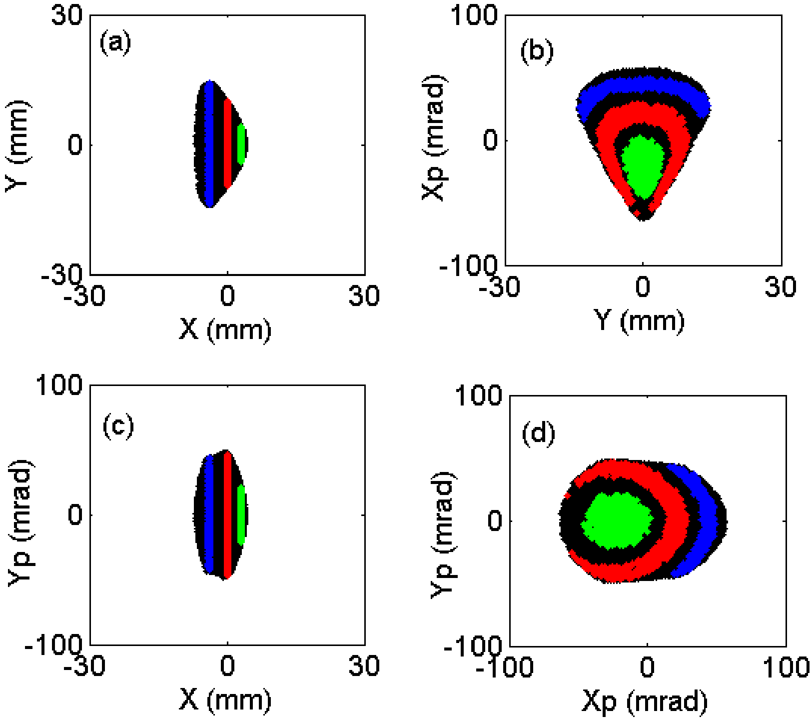

Figure 7.4: *Calculated profiles behind the analyzing magnet (VT2) plotted as a function of* X *with various colours. Spatial profile (a). Mixed phase-space* $(Y \text{ vs } Xp)$ *(b) and* $(X \text{ vs } Yp)$ *(c). Phase profile* $(Xp \text{ vs } Yp)$ *at the same location plotted as a function of* X *(d).*

ITY from the location VT1 to VT2. Fig. 7.5 shows the calculated phase-space distributions at the location of VT2 by applying the second-order coefficients (see Tab. 7.1) to the simulated phase-space distribution at the location VT1 (see Fig. 5.3). Comparison of Fig. 7.5 with Fig. 5.6, which gives the result of the full simulation, demonstrates the dominance of the second-order effects of the M110 magnet on the ion beam transport in comparison with the Fig. 5.6.

The parabolic shape of the image at location VT2 is mainly due to the interplay of $(y|yy)y_0^2$ and $(x|yy)y_0^2$. Particles with significant initial y and y' reach the image plane with significant y. This results in a crescent shape image in the xy-plane at the location of VT2 (see Figs. 7.2a, 7.3b and 7.5c). The $(x|x'x')x_0'^2$ term causes the curved phase-space distribution in the xx'-plane. The bow-tie shape phase-space distribution in the yy'-plane (see Fig. 7.5c) is mainly due to the second-order terms in the y-column of Tab. 7.1. All these non-linear terms together cause a five-fold increase in the effective emittance of a

x	x'	y	y'	ID
-0.496018	-2.303888	0.000000	0.000000	100000
0.348090	-0.399255	0.000000	0.000000	010000
0.000000	0.000000	-0.757739	-1.153239	001000
0.000000	0.000000	0.401070	-0.709306	000100
-2.424614	-1.999897	0.000000	0.000000	200000
-1.967686	-2.429255	0.000000	0.000000	110000
-0.618059	-1.226433	0.000000	0.000000	020000
0.000000	0.000000	-0.509180	7.668750	101000
0.000000	0.000000	-2.264483	4.657631	011000
0.000000	0.000000	-1.151974	-5.335671	100100
0.000000	0.000000	-0.617569	-1.285447	010100
-2.636529	-5.796570	0.000000	0.000000	002000
1.074781	-0.480574	0.000000	0.000000	001100
-0.751168	-0.508179	0.000000	0.000000	000200

Table 7.1: *The different columns correspond to the final coordinates* x; x'; y; y' *and the last column is used for the coordinate identification. The rows contain the various expansion coefficients, which are identified by the exponents of the initial condition. For example, the sixth entry in the first column is the expansion coefficient* $(x|xx')x_0x'_0$ *[39]. These coefficients have been calculated with COSY INFINITY [23] using a built-in fringe field model. Dimensions are in* m *and* rad*.*

transported ion beam through the analyzing magnet. This leads to a decrease in the ion beam transport efficiency of the LEBT system downstream from the analyzing magnet.

7.3 Second-order correction

The analysis described in the previous section clearly shows the large effect of the analyzing magnet on the beam properties. We have therefore investigated the possibilities to improve the beam quality by correcting the aberrations of this magnet. The simulations show that the beam losses occurring on the pole face of the magnet can simply be prevented by increasing the magnet gap from 67 *mm* to 110 *mm*. Several methods for aberration correction have been reported in the literature [24, 147]. The most commonly used multipole correctors are magnetic hexapole and octupole fields. The action of magnetic multipole elements is most effective at positions where the particle beam is large, because these fields affect in particular particles that pass far from the optical axis. The second order aberrations of the analyzing magnet can be compensated by adding hexapole components to the dipole field of the analyzing magnet.

It is also possible to minimize a large second-order aberration by keeping the beam inside the magnetic field narrow, i.e. using an extra focusing element [149, 150]. However, this requires additional optical elements between the extraction system and the analyzing

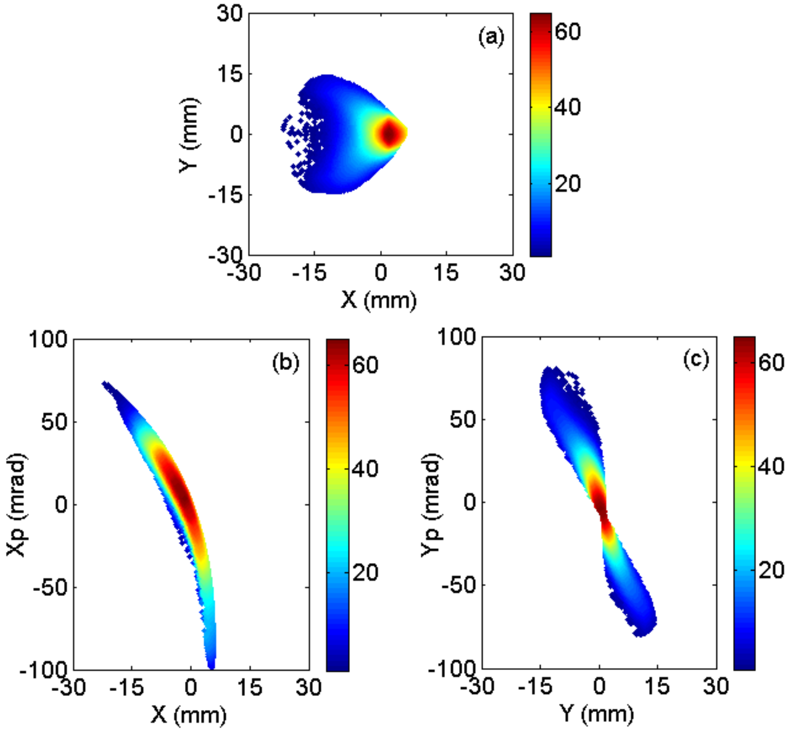

Figure 7.5: *Spatial distributions for a fully space-charge compensated He$^+$ beam in the image plane of the analyzing magnet at location VT2 (a). Calculated horizontal (b) and vertical (c) emittance plot of a fully compensated He$^+$ beam at the same location VT2. The calculations were made with COSY INFINITY.*

magnet, which in our case is difficult because of lack of space. Therefore, we have chosen to further investigate the option of superimposing multipole fields on the dipole field of the analyzing magnet as previously developed by Leitner, et al. [151].

The pole faces at the entrance and exit sections are shaped in such a way that a quadratically increasing field is obtained to correct the vertical hexapole component, while the central part of the pole face shape is modified to obtain a quadratically decreasing magnetic field to correct the horizontal hexapole component. The modified pole face shape of the analyzing magnet is shown in Fig. 7.6. We used COSY INFINITY to quickly estimate the required hexapole strengths and then the LORENTZ3D code for the fine tuning of the pole face shape and for trajectory calculations.

The phase-space distribution calculated at the location of VT1 (see Fig. 5.3) is used as the initial condition for the transport simulations. The space-charge force is not taken into account, i.e. a fully-compensated He^+ beam is assumed.

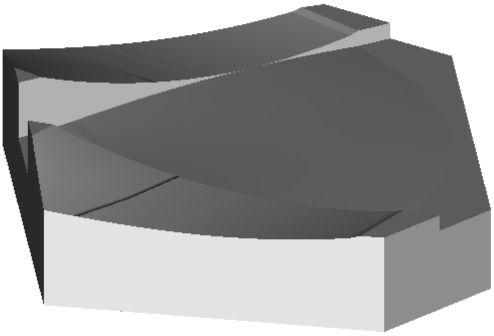

Figure 7.6: *Pole face of the analyzing magnet including the hexapole correction.*

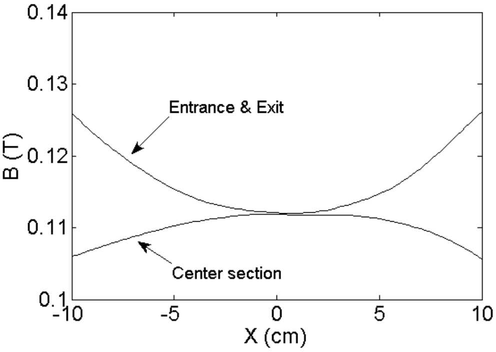

Figure 7.7: *Optimum magnetic field profile in the middle of the entrance (exit) and central sections as a function of the horizontal distance from the central trajectory.*

The calculated beam profile and emittance plots at the location of VT2 for the optimized pole shape are shown in Fig. 7.8. It should be pointed out that the location of VT2 is slightly displaced with respect to the image plane of the analyzing magnet. Shifting VT2 to the image plane would still improve the beamspot. Comparison of Fig. 7.9 with Fig. 5.7 shows that the correlation between the transverse angle $R_p = \sqrt{X_p^2 + Y_p^2}$ and X has been almost completely removed by the optimization of the magnet. As can be seen in Fig. 7.8(a) and (b) a small ($\approx$ 10%) fraction of the beam particles is deflected too much. The simulation shows that these particles are on the left side of the beam before entering the analyzing magnet. By carefully decreasing the field integral on the inner side of the magnet we might remove this tail without affecting the vertical focusing too much. According to the simulations the full beam is transported to the location of VT2 and the horizontal and vertical effective emittances are decreased with a factor of two compared to the uncorrected values.

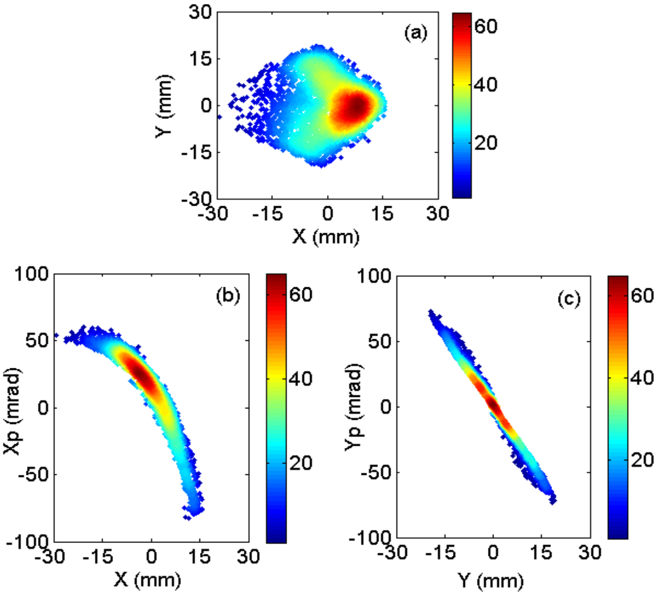

Figure 7.8: *Calculated spatial distribution for a fully space-charge compensated He^{+} beam at the location of VT2 behind the modified analyzing magnet (a). Calculated horizontal (b) and vertical (c) emittance plots at the same location.*

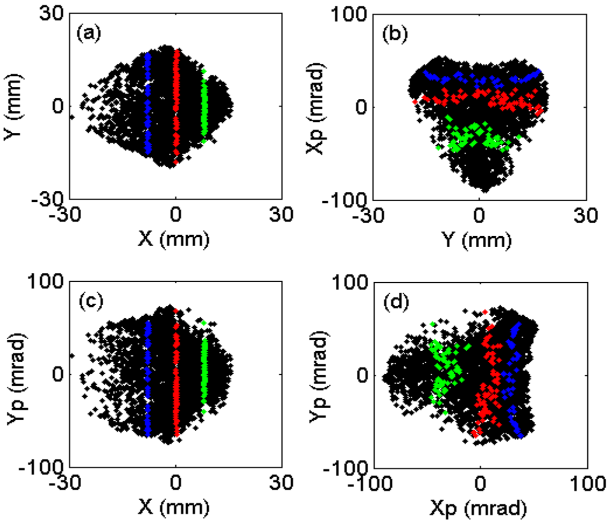

Figure 7.9: *Calculated profiles for the analyzing magnet with the modified pole face at location (VT2) plotted as a function of X with various colours . Spatial profile (a). Mixed phase-space (Y vs Xp) (b) and (X vs Yp) (c). Phase profile (Xp vs Yp) at the same location plotted as a function of X with same colours (d).*

7.4 Conclusions

The simulations described in this chapter demonstrate that the 110° analyzing magnet is the main cause of beam losses and emittance growth of the transported beam. The beam losses can simply be prevented by increasing the pole gap of the magnet from 67 *mm* to 110 *mm*. Insight into the aberration coefficients of the magnet has been obtained by expanding its transfer map up to second-order. Using this transfer map together with detailed 3D magnetic field and ion trajectory calculations we propose to modifying the pole faces of the analyzing magnet by adding hexapole terms to the main dipole field. This will result in a significant reduction of the beam losses and effective emittance growth due to the analyzing magnet. We estimate that such a modification will increase the effective transport efficiency to the AGOR cyclotron as calculated in Sec. 6.4.2 from 16 % to 45 %.

Chapter 8

EXTRACTION AND TRANSPORT AT THE GSI-EIS BEAMLINE

8.1 Introduction

In the framework of the KVI-GSI collaboration we have performed a simulation study of the extraction and transport of ion beams for the ion source test stand at GSI consisting of a CAPRICE ECR ion source [152] and the EIS beam analyzing system [153]. Section 8.2 briefly describes the CAPRICE ECR ion source and the EIS test bench at GSI. A simulation of He^{+} beams and measurements for this beam at location VT2 behind the beamline solenoid (see Fig. 8.1) is presented in Sec 8.3.

Furthermore, simulations have also been performed for Ar^{7+} beams with two different initial distributions, one calculated with the KOBRA3D-INP code [114] and the other one calculated with our PIC-MCC code [33]. The results are presented in Sec. 8.4. The simulations reported in this chapter assume fully space-charge compensated beams and concentrate on possible effective emittance growth due to ion-optical aberrations of the beamline elements.

8.2 CAPRICE and EIS test bench

The CAPRICE ECR ion source and the EIS test bench at GSI are schematically shown in Fig. 8.1. Three diagnostic chambers with viewing targets are installed at the EIS test bench, i.e. VT1 located directly behind the extraction system of the ion source, VT2 near the location of the focal plane behind the beamline solenoid, while the third one, VT3, is located at the image plane of the analyzing system. A magnetic quadrupole has been installed in front of the dipole magnets to optimize the matching of the extracted ion beam to the acceptance of the analyzing system and at the same time improve its mass resolution. Emittance monitors can be installed at the locations of VT1 and VT3.

A schematic view of the CAPRICE ion source is shown in Fig. 8.2. The source has a relatively small plasma chamber with a length of 16 *cm* and a diameter of 6.6 *cm* diameter. The axial mirror field is produced with two solenoids generating a magnetic field profile along the axis as shown in Fig. 8.3. The hexapole field is produced with a NdFeB permanent magnet in the Hallbach configuration [154]. The maximum field of this magnet at the plasma chamber wall is approximately 0.9 T. The electrons in the plasma of the CAPRICE source are resonantly heated with 14 *GHz* microwaves which are injected along the axis of the plasma chamber by a coaxial waveguide.

The ion beams are extracted from the ion source with an accel-decel extraction system (see Fig. 8.4). The extraction system consists of three electrodes: a plasma electrode with an aperture of 10 *mm*, a puller electrode with an aperture of 16 *mm* and a ground electrode with a maximum inner diameter of 40 *mm*. In all simulations we assumed that the plasma electrode is biased at $+14.2$ kV and the puller electrode at -1 kV.

A focusing solenoid is located behind the extraction system. The two dipole magnets of the analyzing system are equipped with shims and clamps to minimize aberrations. These could not be taken into account in our analysis because the drawings of these parts were not available.

8.3 Extraction and transport of He^+ beam

To simulate the extraction of the ion beam from the source and its subsequent transport through the low-energy beamline we used the General Particle Tracer (GPT) code [37]. For the quadrupole and dipole magnets the internal models of GPT were used. These models use realistic second-order fringe fields. More details of the GPT code are discussed in Sec. 2.4. Our previous calculations for the KVI-AECR ion source show that the fringe field of the hexapole magnet has a negligible effect on the trajectories of the extracted ions. Therefore, we did not include the fringe field of the hexapole magnet in the present beam extraction and transport simulations. We used the POISSON code [157] to calculate the solenoid magnetic field of the ion source, the electric fields in the extraction system and the magnetic field of the focussing solenoid, which all have axial symmetry.

In this section the results of a 14.2 *keV* mono-component He^+ beam is presented. For this beam a clean comparison with beam profile and emittance measurements is possible. The initial phase-space distribution of the He^+ ions in the plane of the plasma electrode aperture has been calculated with the PIC-MCC code. In this simulation a

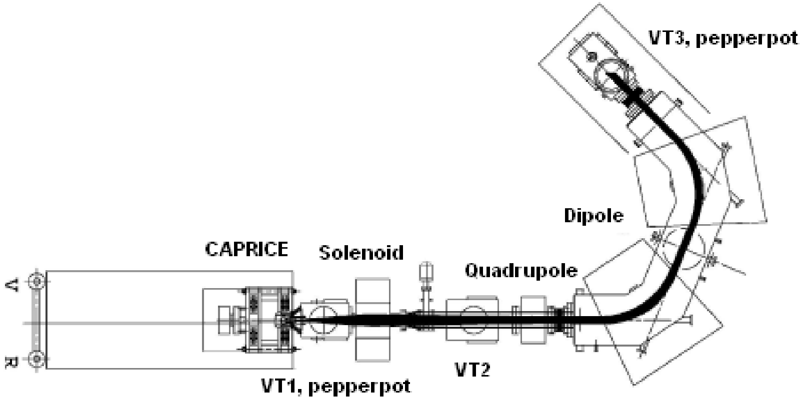

Figure 8.1: *EIS test bench [155].*

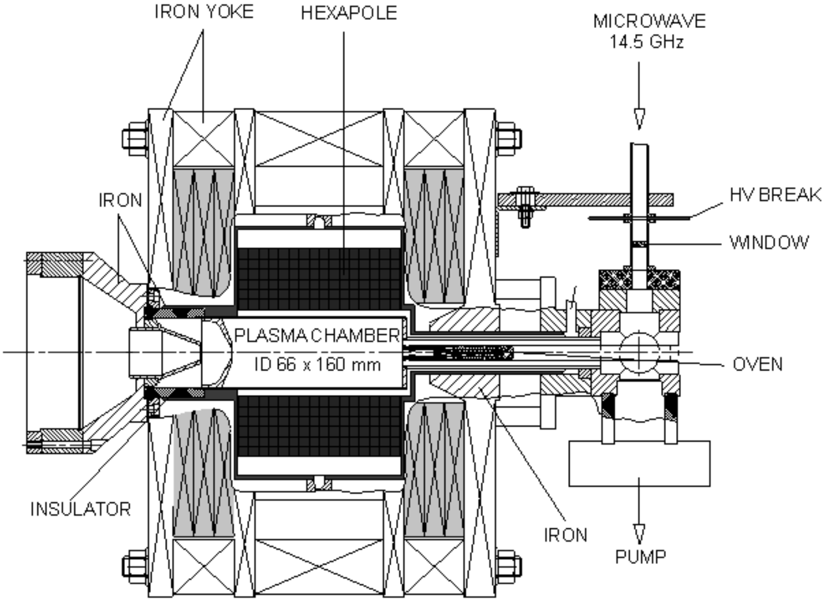

Figure 8.2: *ECR ion source CAPRICE [156].*

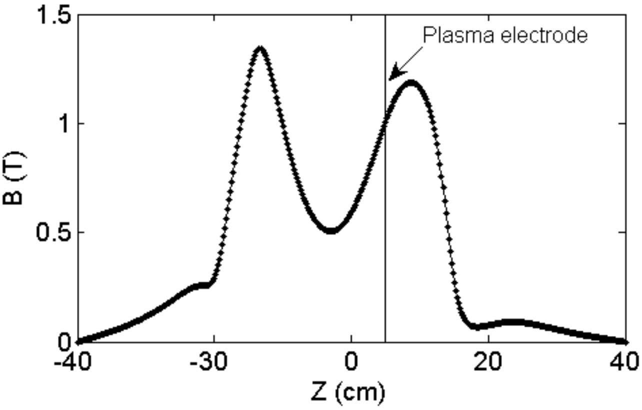

Figure 8.3: *Calculated magnetic field along the axis of the ECR ion source.*

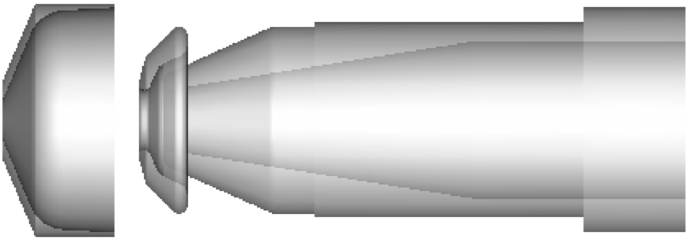

Figure 8.4: *Accel-decel extraction system used in the ECR ion source.*

plasma sheath as described in chapter 5 was used. Furthermore, our previous simulation results presented in chapter 5 and chapter 6 show space-charge forces are negligible for the range of ion currents considered here. Therefore, we also assume that the beam is fully space-charge compensated, i.e. that the effective beam current is zero.

The effective emittance value of the extracted beam at the location of VT1 directly behind the extraction system is 140 π *mm mrad* in both planes. The method for calculating the effective emittance is discussed in Sec. 2.2.2. The spatial profile and transverse phase-space distribution in the horizontal plane at the location of VT2 behind the solenoid are shown in Fig. 8.5 for a few different settings of the solenoid current. For the horizontal and vertical effective emittances of the He^+ beam at this location we find values of approximately 160 π *mm mrad* in both planes.

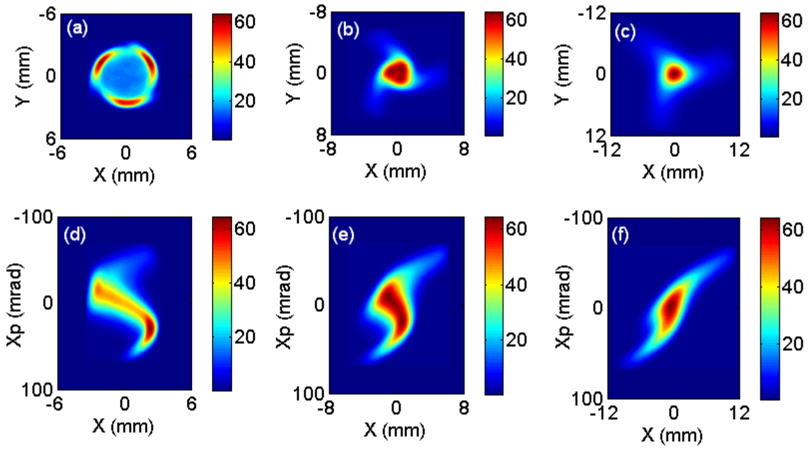

Figure 8.5: *Top row: Calculated spatial distribution of a* 14.2 *keV He$^+$beam at the location of VT2 behind the beamline solenoid with increasing focusing strength of the beamline solenoid (from figure left side to right). Bottom row: Calculated phase-space distribution in the horizontal plane of the same beam.*

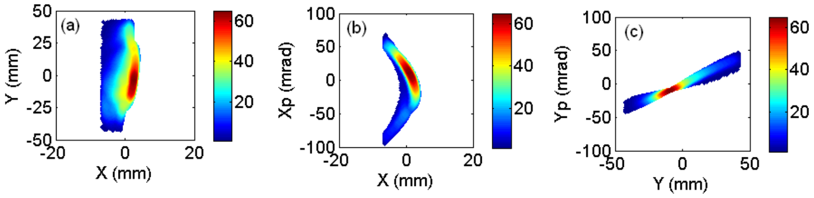

Figure 8.6: *Calculated spatial distribution of the He$^+$ beam at the location of VT3 behind the analyzing system (a). Horizontal (b) and vertical (c) phase-space distributions at the location of VT3.*

The magnetic quadrupole in front of the analyzing magnets has been optimized to match the acceptance of the analyzing magnets. We then transported the beam through the analyzing magnets and calculated both the spatial and transverse phase-space distributions in the center of diagnostics box VT3 behind the analyzing system. These are shown in Fig. 8.6. Calculated horizontal and vertical effective emittances of the He^+ beam in the image plane of the analyzing magnet are 340 π $mm\ mrad$ and 200 π $mm\ mrad$, respectively. This is significantly larger than the effective emittances calculated in front of the analyzing system and caused by non-paraxial effects and ion-optical aberrations. However, the real emittances might be slightly smaller than the calculated ones, because we did not take into account the real fringe fields of the analyzing system. The calculated transmission for the He^+ beam from the ground electrode to the image plane of the

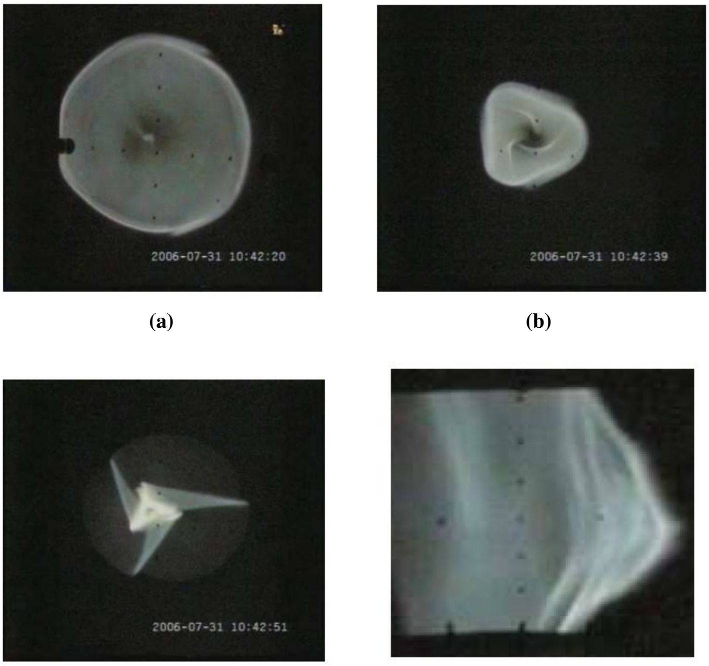

(a) **(b)**

(c) **(d)**

Figure 8.7: *Measured beam profiles of a He^+ beam at the location of VT2 behind the beamline solenoid with increasing focusing strength from figure (a) to (c).Measured beam profiles of a He^+ beam at the location of VT3 behind the analyzing (d) [158].*

analyzing magnet is approximately 80 %.

Comparison of the calculated beam profiles in Fig. 8.5 with the measured beam profiles (see Fig. 8.7) at the location of VT2 behind the beamline solenoid shows that the shape of the simulated beam profiles are similar to those found experimentally. The transport simulations through the solenoid show that the beam has a hollow core and large aberrations in the focal plane of the solenoid for both sets. The large initial emittance of the beam extracted from the ECR ion source causes it to fill the aperture of the solenoid to a very large extent and therefore the spherical aberrations of the solenoid [18] strongly influence the image quality. Charged particles far from the optical axis experience a stronger force and will cross the axis before those particles that are more close to the axis. This leads to the hollow beam profile at the location of VT2 (see Figs. 8.10 and 8.11). It has been reported that the use of a solenoid in LEBT systems can lead to significant beam degradation and hollow beams [125, 149, 150, 159–162], in particular for intense multiple-charge state beams. The proposed explanation is that this is caused by a strong focusing of particles with a higher charge-to-mass ratio compared to particles with a smaller charge-to-mass ratio. The space charge forces then push the particles with a smaller charge-to-mass ratio radially outward. Our simulations show, however, that even without space-charge effects a solenoid can produce a hollow beam profile because of image aberrations. Also the calculated beam profile at the location of VT3 behind the analyzing magnet (see Fig. 8.6a) exhibits similar features as the measured beam profile at the same location (see Fig. 8.7d). The qualitative agreement between simulation and measurement clearly indicates that our simulations reproduce the basic mechanisms of beam formation, extraction and transport.

8.4 Extraction and transport of Ar^{7+} beam

For the simulation of an Ar^{7+} beam we have used two sets of initial condition in order to assess their influence. Set A has been calculated with the KVI PIC-MCC code. In this calculation the geometry and magnetic field configuration of the GSI CAPRICE ECR ion source have been used. The initial conditions of set A are given at the plasma electrode of the source.

Set B has been calculated with the KOBRA3-INP code also using the geometry and magnetic field configuration of the same source. In this set the initial conditions are defined at the location of viewing target VT1, at the exit of the extraction system. The data were provided by Mr. P. Spädtke, GSI. Both sets contain around 64000 particles. For a direct comparison of both sets the particles of set A were tracked through the extraction system and the fringe field of the ion source to the location at which B has been specified.

The spatial distribution and emittances for both sets at the location VT1 are displayed in Figs. 8.8 and 8.9. The effective emitance of set A amounts to 120 π *mm mrad*, while for set B it is 510 π *mm mrad*. We attribute the large difference between these two values to the different radial dependence of the ion density distribution across the plasma electrode aperture for sets A and B. Only emittance measurements directly after the extraction system will resolve this issue.

For the subsequent beam transport simulations the current through the solenoid and the setting of the quadrupole have been optimized to obtain a minimum beam spot size in the focal plane of the solenoid and a maximum transmission through the analyzing system. The same settings have been used for both sets. We assumed full space-charge compensation in the simulations. The spatial profile, horizontal and vertical phase-space distributions of the Ar^{7+} beam in set A at the location of VT2 are shown in Fig. 8.10. Fig. 8.11 shows the profiles of the ion beam for set B at the same location. The beam was then tracked through the analyzing magnets and the spatial and transverse phase-space distributions of the Ar^{7+} beam in the center of the diagnostics box (at the location VT3)

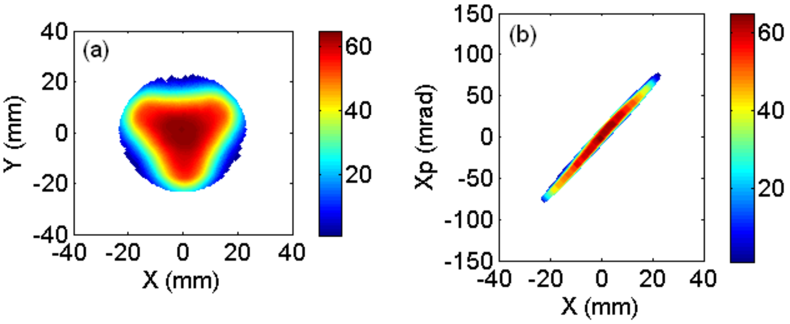

Figure 8.8: *Calculated spatial distribution of the* Ar^{7+} *beam for set A behind the ground electrode at the location of VT1 (a). Horizontal phase-space distributions at the location of VT1 (b).*

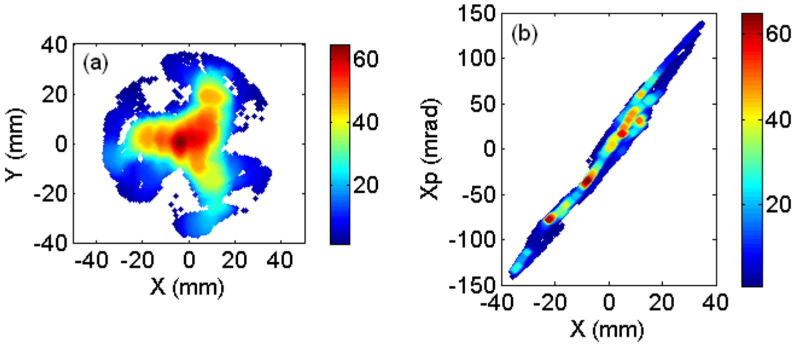

Figure 8.9: *Calculated spatial distribution of the* Ar^{7+} *beam for set B behind the ground electrode at the location of VT1 (a). Horizontal phase-space distributions at the location of VT1 (b).*

behind the analyzing system were calculated for both sets of initial conditions. These distributions are shown in Fig. 8.12 for the beam in set A and in Fig. 8.13 for the beam of set B. Because of its large emittance 40 % of the beam is lost during the transport for set B, while for set A the transmission is 100 %. For the Ar^{7+} beam we observe a hollow core in the focal plane of the solenoid with both datasets (see Figs. 8.10 and 8.11), similar to what was found for the He^{+} beam.

In the previous chapter it has been shown that it is very important to reduce the filling of the analyzing magnet, in particular in the vertical direction that usually has the smallest gap, in order to minimize beam losses and aberrations. In the GSI low energy beamline this reduction of the vertical beamsize in the analyzing magnets is done with the solenoid and a subsequent vertically focussing quadrupole. However, the simulation results show that the solenoid produces large aberrations with a hollow beam profile. As a result the effective emittance after the beam transport through the analyzing magnet is significantly

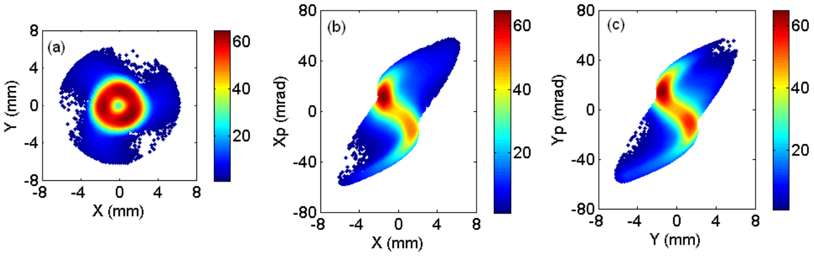

Figure 8.10: *Calculated spatial distribution of the Ar^{7+} beam with initial set A at the location of VT2 behind the beamline solenoid. Horizontal (b) and vertical (c) phase-space distributions at the location of VT2.*

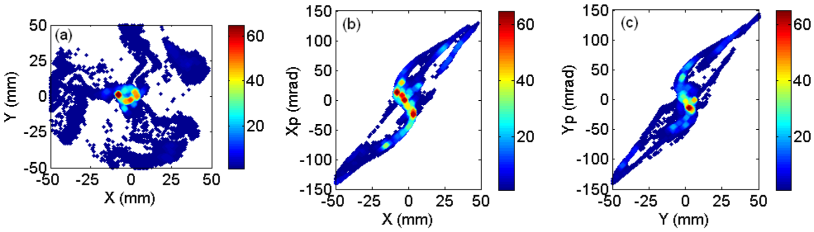

Figure 8.11: *Calculated spatial distribution of the Ar^{7+} beam with initial set B at the location of VT2 behind the beamline solenoid. Horizontal (b) and vertical (c) phase-space distributions at the location of VT2.*

increased. The phase-space distributions of the Ar^{7+} beam at the location of VT3 behind the analyzing magnets are rather similar for both initial distributions, although the spatial distribution of set B shows some hot spots that are absent in the simulation for set A. The ion beam transported through the solenoid and the analyzing magnet has a large effective emittance because of the aberrations of the solenoid and the dipole magnets and the large initial emittance, in particular for the set B. The horizontal and vertical effective emittances for the set A beam in the image plane of the analyzing magnet are 220 π *mm mrad* and 205 π *mm mrad*, respectively. The effective emittance values for the set B beam at this location are 300 π *mm mrad* and 450 π *mm mrad*, respectively.

8.5 Conclusions

We have performed simulations of extraction and transport of He^{+} and Ar^{7+} beams for the CAPRICE ECR ion source and EIS test bench at GSI, Darmstadt. The results of He^{+} beam have been compared with measurements at the location of VT2 behind the beamline solenoid. The qualitative agreement between calculated beam profiles and measured ones

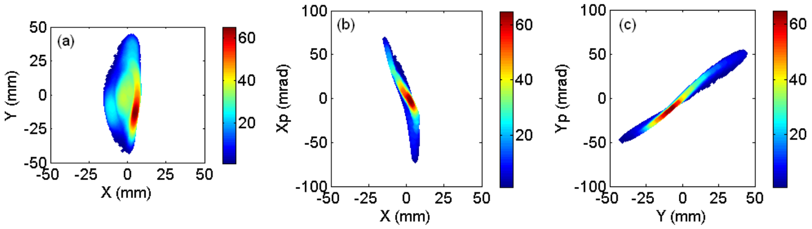

Figure 8.12: *Calculated spatial distribution of the* Ar^{7+} *beam with initial set A at the location of diagnostics box VT3 behind the analyzing system. Horizontal (b) and vertical (c) phase-space distributions at the location of VT3.*

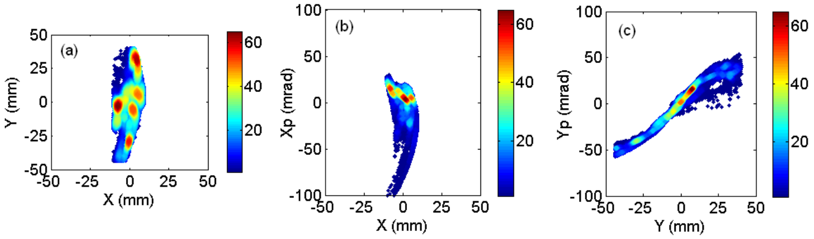

Figure 8.13: *Calculated spatial distribution of the* Ar^{7+} *beam with initial set B at the location of diagnostics box VT3 behind the analyzing system. Horizontal (b) and vertical (c) phase-space distributions at the location of VT3.*

shows that the basic physics is well reproduced in the simulations.

The spherical aberration of the solenoid in combination with the large beam size results in a hollow beam profile in its focal plane. Previously this phenomenon has been solely attributed to space-charge effects; our simulation shows that there is no need to invoke space-charge effects to produce this phenomenon.

From a comparison of the simulations for the test bench at GSI and the setup of the AECR ion source at KVI we draw the following conclusions:

- The insertion of a solenoid between the ion source and the analyzing magnet leads to a significant increase of the effective emittance already before the analyzing magnet and thereby amplifies the effect of the aberrations of the analyzing magnet itself and increases the beam losses in the system.

- The use of a vertically focussing quadrupole in front of the analyzing magnet reduces the beamsize in the fringe fields at the entrance and exit of the magnet and thereby reduces the effect of the aberrations on the effective emittance of the charge state analyzed beam. It is preferable to use a magnetic lens for two reasons: the space-charge compensation in this high intensity region is not adversely affected and the different charge states will be vertically focussed at different locations along the beam axis, thus reducing space-charge effects.

Chapter 9

CONCLUDING REMARKS AND OUTLOOK

9.1 Concluding remarks

The operational experience with ECR ion sources at heavy ion accelerators shows that in general significant losses occur in the low energy beam transport system between the ion source and the accelerator. As an example, the 25 m long beamline between the KVI AECR-source and the AGOR-cyclotron has a typical transmission of about 20 %. Similar values have been reported by other laboratories [163]. Various hypotheses for this low transmission have been advanced, mostly focusing on the asymmetric phase-space distribution of the beam extracted from ECR sources and the angular momentum of the beams caused by the combination of electric and magnetic fields in the extraction region of the source [163]. However, only little evidence for these hypotheses has been presented up to now.

In this thesis an extensive simulation study based on ion trajectory calculations of the beam formation, extraction and transport of highly charged heavy ions from the 14 GHz KVI AECR source is presented. Both higher order aberrations in the transport of the large emittance, low energy beams extracted from the ECR source and space-charge effects have been investigated. The initial conditions needed to start the trajectory calculations have been obtained with an in-house developed PIC-MCC code which simulates the detailed 3D ion dynamics in the plasma of the ECR ion source. We have performed extensive simulations of mono-component He^{+} and multi-component Ne^{q+} beams up to the imaging plane of the analyzing system yielding detailed 4D phase-space distributions of the ions at various positions along the beamline. The simulations have been benchmarked by comparing the calculated phase-space distributions with measurements of beam profiles and emittances. For the beam emittance measurements we used an in-house developed pepperpot emittance meter with which the full 4D transverse phase-space distribution of low-energy ion beams can be determined. This is important because ion beams extracted from ECR sources generally show strong correlations between the horizontal and vertical planes which are missed in the often-used Allison-type emittance meters.

Our simulations and measurements show good agreement which indicates that the important physical processes determining ion beam formation, extraction and transport in the parameter regime investigated are properly incorporated in the codes. The simulations demonstrate that the non-paraxiality is a much more important aspect for low-energy ion beams extracted from ECR sources than their asymmetric phase-space distributions which, as we have shown in chapter 7, do not have a large effect on the subsequent transport. On the other hand, non-paraxial beams tend to fill up the entire beamline aperture thereby amplifying the ion-optical aberrations of the beamline elements.

The good agreement between simulation and measurement shows that the performance of low-energy ion beam transport systems can be accurately predicted with modern simulation tools using realistic 3D magnetic and electric fields at beam current levels up to at least a few *mA*. Therefore these tools should be used to optimize the design of such systems. Our simulations and measurements clearly show that the large beam losses in the LEBT line are caused by emittance growth in the analyzing magnet because of its large second-order aberrations. In addition, a significant fraction of the incident ion beam is lost in the magnet because of its too small pole gap. The simulations described in chapter 7 show that the ion-optical properties of the analyzing magnet can be improved by increasing its pole gap and compensating the second-order aberrations by suitably modifying the shape of the pole faces, i.e. adding hexapole components to the main dipole field. In this way we expect to increase the beam transmission to the cyclotron from 20 % to 45 %.

Finally, we have also simulated beam formation, extraction and transport of He^{+} and Ar^{7+} beams from the CAPRICE ECR ion source at the EIS test bench of GSI, Darmstadt. Two sets of simulations have been performed with different initial conditions, i.e. one using the KVI PIC-MCC code and the other using initial conditions calculated with the KOBRA3D-INP code. The results of both simulations differ significantly showing the importance of a good model for the beam formation in the ECR ion source. Beam emittance measurements, preferably with a pepperpot emittance meter, should settle this issue but have not been performed yet. In addition, the simulations indicate that one should not install a focusing solenoid directly behind the ECR ion source. Its third-order aberrations lead to emittance growth of the ion beam. Instead, installing a vertically-focussing magnetic quadrupole between ion source and analyzing system is very attractive, because *i)* it decreases the effect of the analyzing magnet's second-order aberrations and thus its contribution to emittance growth and *ii)* it increases the mass-analyzing power of the magnet.

We also have performed simulations with different degrees of space-charge compensation. Comparison with the measurements clearly indicates that up to the maximum beam currents investigated ($2.3\ mA$) both the He^{+} and Ne^{q+} beams are fully space-charge compensated. At these intensities a small deviation of only 10 % from full space-charge compensation would already lead to a significant increase of the effective emittance of the Ne^{q+} beam, which has not been observed, thereby showing the importance of effective space-charge compensation for low energy high intensity beams.

9.2 Outlook

The current state-of-the-art ECR ion sources [7,164–166], which are based on superconducting technology to generate both the solenoidal and hexapolar fields, operate with an RF-frequency of 24–28 *GHz*. The magnetic fields in these sources are thus typically a factor two higher than in the 14 *GHz* KVI AECR (and CAPRICE) ion sources for which the beam formation, extraction and transport were studied in this thesis. Consequently the emittance of the beams delivered by these sources is also typically a factor two larger than the emittance of the beams produced by the KVI AECR ion source. Compensation of the higher order aberrations in the beam transport caused by both the non-paraxiality of the beams and the higher order terms in the fields of the optical elements in order to minimize beam losses becomes even more important than it already is in our case. For an optimal design of beam guiding systems for low energy highly charged ions a detailed analysis of the higher order aberrations based on realistic 3D fields and of the kinematic perturbations is therefore essential.

Furthermore, these superconducting sources deliver a total ion current of 15–20 *mA*, to be compared with at most 2–3 *mA* for the KVI AECR and other 14 *GHz* ECR ion sources. The simulations of the effects of space-charge compensation of a Ne^{q+} beam presented in chapter 6 show that for a total current of 2.3 *mA* significant emittance growth occurs already at a compensation level of 90 %. This implies that at the output currents for the superconducting sources the beam space-charge should be compensated beyond 99 % in order to prevent significant emittance growth. As the details of the mechanism of space-charge compensation are not well understood, a systematic study of the space-charge compensation as a function of various parameters, such as pressure, residual gas composition etc., under well controlled conditions should be conducted. Also the possibilities to actively inject low energy electrons into the beam should be investigated. On the other hand, the electrons compensating the space-charge can also cause beam loss via recombination. In addition, the residual gas, which is the main source of these electrons and which therefore can not be reduced at will, also leads to losses via charge exchange collisions. Whether or not the combination of these effects leads to a maximum achievable brilliance of the beams is not clear and should be clarified in such a study.

For future sources operating at still higher frequencies and fields (the use of 60 GHz RF power is anticipated [167]), the full control of both the aberrations and the space-charge compensation is clearly essential for the successful exploitation of the potential of these sources.

Bibliography

[1] R. Geller, *Electron Cyclotron Resonance Ion Sources and ECR Plasmas*, IOP, London, 1996.

[2] H. Wilschut, AIP Conf. Proc. **802**, 223 (2005).

[3] P. Spille, Proceedings of HB2006, Tsukuba, Japan , MOBP02 (2006).

[4] Y. Yano, Nuclear Instruments and Methods in Physics Research Section B: Beam Interactions with Materials and Atoms **261**, 1009 (2007).

[5] D. J. Morrissey, Journal of Physics: Conference Series **267**, 012001 (2011).

[6] M.-H. Moscatello, Proceedings of LINAC, Lübeck, Germany , MO301 (2004).

[7] T. Nakagawa, Y. Higurashi, J. Ohnishi, T. Aihara, M. Tamura, A. Uchiyama, H. Okuno, K. Kusaka, M. Kidera, E. Ikezawa, M. Fujimaki, Y. Sato, Y. Watanabe, M. Komiyama, M. Kase, A. Goto, O. Kamigaito, and Y. Yano, Review of Scientific Instruments **81**, 02A320 (2010).

[8] D. Leitner, C. M. Lyneis, S. R. Abbott, R. D. Dwinell, D. Collins, and M. Leitner, AIP Conference Proceedings **749**, 3 (2005).

[9] L. T. Sun, H. W. Zhao, W. Lu, X. Z. Zhang, Y. C. Feng, J. Y. Li, Y. Cao, X. H. Guo, H. Y. Ma, H. Y. Zhao, Y. Shang, B. H. Ma, H. Wang, X. X. Li, T. Jin, and D. Z. Xie, Review of Scientific Instruments **81**, 02A318 (2010).

[10] P. Zavodszky, B. Arend, D. Cole, J. Dekamp, G. Machicoane, F. Marti, P. Miller, J. Moskalik, J. Ottarson, and J. Vincent, Nuclear Instruments and Methods in Physics Research Section B: Beam Interactions with Materials and Atoms **241**, 959 (2005).

[11] L. Spitzer, *Focusing of charged particles*, Academic Press, New York, Vol. II, 1967.

[12] Z. Q. Xie, *The effect of space charge force on beams extracted from ecr ion sources*, PhD thesis, Michigan State University, USA, 1989.

[13] W. K. Vogt, H. Beuscher, H. L. Hagedoorn, J. Reich, and P. Wucherer, Nucl. Instrum. Methods Phys. Res. A **268**, 5 (1988).

[14] D. Leitner, Proceedings of BIW10, Santa Fe, New Mexico, US, , WEIMNB01 (2010).

[15] S. Brandenburg et al., Proceedings of the 17th International Conference on Cyclotrons and Their Applications, Tokyo, Japan (2004).

[16] H. R. Kremers, J. P. M. Beijers, S. Brandenburg, I. Formanoy, J. Mulder, J. Sijbring, H. Koivisto, and K. Rantilla, AIP Conference Proceedings **749**, 175 (2005).

[17] H. Wiedemann and H. Wiedemann, in *Particle Accelerator Physics*, Springer Berlin Heidelberg, 2007.

[18] M. Reiser, *Theory and Design of Charged Particle Beams*, WILEY-VCH, Weinheim, 2008.

[19] D. C. Carey, *Optics of Charged Particles*, Academic Press Limited, London, 1987.

[20] see http://iapdlpc.physik.uni-frankfurt.de/texte/chapter3.html.

[21] P. M. Lapostolle, IEEE Trans. Nucl. Sci **3**, 1101 (1971).

[22] J. Buon, CERN Accelerator School Fifth General Accelerator Physics Course **vol. I**, 89, CERN 94 (Geneva 1994).

[23] See the homepage of cosy infinity, $http://bt.pa.msu.edu/index\_cosy.htm$.

[24] H. Wollnik, *The Optics of Charged Particle Beams*, Harwood academic publishers, Berkshire, UK, 1992.

[25] K. Wille, *The Physics Of Particle Accelerators*, OXFORD University Press, Oxford, UK, 2005.

[26] *Accelerator School: Intermediate Course on Accelerator Physics*, Zeuthen, Germany, Sep 2003, pp.305-320, CAS - CERN proceedings.

[27] A. J. T. Holmes, Phys. Rev. A **19**, 389 (1979).

[28] V. Toivanen, V. Aho, J. Kauppinen, H. Koivisto, T. Ropponen, O. Tarvainen, and J. Ärje, Proceedings of CYCLOTRONS 2010, Lanzhou, China, **MOPCP050**, 1 (2010).

[29] I. A. Soloshenko, Review of Scientific Instruments **67**, 1646 (1996).

[30] I. A. Soloshenko, Review of Scientific Instruments **69**, 1359 (1998).

[31] V. Toivanen, O. Steczkiewicz, O. Tarvainen, T. Ropponen, J. Ärje, and H. Koivisto, Nuclear Instruments and Methods in Physics Research Section B: Beam Interactions with Materials and Atoms **268**, 1508 (2010).

[32] D. Winklehner et al., Proceedings of the 19th International Workshop on ECR Ion Sources was held in Grenoble, France, , TUCOAK03 (2010).

[33] V. Mironov and J. P. M. Beijers, Phys. Rev. ST Accel. Beams **12**, 073501 (2009).

[34] C. R. Prior, AIP Conf. Proc. **693**, 32 (2003).

[35] See the homepage of lorentz http://www.integratedsoft.com/products/lorentz/default.aspx.

[36] T. Laforce, Boundary element method course notes:pe281, www.Stanford.edu.

[37] See the homepage of gpt http://www.pulsar.nl/gpt/.

[38] See gpt manual, $http : //www.pulsar.nl/gpt/$.

[39] *See COSY INFINITY manual*, $http : //bt.pa.msu.edu/index\_cosy.htm$.

[40] H. Postma, Phys. Lett. A **31**, 196 (1970).

[41] W. H. S. Bliman, R. Geller and B. Jaquot, IEEE Trans. Nucl. Sci **NS-19**, 200 (1972).

[42] K. Bernhardi and K. Wieseman, Plasma Phys. **14**, 1073 (1972).

[43] L. D. C. G. R. Bardet, P. Briand and G. Melin, Nucl. Fusion **15**, 865 (1975).

[44] R. G. P. Briand and B. Jaquot, Nucl. Instrum. Methods **131**, 407 (1975).

[45] R. J. Goldston and P. H. Rutherford, *Introduction to Plasma Physics*, IOP Publishing Ltd., London, 1995.

[46] Z. Q. Xie and C. M. Lyneis, Rev. Sci. Instrum. **69**, 2947 (1994).

[47] Z. Xie and C. Lyneis, Proceedings of the 13th International Workshop on ECR Ion Sources, College station, , 16 (1997).

[48] H. Koivisto et al., Nucl. Instrum. Methods Phys. Res. B **174**, 379 (2001).

[49] H. R. Kremers et al., Rev. Sci. Instrum. **77**, 03A311 (2006).

[50] R. Watson, D. Church, R. Tribble, L. Yang, B. Bandong, and T. Lotze, Nuclear Instruments and Methods in Physics Research Section B: Beam Interactions with Materials and Atoms **56-57**, 223 (1991).

[51] H. Koivisto, J. DeKamp, and A. Zeller, Nuclear Instruments and Methods in Physics Research Section B: Beam Interactions with Materials and Atoms **174**, 373 (2001).

[52] M. Schlapp, R. C. Pardo, R. C. Vondrasek, J. Szczech, P. J. Billquist, J. Vieregg, Z. Q. Xie, C. M. Lyneis, and R. Harkewicz, Review of Scientific Instruments **69**, 631 (1998).

[53] S. L. Bogomolov et al., Proceedings of Cyclotrons and Their Applications 2001, Sixteenth International Conference, Michigan, USA, (2001).

[54] P. Leherissier, C. Barue, C. Canet, M. Dubois, M. Dupuis, J. L. Flambard, G. Gaubert, P. Jardin, N. Lecesne, F. Lemagnen, R. Leroy, J. Y. Pacquet, and F. Pellemoine-Landre, Review of Scientific Instruments **75**, 1488 (2004).

[55] D. Hitz, A. Girard, K. Serebrennikov, G. Melin, D. Cormier, J. M. Mathonnet, J. Chartier, L. Sun, J. P. Briand, and M. Benhachoum, Review of Scientific Instruments **75**, 1403 (2004).

[56] S. Gammino, G. Ciavola, L. Celona, D. Hitz, A. Girard, and G. Melin, Review of Scientific Instruments **72**, 4090 (2001).

[57] T. Nakagawa, T. Kurita, M. Kidera, M. Imanaka, Y. Higurashi, M. Tsukada, S. M. Lee, M. Kase, and Y. Yano, Review of Scientific Instruments **73**, 513 (2002).

[58] Y. Higurashi et al., Nucl. Instrum. Methods. Phys. Res A **510**, 206 (2003).

[59] R. Geller, in Proceedings of the International Conference on ECR Ion Source and their Applications, East Lansing, , 15 (1987).

[60] D. Kchler, M. ONeil, and R. Scrivens, Proceedings of the 18th International Workshop on ECR Ion Sources, Chicago, IL USA, **MOPO11**, 89 (Sep. 2008).

[61] J. Arianer and R. Geller, Annu. Rev. Nucl. Part. Sci **31**, 19 (1981).

[62] R. Geller, Annu. Rev. Nucl. Part. Sci **40**, 15 (1990).

[63] I. G. Brown, *The Physics and Technology of Ion Sources*, Wiley, New York, 2004.

[64] D. Leitner et al., Cyclotrons and Their Applications 2007, Eighteenth International Conference, Giardini, Italy , PPT (2007).

[65] J. P. M. Beijers, *Lecture notes on plasma physics*, University of Groningen, Groningen, 2007-2008.

[66] F. F. Chen, *Introduction to Plasma Physics and Controlled Fusion: Plasma Physics*, Springer, 1984.

[67] C. M. Lyneis et al., Rev. Sci. Instrum. **75**, 1389 (2004).

[68] H. W. Zhao et al., Rev. Sci. Instrum. **73**, 525 (2002).

[69] G. Ciavola, S. Gammino, L. Celona, L. Torrisi, S. Passarello, L. Andó, M. Cavenago, A. Galatà, P. Spaedtke, K. Tinschert, R. Lang, R. Iannucci, R. Leroy, C. Barue, D. Hitz, P. Seyfert, H. Koivisto, P. Suominen, O. Tarvainen, H. Beijers, S. Brandenburg, D. Vanrooyen, C. Hill, D. Kuchler, H. Homeyer, J. Röhrich, L. Schachter, and S. Dobrescu, Review of Scientific Instruments **77**, 03A303 (2006).

[70] C. M. Lyneis, D. Leitner, D. S. Todd, G. Sabbi, S. Prestemon, S. Caspi, and P. Ferracin, Review of Scientific Instruments **79**, 02A321 (2008).

[71] T. H. Stix, *Waves in plasmas*, Springer-Verlag, Newyork, Inc, 1992.

[72] G. Melin, F. Bourg, P. Briand, M. Delaunay, G. Gaudart, A. Girard, D. Hitz, J. P. Klein, P. Ludwig, T. K. Nguyen, M. Pontonnier, and Y. Su, Review of Scientific Instruments **65**, 1051 (1994).

[73] C. Barué, M. Lamoureux, P. Briand, A. Girard, and G. Melin, Journal of Applied Physics **76**, 2662 (1994).

[74] A. G. G. Douysset, H. Khodja and J. P. Briand, Phys. Rev. E **61**, 3015 (2000).

[75] S. Gammino, G. Ciavola, L. G. Celona, D. Mascali, and F. Maimone, IEEE Transactions on Plasma Science **36**, 1552 (2008).

[76] C. Perret, A. Girard, H. Khodja, and G. Melin, Physics of Plasmas **6**, 3408 (1999).

[77] D. R. Whaley and W. D. Getty, Phys. Fluids B **2**, 1195 (June 1990).

[78] O. Tarvainen, *Studies of Electron Cyclotron Resonance Ion Source Plasma Physics*, PhD thesis, JYFL, Finland, 2005.

[79] G. Shirkov, Nucl. Instrum. Methods Phys. Res. A **322**, 161 (1992).

[80] G. Douysset, 1, H. Khodja, A. Girard, and J. P. Briand, Phys. Rev. E **61**, 3015 (2000).

[81] G. Melin, F. Bourg, P. Briand, J. Debernardi, M. Delaunay, R. Geller, B. Jacquot, P. Ludwig, T. K. N'Guyen, L. Pin, M. Pontonnier, J. C. Rocco, and F. Zadworny, Review of Scientific Instruments **61**, 236 (1990).

[82] A. Girard, D. Hitz, G. Melin, and K. Serebrennikov, Review of Scientific Instruments **75**, 1381 (2004).

[83] G. Melin et al., in Proceedings of the Tenth International Workshop on ECR Ion Source, Knoxville, , 1 (1990).

[84] A. G. Drentje and J. Sijbring, KVI Annual Report , 79 (1983).

[85] A. G. Drentje, Nucl. Instrum. Methods Phys. Res. B **9**, 526 (1985).

[86] Z. Xie and C. Lyneis, Proceedings of the 12th International Workshop on ECR Ion Sources, Riken, , 24 (1995).

[87] Z. Q. Xie and C. M. Lyneis, Review of Scientific Instruments **66**, 4218 (1995).

[88] G. D. Alton, F. W. Meyer, Y. Liu, J. R. Beene, and D. Tucker, Review of Scientific Instruments **69**, 2305 (1998).

[89] S. Gammino and G. Ciavola, Plasma Sources Sci. Tech. **5**, 19 (1996).

[90] R. Keller, Nucl. Instrum. Methods Phys. Res. A **247**, 298 (1990).

[91] K. U. Riemann, J. Phys. D: Appl. Phys. **24**, 493 (1991).

[92] J. R. Pierce, *Theory and Design of Electron Beams*, D. VAN NASTRAND INC, 1954.

[93] V. Mironov and J. P. M. Beijers, Phys. Rev. ST Accel. Beams **12**, 073501 (2009).

[94] S. Saminathan, V. Mironov, J. P. M. Beijers, R. Kremers, and S. Brandenburg, Review of Scientific Instruments **81**, 02B706 (2010).

[95] V. Mironov, J. Beijers, H. Kremers, J. Mulder, S. Saminathan, and S. Brandenburg, Proceedings of CYCLOTRONS 2010, Lanzhou, China, **MOPCP053**, 1 (2010).

[96] W. H. Koh, N. H. Choi, D. I. Choi, and Y. H. Oh, Journal of Applied Physics **73**, 4205 (1993).

[97] V. D. D. Jabon, A. M. Umnov, and D. S. Diaz, Physica Scripta **70**, 38 (2004).

[98] L. T. Sun, Y. Cao, H. W. Zhao, X. H. Guo, Z. M. Zhang, Y. C. Feng, J. Y. Li, L. Ma, J. Li, H. Y. Zhao, W. He, X. X. Li, D. Hitz, and A. Girard, AIP Conference Proceedings **749**, 227 (2005).

[99] P. Spädtke, K. Tinschert, R. Lang, and R. Iannucci, AIP Conference Proceedings **749**, 47 (2005).

[100] L. Panitzsch, M. Stalder, and R. F. Wimmer-Schweingruber, Review of Scientific Instruments **82**, 033302 (2011).

[101] G. Melin, A. G. Drentje, A. Girard, and D. Hitz, Journal of Applied Physics **86**, 4772 (1999).

[102] D. Wutte, M. A. Leitner, and C. M. Lyneis, Physica Scripta **T92**, 247 (2001).

[103] D. Wutte, M. A. Leitner, C. M. Lyneis, C. E. Taylor, and Z. Q. Xie, AIP Conference Proceedings **473**, 384 (1999).

[104] A. Girard, C. Perret, G. Melin, and C. Lécot, Review of Scientific Instruments **69**, 1100 (1998).

[105] A. Girard, K. Serebrennikov, G. Melin, R. Vallcorba, and C. Lécot, Review of Scientific Instruments **73**, 1145 (2002).

[106] A. Girard, C. Pernot, G. Melin, and C. Lécot, Phys. Rev. E **62**, 1182 (2000).

[107] A. Girard, D. Hitz, G. Melin, K. Serebrennikov, and C. Lécot, Review of Scientific Instruments **75**, 1463 (2004).

[108] J. S. K. L. Zhao and B. Cluggish, Proceedings of PAC07, Albuquerque, New Mexico, USA, **TUPASO79**, 1832 (2007).

[109] L. Zhao, B. Cluggish, J. S. Kim, R. Pardo, and R. Vondrasek, Review of Scientific Instruments **81**, 02A304 (2010).

[110] B. Cluggish, L. Zhao, and J. S. Kim, Review of Scientific Instruments **81**, 02A301 (2010).

[111] D. Mascali, L. Neri, S. Gammino, L. Celona, G. Ciavola, N. Gambino, R. Miracoli, and S. Chikin, Review of Scientific Instruments **81**, 02A334 (2010).

[112] S. G. L. Celona and G. Ciavola, in Proceedings of HB2010, Morschach, Switzerland, **MOPD36**, 1 (2010).

[113] D. Mascali et al., Proceedings of 19th International Workshop on ECR Ion Sources, Grenoble, France, (2010).

[114] Kobra3d-inp, junkernstr.99, 65205 wiesbaden, germany.

[115] P. Spädtke, R. Lang, J. Mäder, F. Maimone, J. Roßbach, and K. Tinschert, Proceedings of the 19th International Workshop on ECR Ion Sources, Grenoble, France, , TUCOAK05 (August 2010).

[116] P. Spädtke, Review of Scientific Instruments **81**, 02B725 (2010).

[117] P. Spädtke, K. Tinschert, R. Lang, J. Mäder, J. R. bach, J. W. Stetson, and L. Celona, Review of Scientific Instruments **79**, 02B716 (2008).

[118] J. P. M. Beijers and V. Mironov, Review of Scientific Instruments **81**, 02A307 (2010).

[119] J. P. Verboncoeur, A. B. Langdon, and N. T. Gladd, J. Comput. Phys. Commun **87**, 199 (1995).

[120] K. Nanbu, Phys. Rev. E **55**, 4642 (1997).

[121] T. Takizuka and J. Abe, J. Comput. Phys **25**, 205 (1977).

[122] D. Werren, Nuclear Instruments and Methods **58**, 84 (1968).

[123] Technical report, KVI.

[124] H. R. Kremers et al., High En. Phys. and Nucl. Phys. **31**, 90 (2007).

[125] M. Doleans, S. Chouhan, D. Cole, G. Machicoane, F. Marti, P. Miller, J. Moskalik, M. Steiner, X. Wu, P. Zavodszky, A. Zeller, Q. Zhao, N. Msu, and E. Lansing, Proceedings of the eighteenth international conference on Cyclotrons and Their Applications, Giardini Naxos, Italy (2007).

[126] P. Strehl, Rev. Sci. Instrum. **63**, 2652 (April 1992).

[127] B. Wolf, *Handbook of ion sources*, CRC Press. Inc, Florida, 1995.

[128] P. Strehl, *Beam Instrumentation and Diagnostics*, Springer, Heidelberg, 2006.

[129] D. Brandt, CAS Proceedings: CERN Accelerator school on beam diagnostics,Dourdan, France, (28 May - 6 June 2008).

[130] H. R. Kremers, J. P. M. Beijers, S. Brandenburg, S. Saminathan, J. Mulder, V. Mironov, and T. Thuillier, Proceedings of the 18th International Workshop on ECR Ion Sources, Chicago, IL USA, , TUCOA02 (Sep. 2008).

[131] P. Allison, J. D. Sherman, and D. B. Holtkamp, IEEE Trans. Nucl. Sci. **NS-30**, 2204 (1983).

[132] K. T. McDonald and D. P. Russel, Un published (Oct. 1988).

[133] S. Humphries, *Charged Particle Beams*, Wiley, New York, 1990.

[134] M. Sarstedt, Rev. Sci. Instrum. **67**, 1653 (1996).

[135] S. K. Guharay et al., Rev. Sci. Instrum. **67**, 2534 (1996).

[136] M. Zhang, Internal report, Fermilab-TM-1988 .

[137] J. Wang et al., Nucl. Instrum. Meth. A **307**, 190 (1991).

[138] M. P. Stockli, AIP Conf. Proc. **868**, 25 (Nov.2006).

[139] H. R. Kremers, J. P. M. Beijers, and S. Brandenburg, Proc. of DIPAC-2007 , Venice (2007).

[140] A. Septier, *Applied Charged Particel Optics, Part A*, Academic Press, New York, 1980.

[141] I. Zeinoun et al., Rev. Sci. Instrum. **71**, 1194 (FEB. 2000).

[142] D. T. J. Qiang and D. Leitner, Comput. Phys. Commun **175**, 416 (2006).

[143] D. S. Todd, D. Leitner, M. Leitner, C. M. Lyneis, J. Qiang, and D. P. Grote, Review of Scientific Instruments **77**, 03A338 (2006).

[144] H. R. Kremers, J. P. M. Beijers, S. Brandenburg, j. Mulder, S. Saminathan, and V. Mironov, Proceedings of the 19th International Workshop on ECR Ion Sources, Grenoble, France, , TUCOAK05 (August 2010).

[145] M. A. Leitner et al., in Proceedings of the 2001 Particle Accelerator Conference, Chicago, , 67 (2001).

[146] M. B. B. Hartmann and H. Wollnik, Nucl. Instrum. Meth. Phy. Res. A **297**, 343 (1990).

[147] J. Camplan and R. Meunier, Nucl. Instrum. Meth. **186**, 445 (1981).

[148] K. L. Brown, First- and second-order charged particle optics, Technical report, KVI, SLAC Rep. No. 3381, 1984.

[149] Q. Zhao, a. Balabin, M. Doleans, F. Marti, J. Stetson, and X. Wu, Proceedings of the 2005 Particle Accelerator Conference , 1336 (2005).

[150] X. Wu, D. Cole, M. Doleans, G. Machicoane, F. Marti, P. Miller, J. Stetson, M. Steiner, P. Zavodszky, and Q. Zhao, 17th International workshop on ECR Ion Sources and their applications, Lanszhow, China (2006).

[151] M. Leitner et al., ECRIS02 workshop, Jyväskylä (FI) (June 2002).

[152] L. Celona, G. Ciavola, F. Consoli, S. Gammino, F. Maimone, D. Mascali, P. Spädtke, K. Tinschert, R. Lang, J. Mäder, J. R. bach, S. Barbarino, and R. S. Catalano, Review of Scientific Instruments **79**, 023305 (2008).

[153] K. Tinschert, P. Spädtke, J. Bossler, R. Iannucci, and R. Lang, AIP Conference Proceedings **749**, 241 (2005).

[154] K. Halbach, Nucl. Instrum. Methods **169**, 1 (1980).

[155] P. Spädtke, R. Lang, J. Mäder, J. R. bach, K. Tinschert, and J. Stetson, High En. Phys. and Nucl. Phys. (HEP & NP) **31**, 192 (2007).

[156] P. Spädtke, J. Bossler, H. Emig, K. D. Leible, M. Khaouli, C. Mhle, S. Schennach, H. Schulte, and K. Tinschert, International Linear Accelerator Conference, Geneva, Switzerland , 163 (Aug 1996).

[157] See the homepage of poisson/superfish http://laacg1.lanl.gov/laacg.

[158] P. Spädtke, Private communication, GSI, Darmstadt (2010).

[159] P. Spädtke, R. Lang, J. Mader, J. Robach, and K. Tinschert, Proceedings of ECRIS08, Chicago, IL USA, (2008).

[160] J. W. Stetson and P. Spadtke, 2007 IEEE Particle Accelerator Conference (PAC) , 3789 (2007).

[161] H. Koivisto, T. Ropponen, J. Ropponen, T. Koponen, M. Savonen, V. Toivanen, P. Heikkinen, G. Machicoane, J. Stetson, P. Zavodszky, X. Wu, M. Doleans, S. Chouhan, N. Msu, P. Spädtke, H. Beijers, and S. Brandenburg, Proceedings of the eighteenth international conference on Cyclotrons and Their Applications, Giardini Naxos, Italy, (2007).

[162] H. Koivisto, T. Ropponen, V. Toivanen, and M. Savonen, Proceedings of ECRIS08, Chicago, IL USA, (2008).

[163] J. W. Stetson et al., Proceedings of the eighteenth International Conference on Cyclotrons and their Applications , 340 (2008).

[164] C. Lyneis, D. Leitner, S. Abbott, R. Dwinell, M. Leitner, C. Silver, and C. Taylor, Review of Scientific Instruments **75**, 1389 (2004).

[165] H. W. Zhao, L. T. Sun, W. Lu, X. Z. Zhang, X. H. Guo, Y. Cao, H. Y. Zhao, Y. C. Feng, J. Y. Li, H. Y. Ma, Y. Shang, B. H. Ma, H. Wang, X. X. Li, and D. Z. Xie, Review of Scientific Instruments **81**, 02A202 (2010).

[166] P. A. Zavodszky et al., Proceedings of PAC07, Albuquerque, New Mexico, USA , FRXAB03 (2007).

[167] C. M. Lyneis, Private communication, LBNL, USA (2010).

Samenvatting

Versnellers voor ionen, zoals bijvoorbeeld cyclotrons en synchrotrons, hebben allemaal een bron nodig die de ionen produceert. Op het Kernfysisch Versneller Instituut (KVI) in Groningen wordt hiervoor een zogenaamde Electron Cyclotron Resonance (ECR) ionenbron gebruikt die intense bundels kan produceren van hooggeladen ionen van alle elementen. ECR ionenbronnen, gebaseerd op resonante microgolf verhitting van de electronen in een magnetisch opgesloten plasma, zijn zeer efficiënte bronnen van hooggeladen ionen. Na extractie wordt de ionenbundel door middel van een 110° analyse magneet op de verhouding lading/massa geselecteerd en door een ongeveer 25 meter lange lage-energie bundellijn bestaande uit buigmagneten en focusserings elementen getransporteerd naar het AGOR cyclotron. Na in het cyclotron te zijn versneld wordt de hoge-energie bundel naar het uiteindelijke experiment getransporteerd.

Helaas is het transport van de bundel tussen ionenbron en cyclotron niet erg efficiënt, de transmissie is typich maar ongeveer 20%. Soortgelijke transmissies van lage-energie bundellijnen worden ook bij andere versneller faciliteiten gevonden. Deze lage bundel transmissies zijn problematisch, vooral als de bundelintensiteit die aan het experiment wordt geleverd beperkt wordt door de ionenbron. Er zijn verschillende verklaringen geopperd voor deze lage bundel transmissies, zoals bijvoorbeeld de asymmetrische faseruimte verdeling van de uit een ECR ionenbron geëxtraheerde bundels en/of het impulsmoment van de ionenbundels ten gevolge van het gecombineerde effect van de electrische en magnetische velden in het extractie gebied van de bron. Er is echter maar weinig bewijs voor deze verklaringen.

Om een betere verklaring voor de lage bundel transmissie te vinden en deze te verbeteren, zijn in het kader van dit proefschrift uitvoerige computer simulaties gedaan van de productie, extractie en het transport van hooggeladen ionenbundels voor de 14 GHz KVI-AECR ionenbron. Deze simulaties zijn gebaseerd op gedetailleerde baanberekeningen van de ionen, met inachtneming van hogere-orde bijdragen veroorzaakt door zowel kinematische effecten, de relatief grote emittantie van de geëxtraheerde lage-energie bundels, de afbeeldingsfouten van de ionenoptische elementen in de bundellijn en ruimteladings effecten. De baanberekeningen zijn uitgevoerd met een tweetal commerciële codes (GPT en LORENTZ3D) en een in het publieke domein verkrijgbare code (COSY INFINITY). De voor de simulaties benodigde start condities van de ionenbanen in het vlak van de extractie-electrode van de ECR ionenbron zijn berekend met een op het KVI ontwikkelde Particle-In-Cell Monte-Carlo Collision (PIC-MCC) code. Deze code simuleert de ionen dynamica in het plasma van de ionenbron vrijwel volledig en is in staat de belangrijkste eigenschappen van de geëxtraheerde ionenbundels te reproduceren.

De computer simulaties zijn getest door de resultaten ervan te vergelijken met metingen van 2-dimensionale bundelprofielen direct na het extractie systeem en in het beeldvlak van de analyse magneet. Tevens zijn de simulaties vergeleken met metingen van de 4-dimensionale transversale fase-ruimte verdelingen van de ionenbundel in het brandvlak van de analyse magneet. Deze laatste metingen vormen een veel stringentere test voor de simulaties en zijn gedaan met een nieuwe, speciaal daartoe op het KVI ontwikkelde, pepperpot emittantie meter. Met dit instrument kunnen behalve de horizontale en verticale bundel emittanties ook correlaties tussen beide transversale vlakken gemeten worden. Dit soort correlaties zijn karakteristiek voor met ECR ionenbronnen geproduceerde bundels ten gevolge van het extraheren van de bundel in een magnetisch veld en kunnen niet gemeten worden met de veelgebruikte emittantie meters van het Allison type.

We hebben simulaties en metingen uitgevoerd aan twee verschillende ionenbundels. Als eerste hebben we onze aanpak getest op een uit één ladingsgraad bestaande He^+ bundel. De startwaarden voor de baanberekeningen van de He^+ ionen in het extractievlak van de ECR bron zijn berekend met de PIC-MCC code. De ruimtelijke verdeling van de ionen in het extractie gat van de plasma electrode heeft duidelijk een drievoudige symmetrie die karakteristiek is voor de magnetische structuur van de ECR bron en aantoont dat de ionen gemagnetiseerd zijn. Vervolgens hebben we het transport van de He^+ bundel door het extractie systeem en analyse magneet berekend tot aan het beeldvlak van de magneet en hieruit 4-dimensionale fase-ruimte verdelingen gedestilleerd. Vergelijking met de gemeten bundelprofiel en emittantie verdelingen leiden tot een aantal interessante gevolgtrekkingen:

1. Het blijkt dat de berekende en gemeten bundel verdelingen het best met elkaar overeenstemmen indien aangenomen wordt dat de bundel bestaat uit onafhankelijke ionen, m.a.w. de ionen ’voelen’ elkaars Coulomb kracht niet. Dit betekent dat de positieve ruimtelading van de He^+ ionen in de bundel volledig gecompenseerd wordt door in de bundel ingevangen electronen. Wij hebben deze volledige ruimteladings compensatie kunnen vaststellen tot een bundelstroom van 0.5 mA, het maximum dat onze meetinstrumenten nog kunnen accepteren.

2. De emittantie van de geëxtraheerde He^+ bundel is $\varepsilon = 65\,\pi$ mm mrad, zowel in het horizontale als verticale vlak. Deze waarde wordt vrijwel volledig bepaald door behoud van gegeneraliseerd impulsmoment in het magnetische veld van de extractie solenoïde van de ECR bron.

3. Extractie in het magnetische randveld van de ECR bron leidt tot een duidelijke rotatie van de He^+ bundel. Berekende en gemeten rotatie hoeken komen goed met elkaar overeen.

4. Transport van de He^+ bundel door de analyse magneet leidt tot een sterke vergroting van de effectieve emittantie, i.e. de berekende waarden van de bundel emittantie na de analyse magneet zijn $360\,\pi$ mm mrad in het horizontale en $240\,\pi$ mm mrad

in het verticale vlak. Deze waarden komen redelijk goed overeen met de gemeten waarden van respectievelijk 390 en 320 π mm mrad. De lagere waarde voor de verticale bundel emittantie komt doordat de magneet een te kleine verticale apertuur heeft zodat een deel van de bundel verloren gaat. De berekeningen wijzen uit dat de vergroting van de bundel emittantie hoofdzakelijk veroorzaakt wordt door de sterke tweede-orde aberraties van de analyse magneet.

5. De berekende en gemeten bundelprofielen in het beeldvlak van de analyse magneet komen goed met elkaar overeen. Deze hebben de voor tweede-orde aberraties karakteristieke vorm van een halve-maan profiel.

Dezelfde gecombineerde aanpak van simulaties en metingen is gebruikt om de extractie en transport van een uit meerdere ladingsgraden bestaande Ne^{q+} ($q = 1, \ldots, 8$) bundel te bestuderen. We hebben een realistische situatie gesimuleerd waarbij de ECR bron geoptimaliseerd is voor de productie van een Ne^{6+} bundel. In de PIC-MCC code kunnen hiertoe een tweetal parameters getuned worden, namelijk de gasdruk en de electronen temperatuur. Met de code zijn de fase-ruimte verdelingen voor de verschillende ladingsgraden van de Neon ionen in het extractie vlak van de ECR bron berekend die vervolgens als start condities zijn gebruikt voor de extractie en transport simulaties. De ruimtelijke verdeling van de ionen in het extractie vlak van de ECR bron heeft weer de karakteristieke drievoudige symmetrie, maar tevens vinden we dat de concentratie van de ionen rondom de magnetische as van de bron toeneemt voor hogere ladingsgraden. De extractie en transport simulaties zijn op dezelfde wijze uitgevoerd als voor de He^{+} bundel, alleen bestaat de bundel nu uit verschillende ladingsgraden en hebben we de transport simulatie uitgebreid tot voorbij de 90° magneet. We hebben de extractie en transport simulaties getest door deze te vergelijken met metingen van bundelprofielen na het extractie systeem, in het beeldvlak van de analyse magneet en achter de 90° magneet en met metingen van de ladingsverdeling van de bundel in het beeldvlak van de analyse magneet. Simulaties en metingen komen goed overeen als we aannemen dat ook de Neon bundel volledig ladings gecompenseerd is. Ook uit deze berekeningen blijkt dat de te kleine verticale apertuur en de tweede-orde aberraties van de analyse magneet leiden tot een bundelverlies van ongeveer 25% en een significante verhoging van de effectieve bundel emittantie.

Het is te tijdrovend om op deze manier het bundeltransport door de hele lage-energie bundellijn door te rekenen. Daarom hebben we hiervoor met de COSY INFINITY code een tweede-orde overdrachtsmatrix berekend vanaf het beeldvlak van de analyse magneet tot aan de zogenaamde matching sectie vlak voor het AGOR cyclotron. Met behulp van deze overdrachtsmatrix kunnen we vervolgens heel eenvoudig een met GPT berekende transversale faseruimte verdeling in het beeldvlak van de analyse magneet transformeren naar de matching sectie. Uit de bekende acceptantie van het cyclotron van 140 π mm mrad volgt dan dat maximaal slechts 15 - 20 % van de uit de ECR bron geëxtraheerde bundel in het cyclotron geïnjecteerd kan worden. Deze berekende bundel transport efficëntie komt goed overeen met in de praktijk waargenomen waardes.

De relatief lage waarde van de bundel transport efficiëntie wordt hoofdzakelijk veroorzaakt door de tweede-orde aberraties van de 110° analyse magneet. Daarnaast zijn ook de bundelverliezen door de te kleine verticale apertuur van de magneet niet verwaarloosbaar. We hebben een studie verricht naar de mogelijkheid om de transport efficieëntie te verhogen door het verbeteren van de optische eigenschappen van de analyse magneet. Het blijkt inderdaad mogelijk om zo'n verbetering door te voeren door de verticale apertuur te vergroten van 67 naar 110 mm en de vorm van de magneetpolen zodanig te modificeren dat de tweede-orde aberratie coëfficiënten voor een belangrijk deel gecompenseerd worden. Dit laatste kan gerealiseerd worden door de in- en uittree vlakken van de magneetpolen een concave vorm te geven en de centrale gedeeltes een convexe vorm. We hebben de vorm van de pooloppervlakken zodanig geoptimaliseerd dat de tweede-orde aberratie coëfficiënten zo klein mogelijk zijn. Bundel transport simulaties laten zien dat hiermee de transport efficiëntie van de lage-energie bundellijn verhoogd kan worden tot 45 %, een winst van een factor twee tot drie.

Tenslotte hebben we onze bundel simulatie methodiek toegepast op een ECR bron en bijbehorend lage-energie bundelgeleidingssysteem gebruikt voor test doeleinden op het GSI instituut in Darmstadt, Duitsland. Karakteristiek voor dit bundelgeleidingssysteem is dat tussen het extractie systeem van de ECR bron en de analyse magneet nog een solenoïde en een verticaal focusserende quadrupool magneet geplaatst is. We hebben simulaties gedaan voor een He^{+} en een Ar^{7+} bundel, waarbij aangenomen werd dat beide bundels volledig ladings geneutraliseerd zijn. Voor de He^{+} bundel zijn de startcondities van de ionen in het extractie vlak van de ECR bron berekend met de PIC-MCC code en de ionenbanen door de bundellijn met GPT. We hebben de simulaties kunnen testen door deze te vergelijken met metingen van bundelprofielen direct achter de solenoïde en de analyse magneet. Simulaties en metingen komen redelijk met elkaar overeen. Een interessant fenomeen hierbij, dat ook bij andere, soortgelijke bundellijnen werd gevonden, is dat het bundelprofiel hol is. Volgens de conventionele verklaring worden holle bundelprofielen veroorzaakt door ruimteladings effecten, waarbij de ionen met een grote ladings-massa verhouding door de solenoïde sterker gefocusseerd worden dan de ionen met een kleinere ladings-massa verhouding, waardoor deze laatste ionen in de bundel naar buiten worden gedrukt. Echter, in onze simulatie nemen we aan dat de ruimtelading volledig geneutraliseerd is. De holle bundel wordt volgens onze simulaties veroorzaakt door de sferische aberratie van de solenoïde en de grote emittantie van de geëxtraheerde bundel, waardoor ionen ver van de optische as sterker gefocusseerd worden en de as eerder kruisen dan ionen die dichter bij de as bewegen.

We hebben twee verschillende simulaties uitgevoerd van de Ar^{7+} bundel, namelijk één waarbij de startcondities berekend zijn met onze PIC-MCC code en een andere waarbij de startcondities berekend werden door onze GSI collega's met de KOBRA3D-INP code. Beide sets startcondities verschillen significant en leiden ook tot grote verschillen in de berekende bundelprofielen en emittanties. Helaas hebben we nog geen metingen kunnen doen om uit te wijzen welke van de twee simulaties het beste met de realiteit overeenstemt.

Onze algemene conclusie uit deze studie is dat door het niet-paraxiale karakter en de relatief grote emittantie van uit ECR ionenbronnen geëxtraheerde ionenbundels het belangrijk is om voldoende aandacht te besteden aan de optische eigenschappen van met name de dipool magneten in een lage-energie bundellijn. Moderne simulatie software berekent het bundeltransport van ionen in lage-energie bundellijnen met voldoende nauwkeurigheid om een optimaal ontwerp met minimale hogere-orde aberraties mogelijk te maken. We hebben aangetoond dat voor bundelstromen tot ongeveer een 0.5 mA de ionenbundel volledig ladings geneutraliseerd is en we verwachten dat dit zo blijft tot bundelstromen van ongeveer 5 mA. Voor de nieuwste generatie supergeleidende ECR bronnen, waarbij de geëxtraheerde bundelstroom in de orde van 50 mA of meer is, zal ladingscompensatie wel een belangrijke issue worden.

List of Acronyms

AECR	Advanced Electron Cyclotron Resonance ion source
LEBT	Low Energy Beam Transport
KVI	Kernfysisch Versneller Instituut, Groningen, Netherlands
AGOR	Accelerator Groningen ORsay
TRIμP	Trapped Radioactive Isotopes: μicro-laboratories for fundamental Physics
GSI	Helmholtzzentrum für Schwerionenforschung GmbH, Darmstadt, Germany
RIKEN	The Institute of Physical and Chemical Research, Saitama, Japan
NSCL	National Superconducting Cyclotron Laboratory, Michigan, USA
JYFL	Department of Physics, University of Jyväskylä, Jyväskylä, Finland
GANIL	Grand Accelerateur National d'Ions Lourds, Caen, France
ANL	Argonne National Laboratory, Argonne, USA
LBNL	Lawrence Berkeley National Laboratory, Berkeley, USA
MSU	Michigan State University, Michigan, USA
FAIR	Facility for Antiproton and Ion Research, Darmstadt, Germany
FRIB	Facility for Rare Isotope Beams, Michigan, USA
EIS	ECR Injector Setup
rms	root mean square
PIC-MCC	Particle-in-Cell Monte Carlo Collision code
GPT	General Particle Tracer, 3D Simulation code for trajectory calculation
BEM	Boundary Element Method
FEM	Finite Element Method
ECRH	Electron Cyclotron Resonance Heating
MHD	Magnetohydrodynamics
RF	Radio Frequency
EEDF	Electron Energy Distribution Function
CSD	Charge State Distribution
TWTA	Traveling Wave Tube Amplifiers
FCs	Faraday Cups
BaF	Barium Fluoride
NdFeB	Neodymium Iron Boron permanent magnet

CCD	Charged Coupled Device
MCP	Multi-Channel Plate
VT	Viewing Target
EFB	Effective Field Boundary

List of Publications

Extraction and Transport of MCI beams from an Electron Cyclotron Ion Source
S. Saminathan, J.P.M Beijers, H.R. Kremers, V. Mironov, J. Mulder and S. Brandenburg
Proceedings of the 14th International Conference on Ion Sources, Giardini Naxos, Italy, September 2011

Dipole magnet optimization for high efficiency low energy beam transport
S. Saminathan, J.P.M Beijers, J.Mulder, V. Mironov, and S. Brandenburg
Proceedings of the 14th International Workshop on ECR Ion Sources, Grenoble, France, August 2010

Trace space reconstruction from pepperpot data
H.R. Kremers, J.P.M. Beijers, V. Mironov, J.Mulder, S. Saminathan, and S. Brandenburg
Proceedings of the 14th International Workshop on ECR Ion Sources, Grenoble, France, August 2010

ECRIS development at KVI
V. Mironov, J.P.M. Beijers, H.R. Kremers, J. Mulder, S. Saminathan, and S. Brandenburg
Proceedings of the nineteenth International Conference on Cyclotrons and their Applications, Lanzhou, China, September 2010

Progress towards high intensity heavy ion beams at the AGOR-facility
S. Brandenburg, J.P.M. Beijers, M.A. Hevinga, M.A. Hofstee, H.R. Kremers, V. Mironov, J. Mulder, S. Saminathan, and A. Sen
Proceedings of the nineteenth International Conference on Cyclotrons and their Applications, Lanzhou, China, September 2010

Study of ion beam extraction and transport from an electron cyclotron resonance ion source
S. Saminathan, V. Mironov, J.P.M. Beijers, H.R. Kremers, and S. Brandenburg
Review of Scientific Instruments 81, 02B706 (2010)

Study of ion beam extraction and transport from an electron cyclotron resonance ion source
S. Saminathan, V. Mironov, J.P.M Beijers, R. Kremers, and S. Brandenburg
Proceedings of the 13th International Conference on Ion Sources, Gatlinburg, Tennessee, USA, September 2009

Comparison between an Allison scanner and the KVI-4D emittance meter
H. R. Kremers, J. P. M. Beijers, S. Brandenburg, S. Saminathan, and V. Mironov
Proceedings of ECRIS08, Chicago, IL USA

Ion source development at KVI
J.P.M. Beijers, H.R. Kremers, V. Mironov, J. Mulder, S. Saminathan, and S. Brandenburg
Review of Scientific Instruments 79 , 02A320(2008)

Operations of KVI AECRIS at AGOR superconducting cyclotron facility
V. Mironov, J. P.M. Beijers, S. Brandenburg, H. R. Kremers, J. Mulder, and S. Saminathan
Proceedings of ECRIS08, Chicago, IL USA

Ion source development at the AGOR facility
S. Brandenburgy , J.P.M. Beijers, H.R. Kremers, V. Mironov, J. Mulder, and S. Saminathan
Proceedings of the eighteenth International Conference on Cyclotrons and their Applications, Giardini Naxos, Italy, October 2007

Acknowledgement

This thesis would not have been possible without the help and support of Prof. dr. Sytze Brandenburg and Dr. ir. J. P. M. Beijers. Dr. Vladimir Mironov, Rob Kremers and Jan Mulder have also helped me enormously in this work.

The good advice, support and friendship of my supervisor, Hans Beijers, has been invaluable on both an academic and a personal level, for which I am extremely grateful. I owe my deepest gratitude to my thesis supervisor, Sytze Brandenburg for his constant and invaluable guidance during my Ph. D work. His attention, moral support and timely suggestions were useful in the preparation of my thesis. I am very much thankful to my supervisors for putting me in the track of this research.

I am very much grateful to Vladimir Mironov for his generous help in particular issues related to simulations and experimental setup. I thank Rob Kremers for helping me in diagnostics and I thank Jan Mulder for helping me in mechanical drawings. Also I would like to thank these people for sharing the lunch table very often with me and the discussions during the lunch time is a nice memory.

I would like to thank FANTOM board for giving me the opportunity to participate in the FANTOM schools. I am thankful to KVI and director for providing me the nice working environment. I also acknowledge the KVI and RUG for the support of Ubbo Emmius scholarship.

I am grateful to members of my thesis reading committee Prof. dr. K. J. Boller (University of Twente, Enschede, The Netherlands), Prof. dr. ir. R. H. Hoekstra (KVI, Groningen The Netherlands), Dr. C. M. Lyneis (LBNL, California, USA) for spending their time on careful reading of my thesis as well as for their valuable comments.

It is a pleasure to thank Peter Spädtke and K. Tinschert, with whom I have collaborated on the work in chapter 8. I would like to thank Thomas Thuillier for the comparison of pepper-pot device with Allison scaner in their experimental setup at LPSC, Grenoble.

I am thankful to all of my colleagues in the accelerator group and would like to give spacial thanks to Mariet, Marc-Jan and Harm post. Also I would like to thank my former

colleagues in the NBI group at IPR (Gandhinagar, Gujarat, India) for their encouragement to pursue a graduate study.

It is pleasure to thank all the people working in the mechanical, vacuum, electronics and IT groups of KVI and grateful to KVI administration, personal and financial section for their kind help during my stay in Groningen. I am very much thankful to Hilde Landstra and Hilde van der Meer for all the paper works they have done for me.

I met some very nice people who made my stay enjoyable in Groningen. Thanks for the unforgettable time: Ahmad, Ali, Alma, Andraey, Daren, Dennis, Duurt, Elmaddin, Erwin, Gabriel, Hong, Hossein, Kalpana, Leila, Lotje, Lotje, Manisha, Marlene, Moeini, Mohammad, Oksana, Ola, Olena, Olga, Oscar, Qader, Renato, Ruud, Sadia, Sahoo, Simona, Sivaji, Sohani, Subhadeep, Sybren, Victor, Wilbert and many others.

I express my gratitude to all my Indian friends in Groningen, who made me home away from home. It was a pleasure to share doctoral studies and life with Ayan, Bodhaditya, Easwar, Ganesh, Gobi, Gouri, Guru, Martin, Praveen, Ram, Rathana, Saheed, Siva, Sriram, Umakanth and Vanni.

These acknowledgments would not be complete without thanking my family for their constant support and care. Today I feel that my parents hard work and dreams have been blossomed. I thank my father Saminathan, my mother Vijayalakshmi, my brother Murthy and my sister Suja. I also wish to extend my thanks to my father-in-law, Sundar and my mother-in-law, Valarmathi for their kind support and I am grateful to all my teachers from school to university education. Finally, I would like to mention two other people who are very important in my life: My wife, Abirami and my little son, Anirudh. I thank Abirami for everything. I thank my little son for making me so happy with his cute smile and engaging me lot at home.

Suresh
Groningen